STUDY ON AIRBORNE SAR EXPERIMENT TO SIMULATE HYDROTERRA DATA

'SARSIMHT 2019'

Final Report

by

Valeria Gracheva, Rolf Scheiber, Ralf Horn, Martin Keller, Jens Fischer

German Aerospace Center (DLR) e.V.,
Microwaves and Radar Institute
SAR Technology Department
D-82234 Wessling, Germany

(Technical Report: DLR-HR-TR-SARSimHT-2019-003)

Prepared for the European Space Agency (ESA) under

Contract No. 4000129993/20/NL/FF/ab

Contents

1 Introduction and Purpose of the Document

This document is the final report of the SARSimHT study. The purpose of this study is to gain knowledge about the new SAR processing possibilities and challenges using satellite data from the Hydroterra system. Hydroterra is one of three mission concepts competing for the Earth Explorer 10, consisting of a geosynchronous satellite to cover Africa and the Mediterranean area with a C-band SAR for an improved understanding and prediction capability of rainfall and water availability, flooding and landslides.

The main objectives of this study are the following:

- To demonstrate the image formation process of Hydroterra through the exploitation of a repeat-pass multi-temporal airborne SAR image stack.
- To preliminary investigate variations in radar observables as a function of changing geophysical conditions.
- To investigate the potential to detect diurnal changes of land surface parameters (e.g. soil moisture) with simulated Hydroterra time series.
- To introduce wind effects in simulated Hydroterra data to identify and quantify to which extend defocussing of high vegetation areas affects the surrounding areas of bare soil / sparse vegetation.

This document is organized as follows: Chapter 2 gives an overview of the airborne campaign and previous work of this study. The simulated Hydroterra amplitude and interferometric products are presented in Chapter 3. Also an analysis of the image quality of Hydroterra amplitude products is performed in Chapter 3. Chapter 4 analyses the intensity, coherence and interferometric phase of field areas with available ground truth. In Chapter 4 this analysis is performed on F-SAR radar data, whereas in Chapter 5 the F-SAR data from Chapter 4 is used to simulate a Hydroterra like time series. Here the F-SAR data are adjusted to the radar parameters of one sizing scenario. The simulated Hydroterra time series is then applied in Chapter 5 to analyse the intensity, coherence and interferometric phase of the same fields as in Chapter 4. Chapter 6 evaluates coherences of forest and urban areas of F-SAR data and simulated Hydroterra time series. The intensity, coherence and interferometric phase of simulated time series with Hydroterra soil moisture for agriculture product (SSM Agro) parameters are presented in Chapter 7 and compared to the ones of F-SAR data. In Chapter 8 phase triplets analysis is performed to identify fields with moisture. The simulation procedure to obtain Hydroterra specific data sets with realistic wind effects is described in Chapter 9.

1.1 References

[1] SARSimHT Data Acquisition Report (Technical Report: DLR-HR-TR-SARSimHT-2019-001).

[2] DLR's Airborne SAR System F-SAR PRODUCT DESCRIPTION, Version: 3.2.
(Available: https://www.dlr.de/hr/Portaldata/32/Resources/images/institut/sar-technologie/f-sar/F-SAR_DIMS-products.pdf)

[3] Description of Simulated Amplitude Results for Hydroterra (Technical Report: DLR-HR-TR-SARSimHT-2019-002).

[4] Hydroterra Earth Explorer 10 Mission Candidate Mission Assumptions and Preliminary Technical Requirements (MATER).

[5] R. Scheiber, S.-K. Lee, K. P. Papathanassiou, N. Floury, "Extrapolation of Airborne Polarimetry and Interferometric SAR Data for Validation of Bio-Geo-Retrieval Algorithms for Future Spaceborne SAR Missions", Proc. IGARSS, Cape Town, 2009.

[6] J. Lee and E. Pottier, "Polarimetric Imaging: From Basics to Applications". Boca Raton, FL: CRC Press, 2009.

[7] J. C Curlander and R. N. McDonough, "Synthetic Aperture Radar: Systems and Signal Processing", 647 pp., John Wiley, New York, 1991.

[8] Description of Time Series with SSM Agro Parameters (Technical Report: DLR-HR-TR-SARSimHT-2019-004).

[9] F. De Zan, A. Parizzi, P. Prats-Iraola and P. López-Dekker, "A SAR Interferometric Model for Soil Moisture", IEEE Transactions Geoscience and Remote Sensing, vol. 52, no. 1, pp. 418–425, Jan. 2014.

[10] F. De Zan and G. Gomba, "Vegetation and Soil Moisture Inversion from SAR Closure Phases: First Experiments and Results", Remote Sensing of Environment, vol. 217, pp. 562–572, Nov. 2018.

[11] F. De Zan, M. Zonno and P. López-Dekker, "Phase Inconsistencies and multiple Scattering in SAR Interferometry", IEEE Transactions Geoscience and Remote Sensing, vol. 53, no. 12, pp. 6608–6616, Dec. 2015.

[12] BOREALSCAT, Second Data Analysis Report, L. Ulander and A. Monteith, Chalmers University of Technology, Gothenburg, Sweden ESA-contract 4000118576, CCN 1, v2, May 2020.

1.2 List of Abbreviations

ML	Multi-look
SLC	Single-Look Complex
NESZ	Noise Equivalent Sigma Zero
SNR	Signal-to-Noise Ratio

2 SARSimHT Study Overview

This chapter gives an overview of the airborne campaign which is used as basis for the SARSimHT 2019 study and of some previous results.

The airborne campaign took place on July 9th, 2019. During this experiment, two flights were performed. The first flight started in the morning and the second one in the afternoon. The data were collected with DLR's airborne radar system F-SAR. Table 2.1 summarizes the radar parameters used for the data processing. A more detailed description of the airborne campaign can be found in [1].

The test site was around Kaufbeuren, which is a small town in Bavaria, Germany. During the SARSimHT airborne flight campaign, three teams collected ground truth data at different survey points at the test site. In total, measurements at 123 survey points were acquired. The main goal of the ground truth data collection was to investigate the vegetation type and height at the test site. The day before and the day after the airborne experiment, another team also collected 673 aerial views from drone flights at three different areas inside the test site. Figure 2.1 shows all available survey points and drone image positions at the test site. In Chapters 4 and 5 some of the survey points are used to investigate the properties of radar data in more detail.

To simulate the long integration time of Hydroterra, data of the test site were repeatedly collected to acquire an image stack of 13 stripmap SAR images with zero spatial baseline and 8-9 minutes temporal baseline. This acquisition procedure was used for the first and the second flight. A simulated integration time of 1 hour and 41 minutes for the first flight and 1 hour and 44 minutes for the second flight was achieved with the described procedure. Figure 2.2 visualizes this acquisition procedure.

Figure 2.3 describes the simulation procedure which was used to acquire simulated Hydroterra SLC products from the collected image stacks. To simulate a Hydroterra product, an image stack with zero spatial baseline of F-SAR data is needed, which is described in more detail in [1]. For this study two image stacks are available, which were collected during two different flights with the airborne radar system F-SAR. The simulation procedure is as follows: First a master is chosen from the image stack. Then each image of the image stack is coregistered to the master geometry, filtered to the desired resolution in azimuth and slant range, and finally normalized in terms of energy [5]. In the next step, an interferometric calibration is performed in order to properly align coherently the images. This is performed by subtracting the phase difference between the master image and the image, i.e., the interferometric phase, to the slave images. After the phase calibration, each image is Fourier transformed to the azimuth frequency domain, where a different bandpass filter is applied to each image, as sketched in Figure 2.3. This bandpass filter is needed to simulate the slow velocity of a satellite in a geosynchroneous orbit. The bandwidth and centre frequency of each band pass filter is calculated to ensure the desired final resolution of the Hydroterra product. An overlap of 50% between adjacent bands is performed by using a feathering function. An overlap is needed to eliminate phase jumps in the final product, which otherwise would degrade the final simulated Hydroterra product, something which is not occurring in a real Hydroterra product. Phase jumps occur because spectra from different images are combined; implying different phase offsets at the edges between the spectra might be present. The feathering function ensures a smooth transition between bands. After bandpass filtering, all images are coherently combined in the azimuth frequency domain by simply adding them. Due to the time span between the first and the last F-SAR acquisitions (about one hour and forty-five minutes), this simulation corresponds to the long integration time of the Hydroterra mission. In the last step, an inverse Fourier transform in the azimuth domain is performed and the noise equivalent sigma zero (NESZ) of the product is adjusted to the one of a Hydroterra product, as

described in [5]. The result of this simulation is a simulated Hydroterra single-look complex product. Additionally, multi-looking is performed to obtain simulated Hydroterra multi-looked products. This procedure is also described in [3]. The simulated Hydroterra products are presented in Chapter 3.

Center Frequency	5300 MHz (C-band)
Range Bandwidth	384 MHz
Range Sampling Frequency (RSF)	500 MHz
Chirp Length	10 µs
Azimuth Bandwidth	257.33 Hz
Pulse Repetition Frequency (PRF) (after pre-summing)	300.25 Hz
Polarization	Fully polarimetric
3dB-beamwidth	23° in elevation, 12° in azimuth
Resolution	0.5 m in slant range, 0.5 m in azimuth
Sampling	0.30 m in slant range, 0.33 m in azimuth
Number of Samples	7536 in slant range, 19456 in azimuth

Table 2.1: Radar parameters used for data processing.

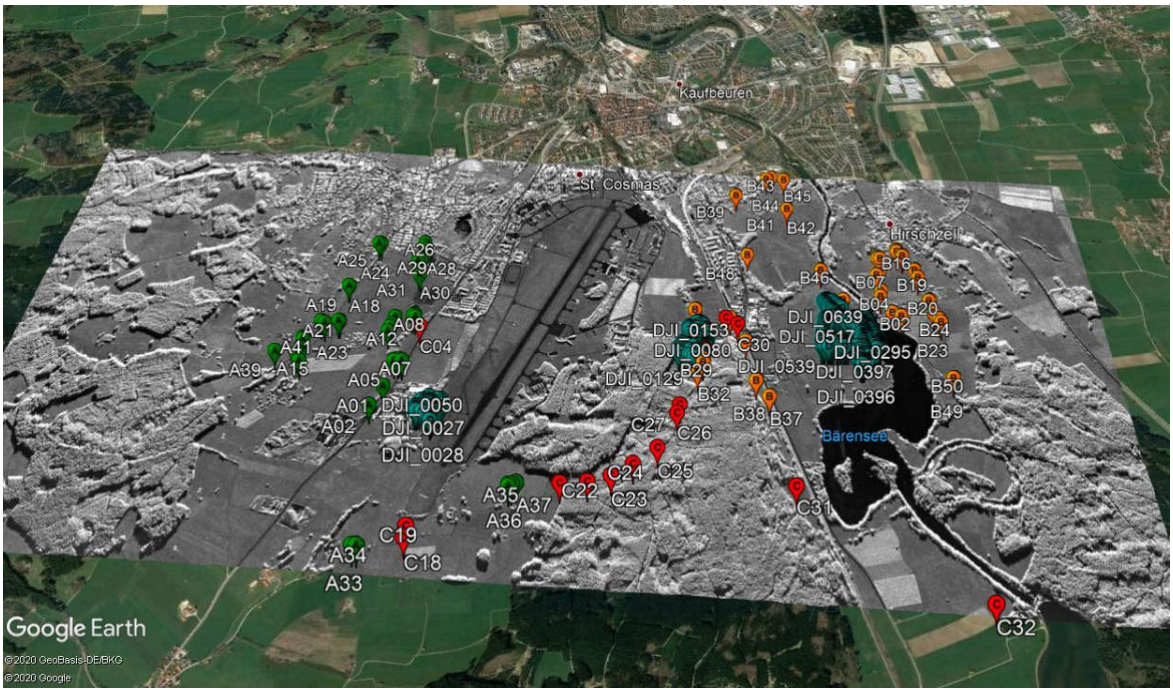

Figure 2.1: All collected survey points of ground truth data of three teams (A (green), B (orange), C (red)). The survey points are displayed on the geocoded amplitude of the first acquisition in Google Earth. In blue also the drone image positions are visualized (DJI_*).

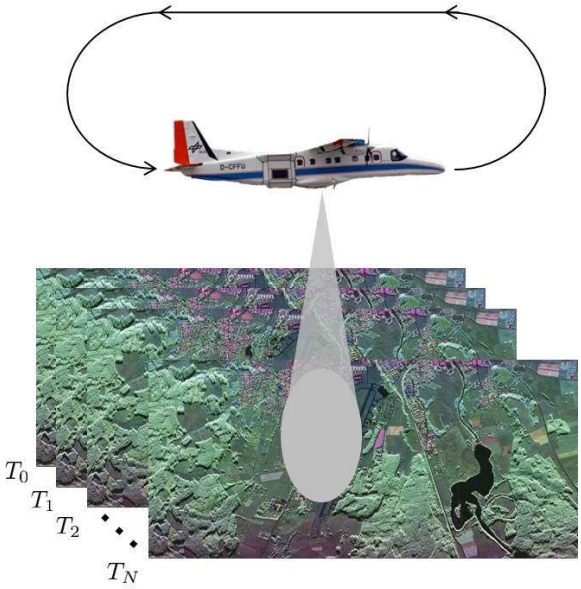

Figure 2.2: Acquisition procedure of Hydroterra airborne experiment.

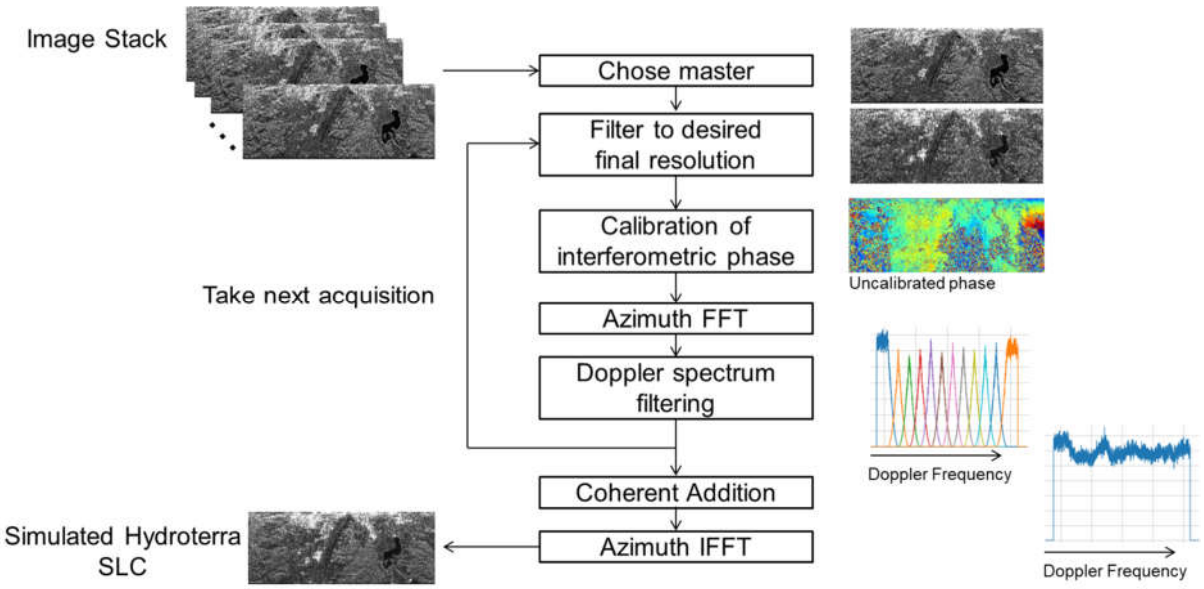

Figure 2.3: Simulation procedure to acquire simulated Hydroterra SLC products

3 Simulated Hydroterra Products

3.1 Simulated Hydroterra Amplitude Products

As part of 'WP220 – Hydroterra Image Simulation', DLR has simulated single-look complex (SLC) and multi-look detected (ML) Hydroterra images. The data will be delivered to ESA in the following format:

- slc_ht_flX_YY.rat
- slc_pp_ht_flX_YY.xml
- ml_ht_flX_YY.rat
- ml_pp_ht_flX_YY.xml

Here "X" corresponds to the flight number and "YY" to the polarization.

To simulate the Hydroterra products, the current parameters of the scenario 4 of the interferomet-ric type (Glacier flow/ Landslides) were used, because this product has the highest resolution of all defined Hydroterra products. A high resolution is preferable for the amplitude and phase analysis of this study. In Table 3.1.1 the relevant parameters are summarized.

Parameter	Value
Single-look azimuth resolution	5 m
Multi-look azimuth resolution	50 m
Number of azimuth looks	10
Range bandwidth	6 MHz
Single-look slant range resolution	22.2 m
Multi-look slant range resolution	22.2 m
Number of range looks	1
Noise Equivalent Sigma Zero	-21.1 dB

Table 3.1.1: Relevant parameters of scenario 4 of the interferometric type used for Hydroterra product simulation.

Figures 3.1.1-3.1.3 show the simulated Hydroterra single-look complex (SLC) products for the different polarizations for both flights. On the left side of these figures also a normal SLC image of the first acquisition with adjusted resolution and NESZ is displayed. Significant image degradation between the SLC and the simulated Hydroterra images is not visible. A more detailed analysis of the image quality will be performed in Chapter 3.2.

Figure 3.1.4 shows the Pauli composite images of one acquisition and the simulated Hydroterra products of both flights. Pauli composite images are useful, because their components have a physical meaning [6]. The red color in Figure 3.1.4 corresponds to the component HH-VV, which is due to even bounce scattering. The green color in Figure 3.1.4 visualizes the component 2*HV which is due to volume scattering and the blue color shows the component due to odd bounce scattering, which can be calculated from HH+VV.
Figures 3.1.5 - 3.1.7 show the multi-look detected simulated Hydroterra amplitude image products in slant range geometry for different polarizations and with adjusted NESZ. On the left side the simulated Hydroterra image product of flight 1 is displayed and on the right side the one of flight 2 is shown.

Figure 3.1.8 shows the simulated Hydroterra SLC amplitude image products and Figure 3.1.9 the

multi-look detected simulated Hydroterra amplitude image products for the HH polarization with an integration time of 43 minutes instead of 1 hour and 41 minutes for both flights. The resolution in azimuth reduces therefore from 5 m to 10 m in the SLC image and from 50 m to 108 m in the multi-look detected image. Figure 3.1.10 shows the simulated Hydroterra SLC amplitude image products and Figure 3.1.11 the multi-look detected simulated Hydroterra amplitude image products for the HH polarization with an integration time of 18 minutes for both flights. This reduces the azimuth resolution to 17.5 m for the SLC and 216 m for the multi-look detected image. A coarser azimuth resolution is evident in Figures 3.1.8-3.1.11. Simulated Hydroterra amplitude products with a shorter integration time will be delivered to ESA in the following format:

- slc_ht_intTimeZmin_flX_YY.rat
- slc_pp_ht_ intTimeZmin_flX_YY.xml
- ml_ht_flX_ intTimeZmin_YY.rat
- ml_pp_ht_flX_ intTimeZmin_YY.xml

Here "X" corresponds to the flight number, "YY" to the polarization and "Z" to the integration time in minutes.

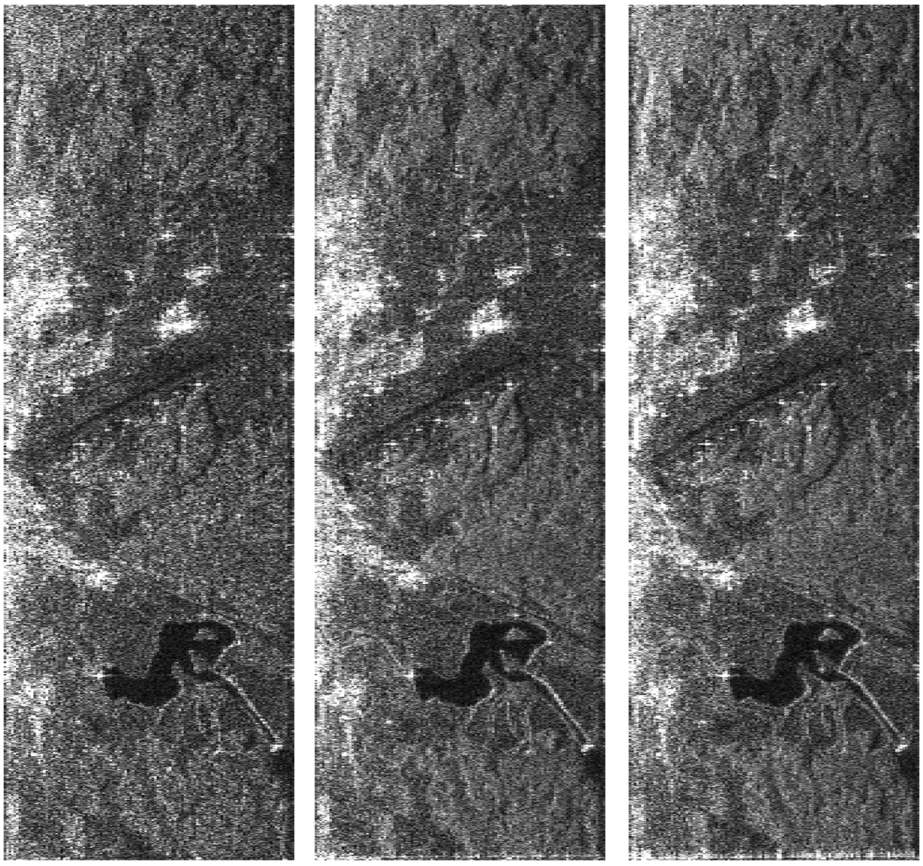

Figure 3.1.1: Single-look complex images in slant range geometry of HH polarisation. Left: One acquisition with adjusted resolution (5 m x 22.2 m) and NESZ (-21.1 dB), middle: Simulated Hydroterra amplitude product of flight 1 (integration time: 1 hour and 41 minutes), right: Simulated Hydroterra amplitude product of flight 2 (integration time: 1 hour and 44 minutes).

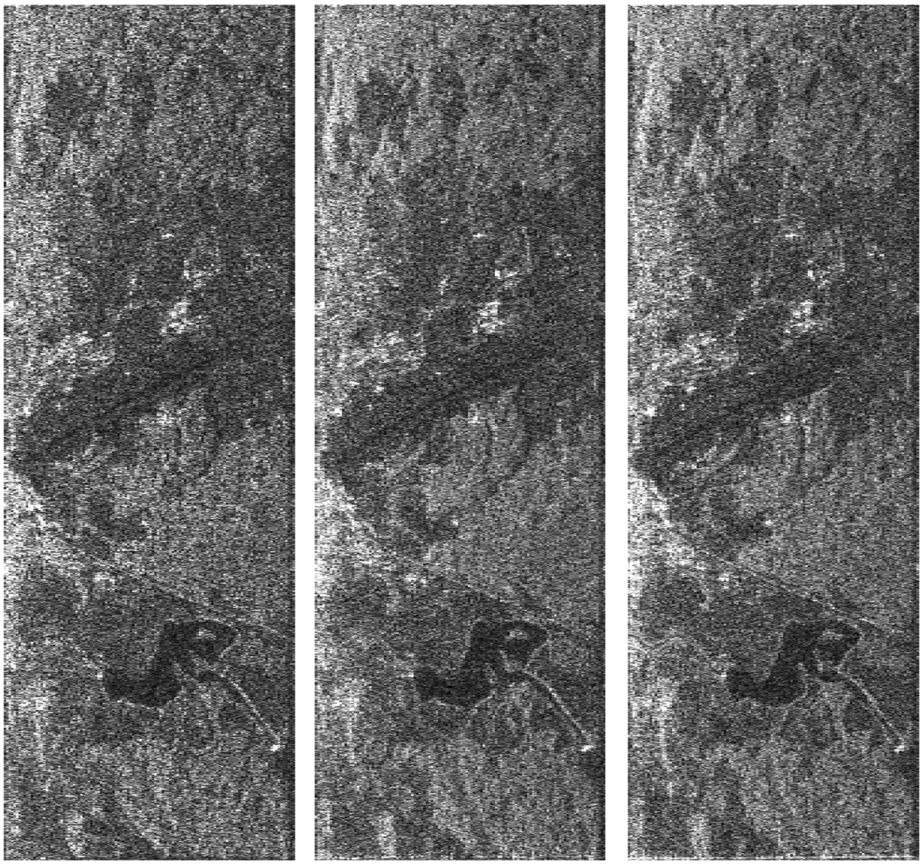

Figure 3.1.2: Single-look complex images in slant range geometry of HV polarisation. Left: One acquisition with adjusted resolution (5 m x 22.2 m) and NESZ (-21.1 dB), middle: Simulated Hydroterra amplitude product of flight 1 (integration time: 1 hour and 41 minutes), right: Simulated Hydroterra amplitude product of flight 2 (integration time: 1 hour and 44 minutes).

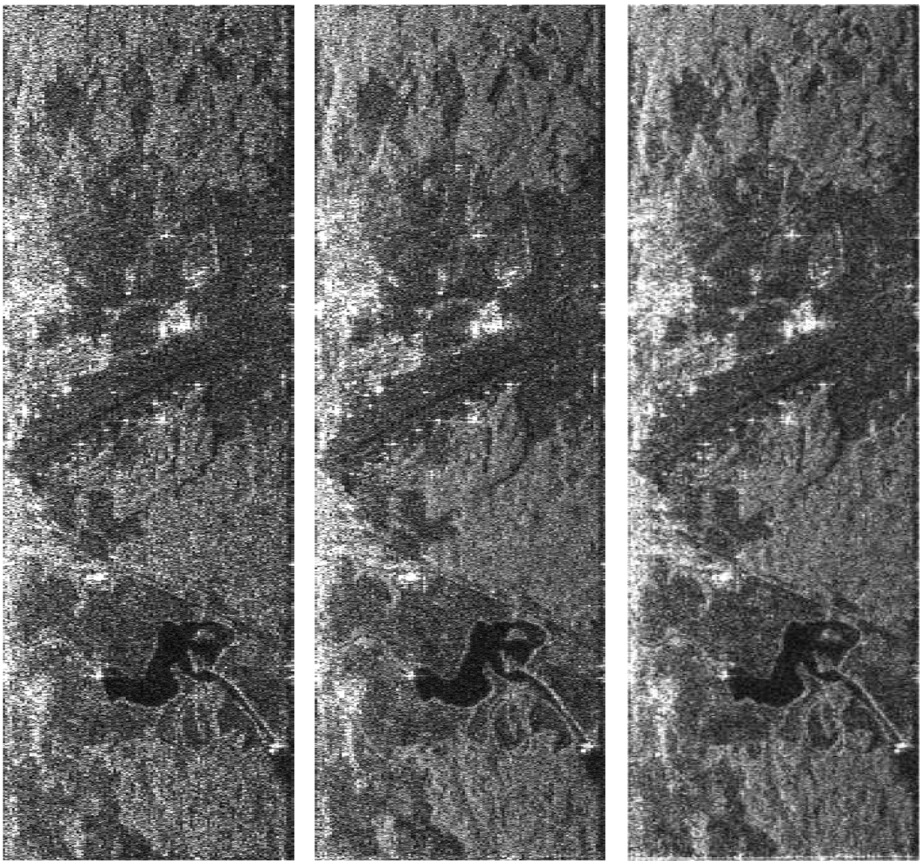

Figure 3.1.3: Single-look complex images in slant range geometry of VV polarisation. Left: One acquisition with adjusted resolution (5 m x 22.2 m) and NESZ (-21.1 dB), middle: Simulated Hydroterra amplitude product of flight 1 (integration time: 1 hour and 41 minutes), right: Simulated Hydroterra amplitude product of flight 2 (integration time: 1 hour and 44 minutes).

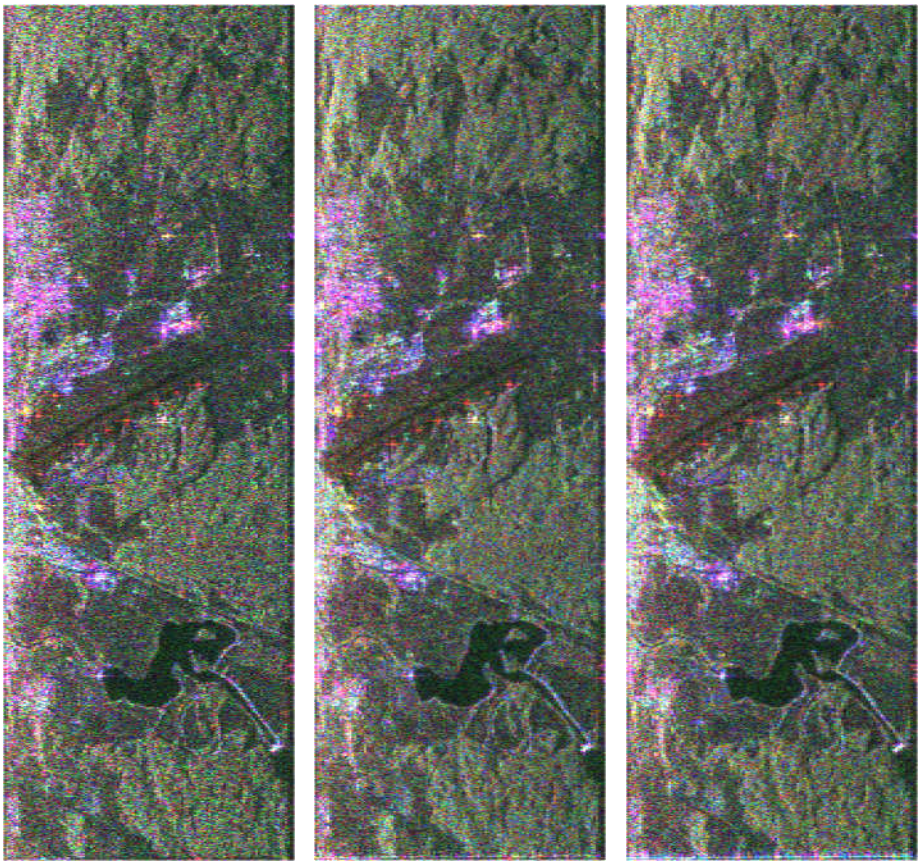

Figure 3.1.4: Pauli composite images (Red: Even bounce scattering, green: Volume scattering, blue: Odd bounce scattering). Left: One acquisition with adjusted resolution and NESZ (-21.1 dB), middle: Simulated Hydroterra amplitude product of flight 1 (integration time: 1 hour and 41 minutes), right: Simulated Hydroterra amplitude product of flight 2 (integration time: 1 hour and 44 minutes).

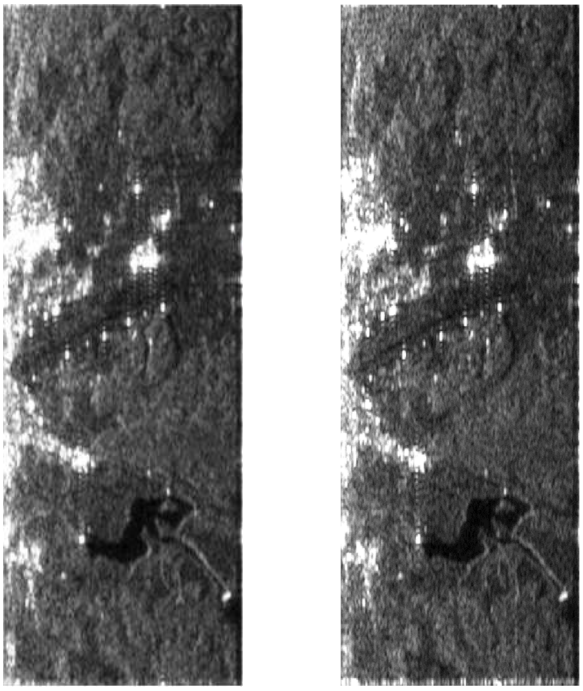

Figure 3.1.5: Amplitude of multi-look detected simulated Hydroterra amplitude products in slant range geometry of HH polarisation. Left side: Simulated Hydroterra amplitude product of flight 1 (integration time: 1 hour and 41 minutes), right side: Simulated Hydroterra amplitude product of flight 2 (integration time: 1 hour and 44 minutes).

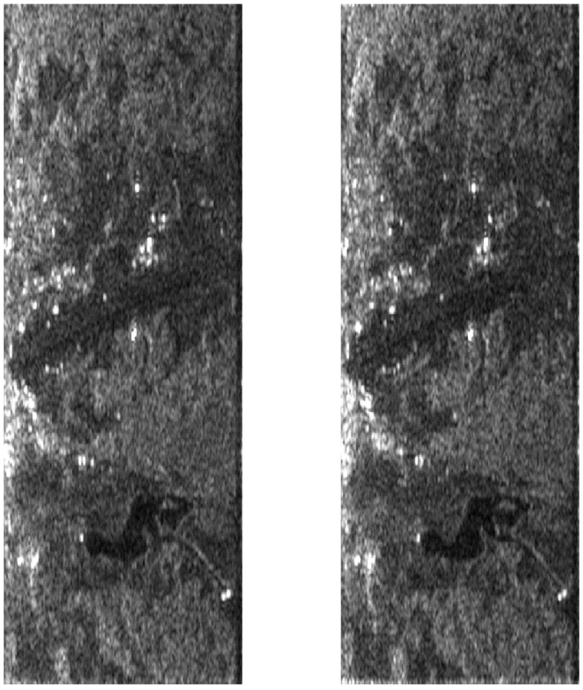

Figure 3.1.6: Amplitude of multi-look detected simulated Hydroterra amplitude products in slant range geometry of HV polarisation. Left side: Simulated Hydroterra amplitude product of flight 1 (integration time: 1 hour and 41 minutes), right side: Simulated Hydroterra amplitude product of flight 2 (integration time: 1 hour and 44 minutes).

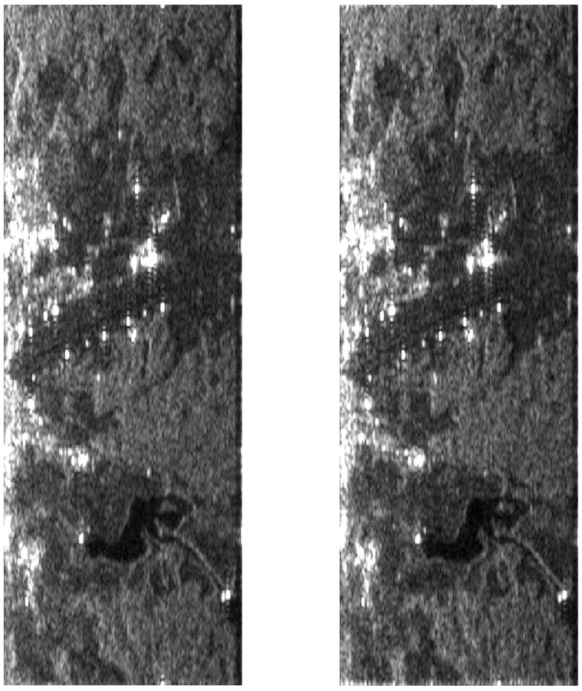

Figure 3.1.7: Amplitude of multi-look detected simulated Hydroterra amplitude products in slant range geometry of VV polarisation. Left side: Simulated Hydroterra amplitude product of flight 1 (integration time: 1 hour and 41 minutes), right side: Simulated Hydroterra amplitude product of flight 2 (integration time: 1 hour and 44 minutes).

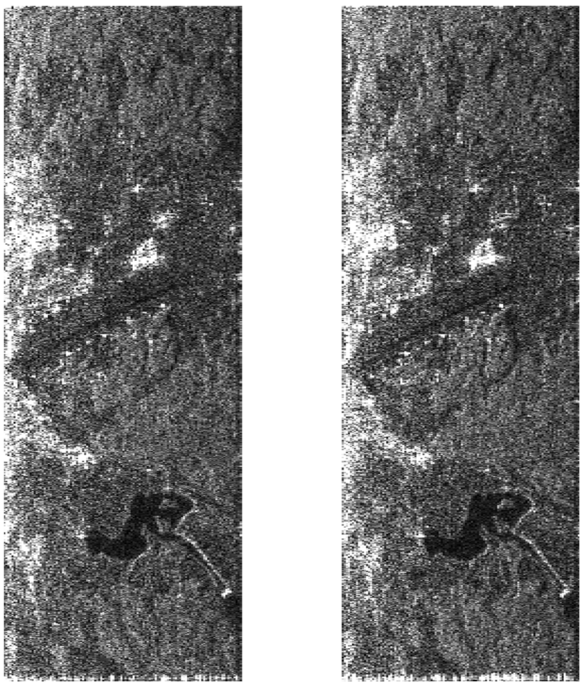

Figure 3.1.8: Amplitude of single-look complex simulated Hydroterra amplitude products in slant range geometry of HH polarisation for 43 minutes integration time. Left side: Simulated Hydroterra amplitude product of flight 1, right side: Simulated Hydroterra amplitude product of flight 2.

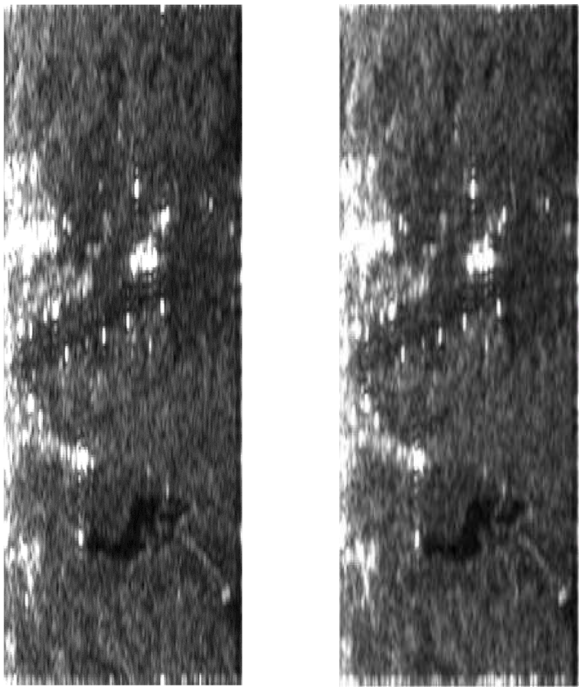

Figure 3.1.9: Amplitude of multi-look detected simulated Hydroterra amplitude products in slant range geometry of HH polarisation for 43 minutes integration time. Left side: Simulated Hydroterra amplitude product of flight 1, right side: Simulated Hydroterra amplitude product of flight 2.

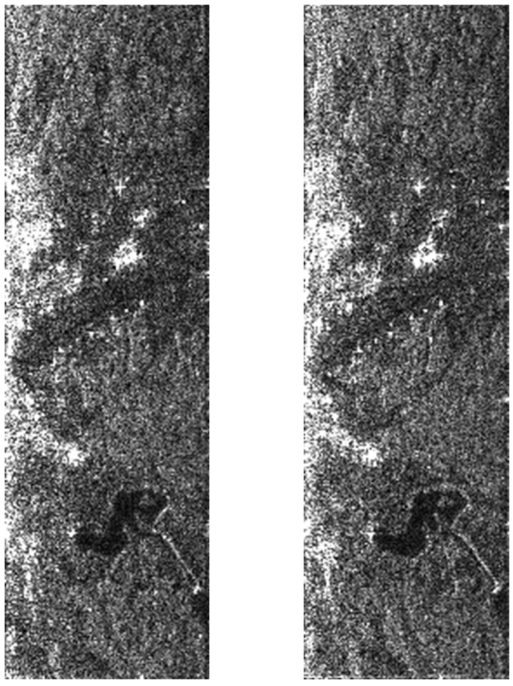

Figure 3.1.10: Amplitude of single-look complex simulated Hydroterra amplitude products in slant range geometry of HH polarisation for 18 minutes integration time. Left side: Simulated Hydroterra amplitude product of flight 1, right side: Simulated Hydroterra amplitude product of flight 2.

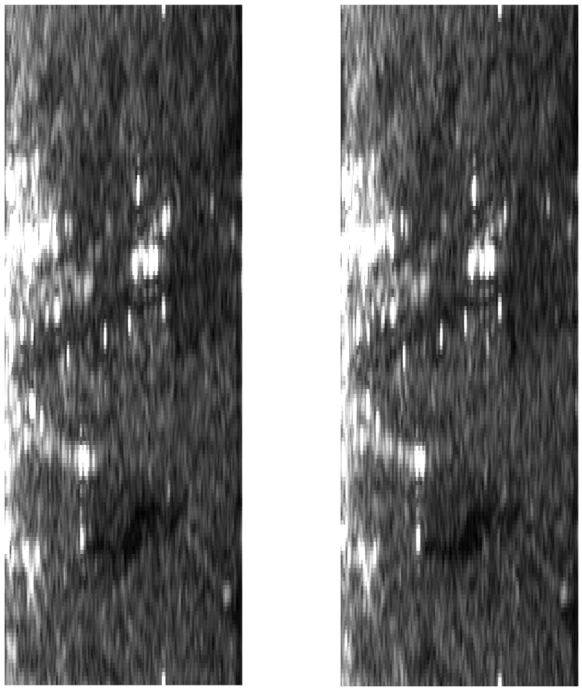

Figure 3.1.11: Amplitude of multi-look detected simulated Hydroterra amplitude products in slant range geometry of HH polarisation for 18 minutes integration time. Left side: Simulated Hydroterra amplitude product of flight 1, right side: Simulated Hydroterra amplitude product of flight 2.

3.2 Image Quality Analysis

The purpose of this section is to compare the image quality of simulated Hydroterra amplitude products to the image quality of a normal SLC and evaluate if an image quality degradation occurred due to the long integration time of Hydroterra.

One possibility to evaluate the image quality of an image is by calculating its contrast. The contrast can be calculated from [7]

$$C = \frac{Var\{I\}}{(E\{I\})^2} \leq 1.$$

Here I is the magnitude of the image, $Var\{\}$ denotes the variance and $E\{\}$ the expectation value. The contrast ranges between 0 and 1, where 0 is the lowest contrast and 1 the highest one. Higher contrast indicates better image quality if the same scene is analysed.

Figure 3.2.1 shows the contrast of a normal SLC and of simulated Hydroterra images. The contrast was calculated with a sliding window. In Figure 3.2.1 a higher contrast is visible for the SLC of a single acquisition than for the Hydroterra products. This is especially evident in forested areas. The contrast in forested areas is lower for Hydroterra images, because the movement of the trees during the integration time defocusses the image, i.e., the clutter level is increased at the neighbouring pixels.

Figure 3.2.2 shows histograms of the calculated contrasts in Figure 3.2.1. Also this Figure shows that the contrast is higher for the SLC of a single acquisition than for the Hydroterra images. The mean contrast is 0.306 for the SLC of a single acquisition, 0.210 for the simulated Hydroterra product of the first flight and 0.209 for the simulated Hydroterra product of the second flight.

Figures 3.2.3 and 3.2.4 show the calculated contrast with a sliding window and the histograms of the contrast for Hydroterra products with an integration time of 18 minutes and the according SLC of a single acquisition. The sliding window was chosen to have the same resolution as in Figure 3.2.1. The difference between the contrast of the SLC of a single acquisition and the Hydroterra images is lower. The mean contrast is 0.308 for the SLC of a single acquisition, 0.235 for the simulated Hydroterra product of the first flight and 0.231 for the simulated Hydroterra product of the second flight. The difference of the contrast is smaller for the shorter integration time, because the forested areas are less defocussed.

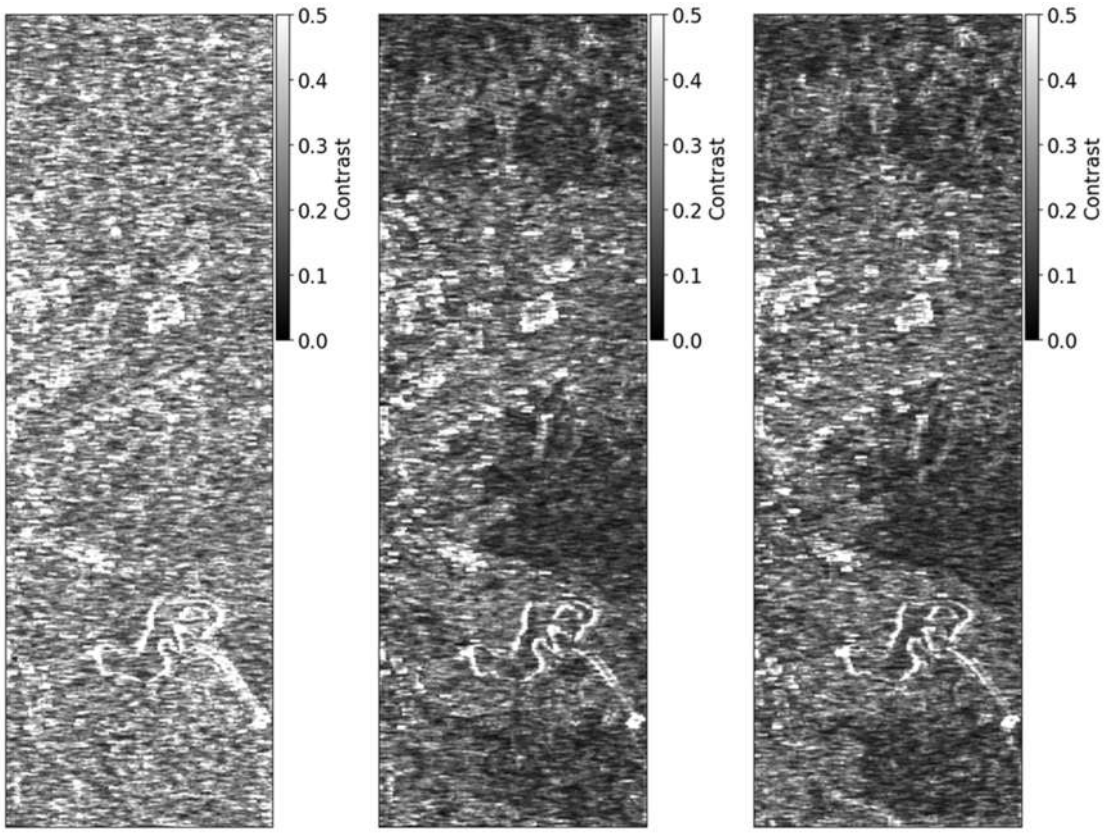

Figure 3.2.1: Contrast calculated with a sliding window for products with 1 hour and 41 minutes integration time. Left: One acquisition with adjusted resolution and NESZ, middle: Simulated Hydroterra amplitude product of flight 1, right: Simulated Hydroterra amplitude product of flight 2.

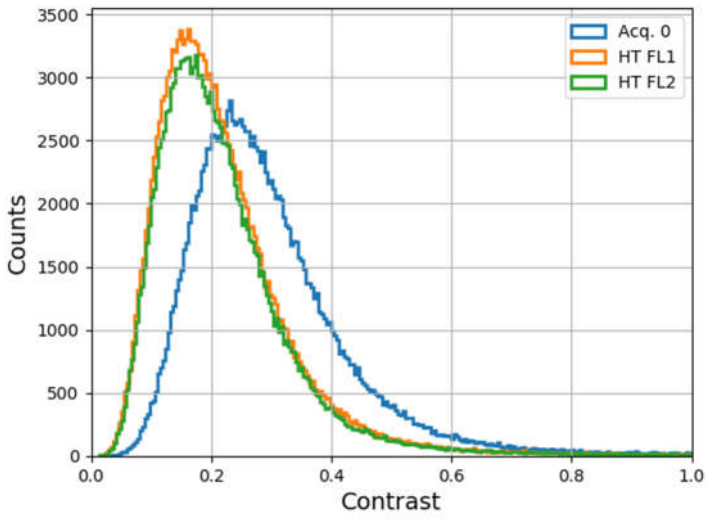

Figure 3.2.2: Histograms of calculated contrasts from Figure 3.2.1.

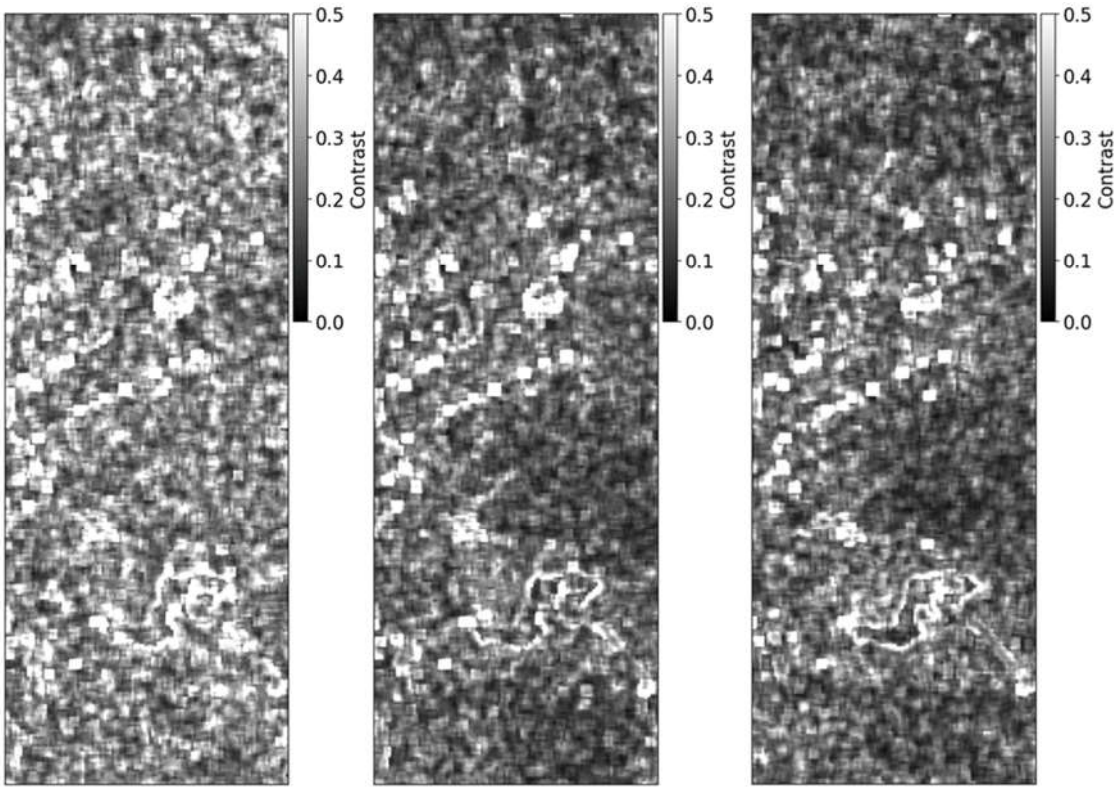

Figure 3.2.3: Contrast calculated with a sliding window for products with 18 minutes integration time. Left: One acquisition with adjusted resolution and NESZ, middle: Simulated Hydroterra amplitude product of flight 1, right: Simulated Hydroterra amplitude product of flight 2.

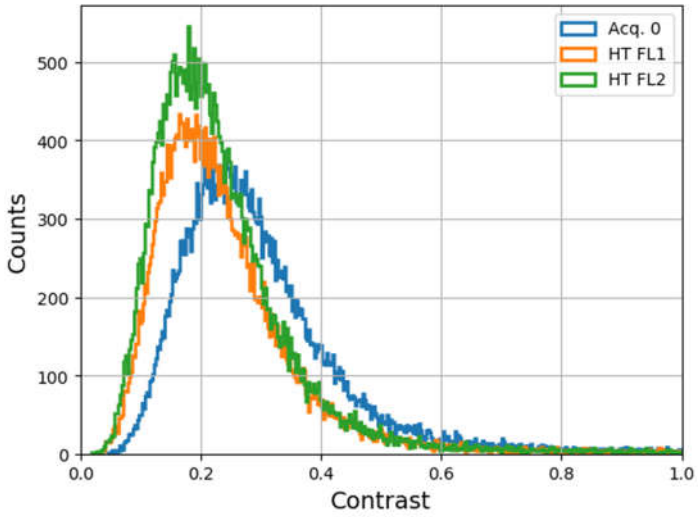

Figure 3.2.4: Histograms of calculated contrasts from Figure 3.2.3.

3.3 Simulated Hydroterra Coherence and Interferometric Phase Products

During the airborne experiment, two flights were performed, one in the morning and one in the afternoon. This allows to simulate two Hydroterra single-look complex products which can be used to process coherence and interferometric phase products. From now on an integration time of 1 hour and 41 minutes is considered.

As part of 'WP300 – Hydroterra INSAR Simulation and Analysis', DLR has processed coherence and interferometric phase products from the simulated Hydroterra products of both flights. The data will be delivered to ESA in the following format:

- coh_ht_flX_YY.rat
- pha_ht_flX_YY.rat
- ppinsar_ht_flX_YY.xml

Here "X" corresponds to the flight number and "YY" to the polarization. The processing parameter file "ppinsar_ht_flX_YY.xml" and the rat format are described in more detail in [2].

Figure 3.3.1 shows the coherence of simulated Hydroterra products for the HH, HV and VV polarisations. The coherence was calculated with a moving average window. The HV coherence is smaller, because the signal-to-noise ratio (SNR) of this polarisation is lower. As one would expect, Figure 3.3.1 shows lower coherence in forested areas and higher coherence in field and urban areas.

In Figures 3.3.2 - 3.3.4 histograms of coherences between the first acquisition of the first flight as master and all acquisitions of the second flight for the polarisations HH, HV and VV are displayed. The resolution and NESZ of all acquisitions was adjusted to the ones of the simulated Hydroterra products. Additionally, the black line in Figures 3.3.2 - 3.3.4 indicates the histogram of the simulated Hydroterra coherence product. Figures 3.3.2 - 3.3.4 show that the coherence of simulated Hydroterra products is similar to the coherence of single acquisitions. A more detailed comparison between the coherences of single acquisitions and the coherence of simulated Hydroterra products will be performed in Chapters 5 and 6.

Figure 3.3.5 shows the interferometric phase of simulated Hydroterra products for the HH, HV and VV polarisations. Also here the interferometric phase is noisier for the HV polarisation due to the lower SNR.

The histograms of the interferometric phases for the different polarisations are visualized in Figures 3.3.6 – 3.3.8. Here the coloured lines indicate the histograms of the interferometric phase between the first acquisition of the first flight as master and all acquisitions of the second flight. The black line shows the histogram of the interferometric phase between the two simulated Hydroterra products. Figures 3.3.6 - 3.3.8 indicate a similar interferometric phase of the simulated Hydroterra products as compared to the interferometric phase of single acquisitions.

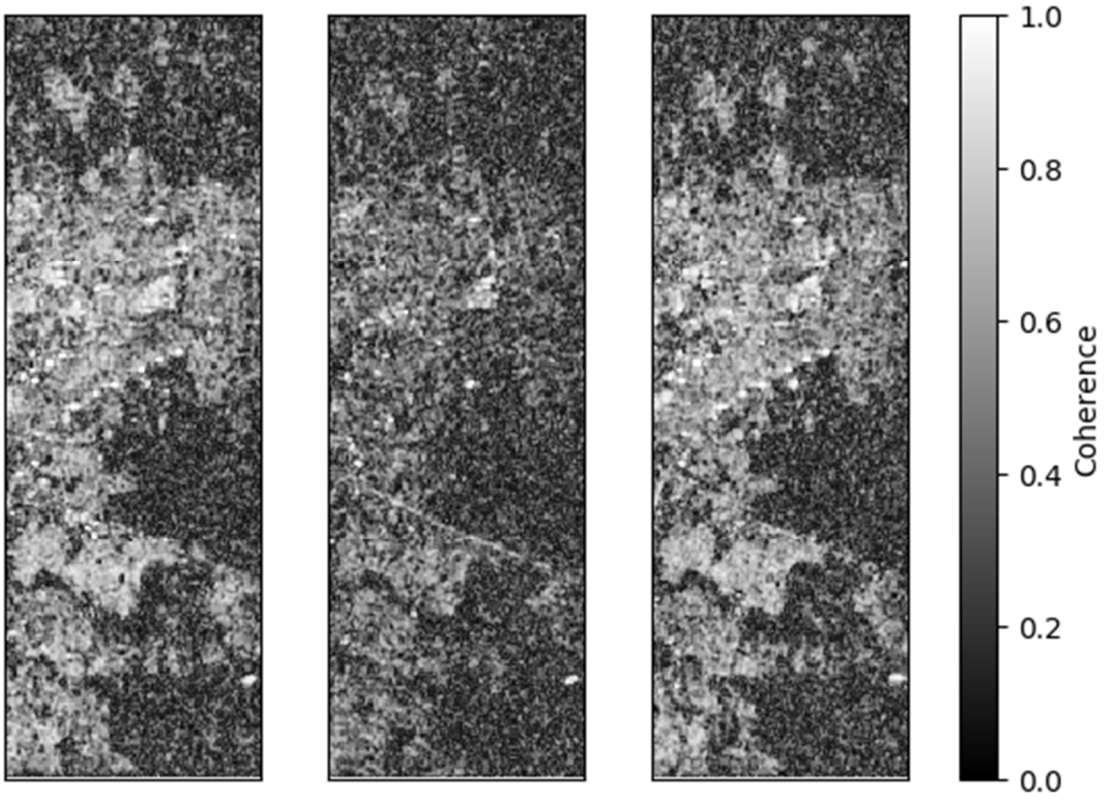

Figure 3.3.1: Coherence of simulated Hydroterra products. Left: HH polarisation, middle: HV polarisation, right: VV polarisation.

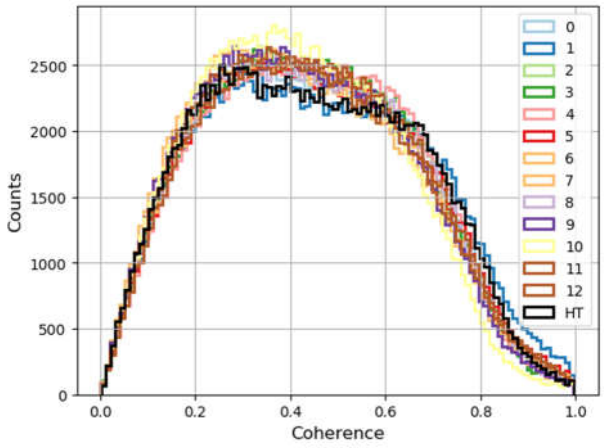

Figure 3.3.2: Histograms of coherences between the first acquisition of the first flight as master and acquisitions of the second flight as slave. The numbers indicate the considered acquisition of the slave. The black line is the coherence of the simulated Hydroterra products (HT) for the HH polarisation.

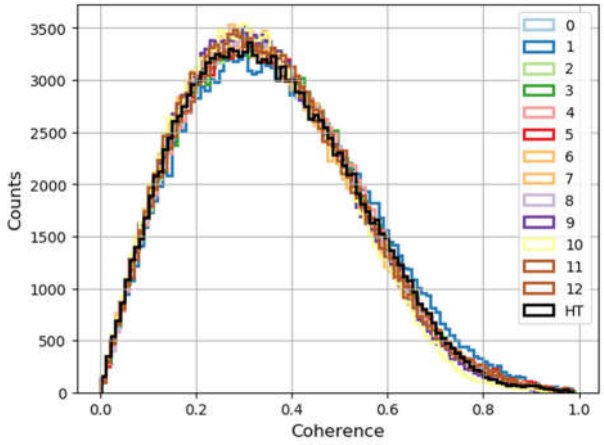

Figure 3.3.3: Histograms of coherences between the first acquisition of the first flight as master and acquisitions of the second flight as slave. The numbers indicate the considered acquisition of the slave. The black line is the coherence of the simulated Hydroterra products (HT) for the HV polarisation.

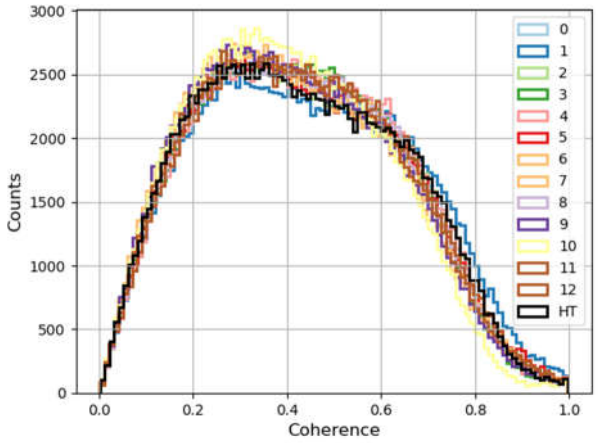

Figure 3.3.4: Histograms of coherences between the first acquisition of the first flight as master and acquisitions of the second flight as slave. The numbers indicate the considered acquisition of the slave. The black line is the coherence of the simulated Hydroterra products (HT) for the VV polarisation.

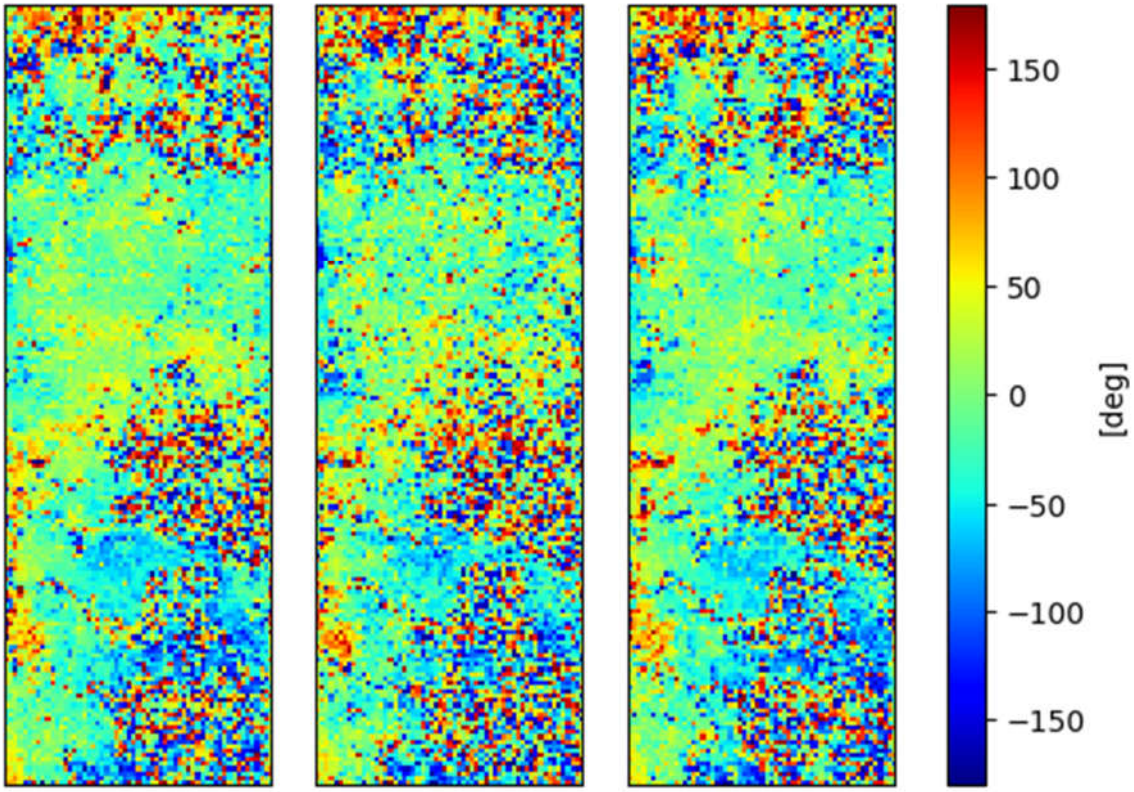

Figure 3.3.5: Interferometric phase of simulated Hydroterra products. Left: HH polarisation, middle: HV polarisation, right: VV polarisation.

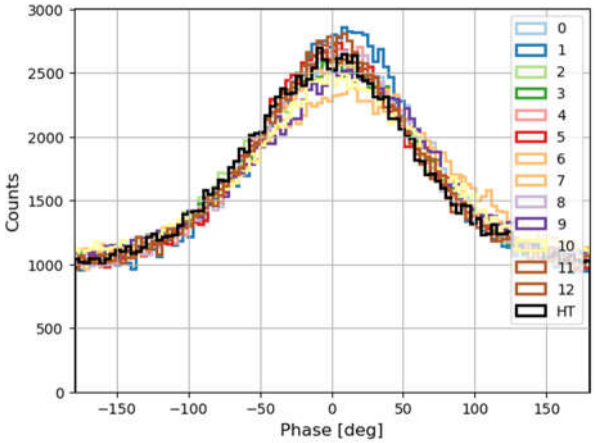

Figure 3.3.6: Histograms of interferometric phase between the first acquisition of the first flight as master and acquisitions of the second flight as slave. The numbers indicate the considered acquisition of the slave. The black line is the interferometric phase of the simulated Hydroterra products (HT) for the HH polarisation.

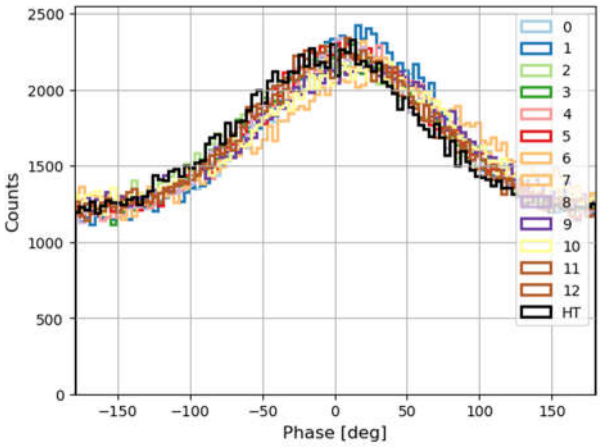

Figure 3.3.7: Histograms of interferometric phase between the first acquisition of the first flight as master and acquisitions of the second flight as slave. The numbers indicate the considered acquisition of the slave. The black line is the interferometric phase of the simulated Hydroterra products (HT) for the HV polarisation.

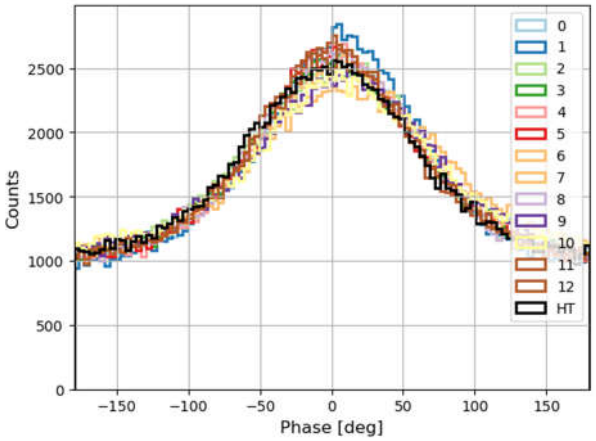

Figure 3.3.8: Histograms of interferometric phase between the first acquisition of the first flight as master and acquisitions of the second flight as slave. The numbers indicate the considered acquisition of the slave. The black line is the interferometric phase of the simulated Hydroterra products (HT) for the VV polarisation.

4 Survey Points Analysis

Ground truth measurements were collected during the airborne campaign for the SARSimHT study. For the ground truth measurement collection the vegetation type and vegetation height were collected at 123 survey points. The ground truth measurements are described in more detail in [1].
In this chapter six survey points are chosen to analyse the intensity, coherence and interferometric phase in dependence of the vegetation. This is part of the work package WP300.
Figure 4.1 shows the positions of the survey points in the Pauli image. The different parameters are estimated from a set of pixels around the survey points. In this chapter the analysis is performed on F-SAR data with the original F-SAR parameters. Parameters relevant for this analysis are summarized in Table 4.1. Figure 4.2 shows the NESZ in dependence of the off-nadir angle and Table 4.2 outlines the SNR in dB for the six survey points and the different polarizations. The SNR was calculated by using the NESZ from Figure 4.2. In Chapter 5 the same analysis will be performed on data with Hydroterra parameters of the scenario 4.
Figures 4.3 - 4.7 show photographs of the survey points which will be analysed in this chapter. In Figure 4.3 the vegetation at survey point "A16" is visible, where corn was growing with a measured height of 190 cm. The vegetation of the survey point "B01" is shown in Figure 4.4, where oat can be seen. The height of the oat was measured as 100 cm. Figures 4.5 and 4.6 visualize the vegetation type at the survey points "B18" and "B22", which was grass for both survey points. The grass height at "B18" was 10 – 20 cm and 60 – 70 cm at "B22" during the data acquisition. Figure 4.7 shows the survey point "A30". Here the vegetation type was grass with a height of 3 cm. This survey point is interesting, because the ground measurement team observed at 12:40 local time, which is between the first and second flight, how the grass was cut and watered. In Figure 4.8 two photographs of the survey point "B03" are shown, where the vegetation type is grass with a height of 40 cm.
The survey points "B18" and "B22" were chosen, because grass was the typical vegetation type at this test site. These two survey points are therefore representative for several other survey points. The survey points "A16" and "B01" were chosen to analyse the impact of other vegetation type then grass. The survey point "B03" was chosen, because a strong close phase can be estimated around this survey point, as will be discussed in Chapter 8.

Parameter	Value
Single-look azimuth resolution	0.5 m
Single-look slant range resolution	0.5 m
Pixel spacing in azimuth	0.3342 m
Pixel spacing in range	0.2997 m

Table 4.1: Relevant radar parameters of F-SAR data.

Survey Point	SNR for HH [dB]	SNR for HV [dB]	SNR for VV [dB]
"A16"	31.73	23.86	29.87
"B01"	33.93	23.88	30.83
"B18"	30.99	23.60	28.85
"B22"	31.13	24.32	28.94
"A30"	27.57	20.91	27.45
"B03"	31.85	24.75	30.23

Table 4.2: Signal-to-Noise Ratio (SNR) for the 5 survey points and all polarizations.

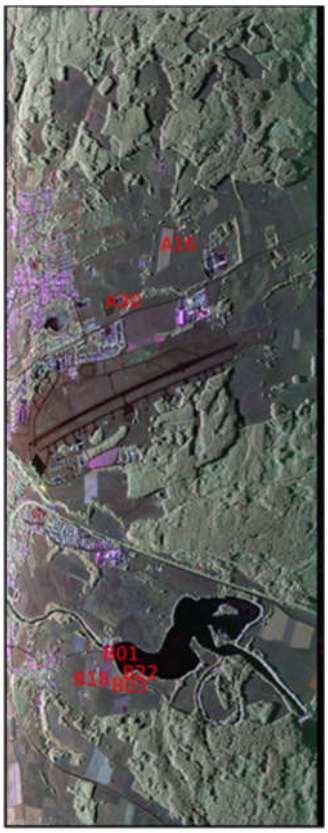

Figure 4.1: All survey points which will be further analysed in this chapter in Pauli composite image. (Red: Even bounce scattering, green: Volume scattering, blue: Odd bounce scattering).

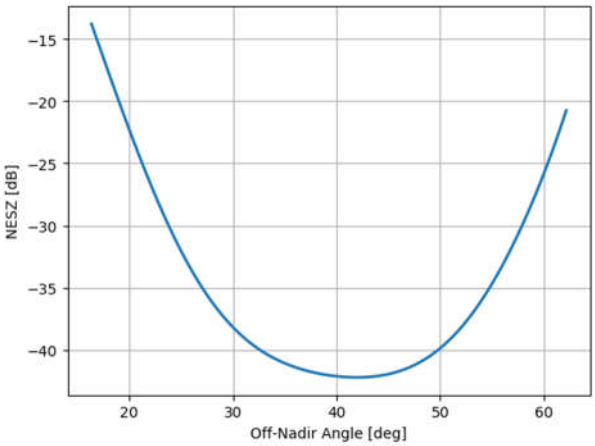

Figure 4.2: Noise Equivalent Sigma Zero (NESZ) of F-SAR data in dB in dependence of the off-nadir angle.

Figure 4.3: Two photographs of survey point "A16".

Figure 4.4: Two photographs of survey point "B01".

Figure 4.5: Two photographs of survey point "B18".

Figure 4.6: Two photographs of survey point "B22".

Figure 4.7: Two photographs of survey point "A30".

Figure 4.8: Two photographs of survey point "B03".

4.1 Intensity Analysis at Survey Points

In this section the intensity of Pauli composites at the 6 survey points is analysed. The Pauli decomposition is performed, because the different composites have physical meanings which facilitate the interpretation of the different results, namely, HH-VV represents the even bounce scattering, HH+VV the odd bounce scattering, and 2HV the volume scattering.

Figures 4.1.1 – 4.1.5 show on the left side a section of the Pauli composite image around the area of each survey point. The red rectangle indicates the exact area which is used for the intensity analysis but also for the coherence and interferometric phase analysis in Chapters 4.2 and 4.3. The right side of Figures 4.1.1 – 4.1.5 shows the intensities averaged over the area indicated by the red rectangle for each survey point. The red line indicates the intensity from even bounce scattering, the green line is due to volume scattering and the blue line shows the odd bounce scattering. For all survey points the highest intensity comes from the odd bounce scattering, which is considered to be the scattering from the surface. The intensity is evaluated for each acquisition of the two flights. The black dotted line in the middle of the image indicates when the acquisitions correspond to the second flight.

In Figures 4.1.1 and 4.1.2 no difference of the intensity between the first and second flight is visible. In these figures the survey points "A16"and "B01" are evaluated, where at both survey points high vegetation was recorded.

In Figures 4.1.3 and 4.1.4, however, a drop of around 0.5 dB is visible between flight 1 and flight 2 for the odd bounce scattering and the volume scattering component. One possible reason for this drop is moisture. Heavy rainfall occurred during the night before the airborne campaign and the ground measurement teams reported that the grass was wetter in the morning than in the afternoon.

The right side of Figure 4.1.5 shows the intensity of Pauli composites of the survey point "A30". Here the intensity rises between the first and second flight. This rise is especially evident for the odd bounce scattering component, which is more than 1 dB. This rise makes sense, because the area at this survey point was watered between the first and second flight, thus inverting the moisture gradient when compared to the other points. For the survey points "B18" and "B22" the intensity drops between the first and second flight, because the surface and grass dry up. But at the survey point "A30" the surface and grass get wetter between the first and second flight due to the watering and therefore the intensity rises.

In Figure 4.1.6 the intensity of the Pauli composites of the survey point "B03" is shown. Also here a drop of the intensity from the first to the second flight is evident. The highest drop is for the volume scattering component, where it is around 1 dB.

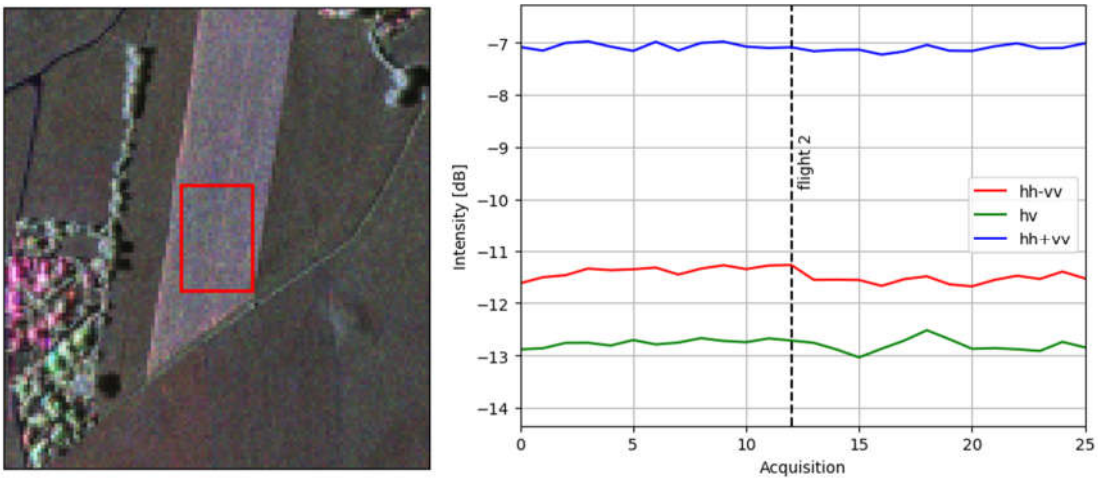

Figure 4.1.1: Left: Pauli composite image around the area of survey point "A16". The red rectangle shows the area which is used for all further evaluations of this survey point. Right: Intensity of Pauli composites averaged over area in red rectangle. (Red: Even bounce scattering, green: Volume scattering, blue: Odd bounce scattering).

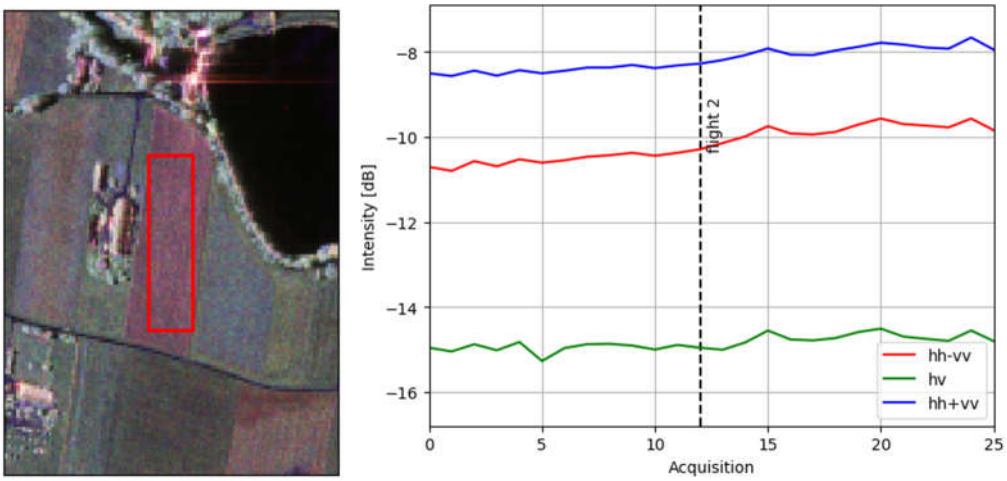

Figure 4.1.2: Left: Pauli composite image around the area of survey point "B01". The red rectangle shows the area which is used for all further evaluations of this survey point. Right: Intensity of Pauli composites averaged over area in red rectangle. (Red: Even bounce scattering, green: Volume scattering, blue: Odd bounce scattering).

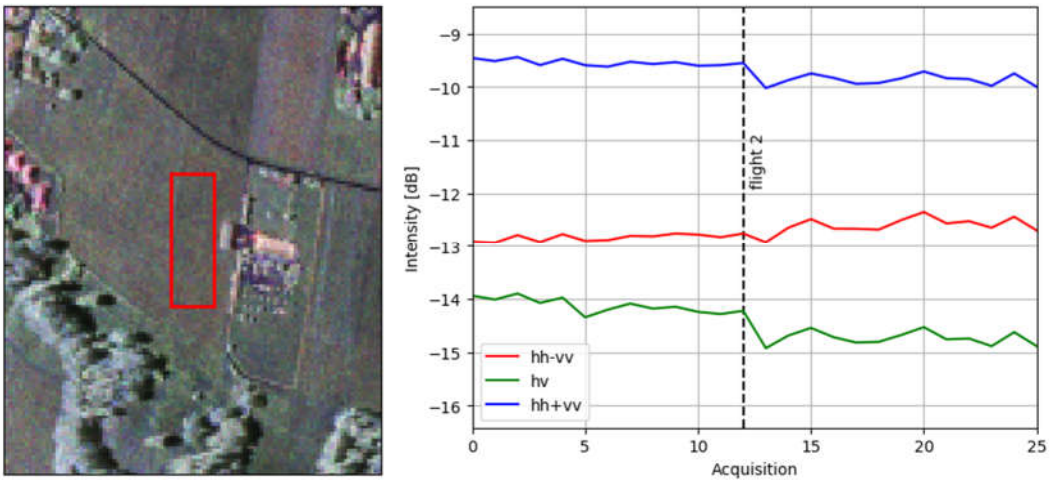

Figure 4.1.3: Left: Pauli composite image around the area of survey point "B18". The red rectangle shows the area which is used for all further evaluations of this survey point. Right: Intensity of Pauli composites averaged over area in red rectangle. (Red: Even bounce scattering, green: Volume scattering, blue: Odd bounce scattering).

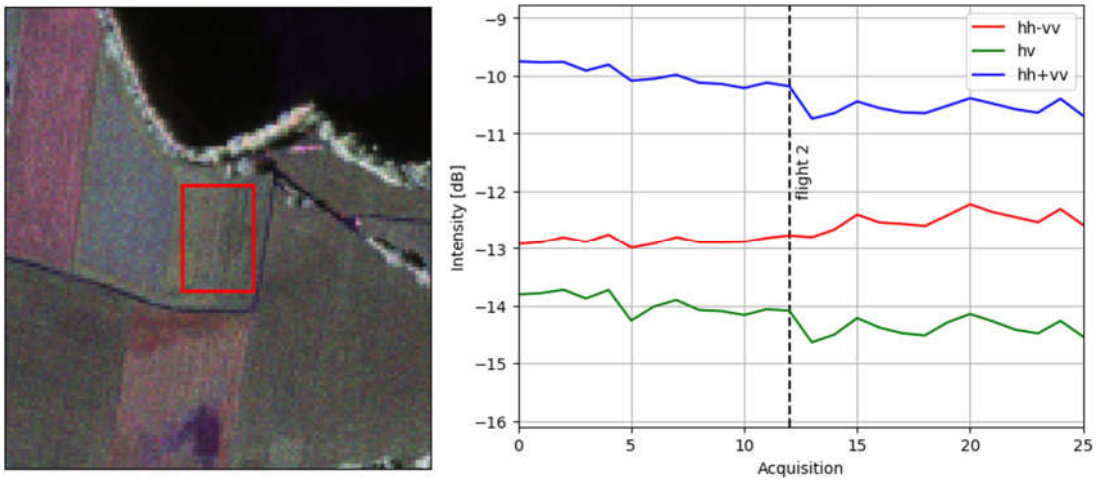

Figure 4.1.4: Left: Pauli composite image around the area of survey point "B22". The red rectangle shows the area which is used for all further evaluations of this survey point. Right: Intensity of Pauli composites averaged over area in red rectangle. (Red: Even bounce scattering, green: Volume scattering, blue: Odd bounce scattering).

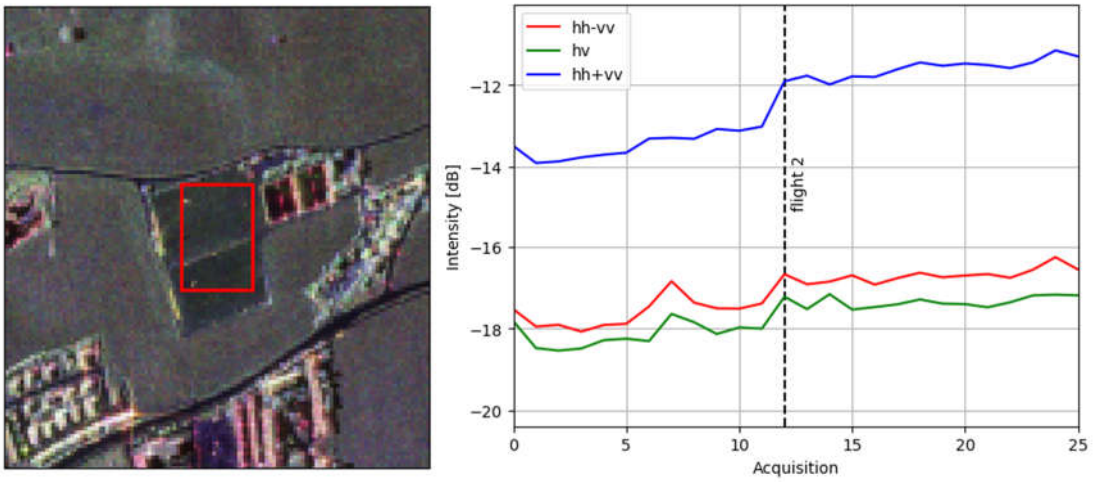

Figure 4.1.5: Left: Pauli composite image around the area of survey point "A30". The red rectangle shows the area which is used for all further evaluations of this survey point. Right: Intensity of Pauli composites averaged over area in red rectangle. (Red: Even bounce scattering, green: Volume scattering, blue: Odd bounce scattering).

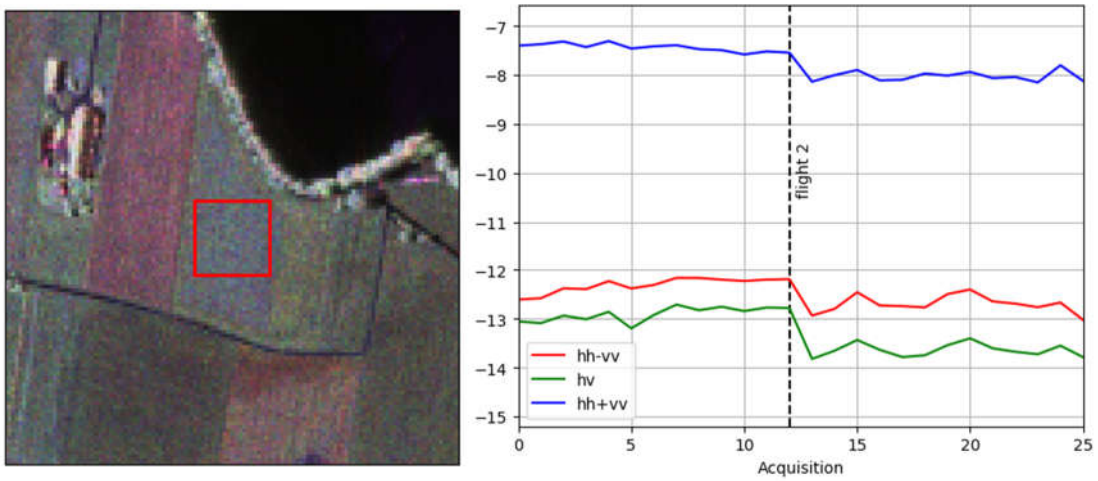

Figure 4.1.6: Left: Pauli composite image around the area of survey point "B03". The red rectangle shows the area which is used for all further evaluations of this survey point. Right: Intensity of Pauli composites averaged over area in red rectangle. (Red: Even bounce scattering, green: Volume scattering, blue: Odd bounce scattering).

4.2 Coherence Analysis at Survey Points

Figure 4.2.1 shows the coherence at the survey point "A16". Here the coherence is evaluated from the area which is marked by the red rectangle in Figure 4.1.1. In Figure 4.2.1 the coherence is evaluated for each acquisition with the first acquisition of each flight as master. The coherence is evaluated for the different Pauli composites.

Figure 4.2.2 displays the coherence over time for the survey point "A16". Here the coherence is evaluated in dependence of the UTC time and the master is always the first acquisition of the first flight. Also here the coherence is evaluated for the different Pauli composites.

The coherence is evaluated with the same approach as in Figure 4.2.1 also in Figures 4.2.3, 4.2.5, 4.2.7 and 4.2.9 but for the survey points "B01", "B18", "B22" and "A30". In Figures 4.2.1 and 4.2.3 some differences are visible between the coherences of the different Pauli composites. For the survey point "A16" the coherence of the odd bounce scattering is the lowest and for the survey point "B01"the coherence of the volume scattering is the lowest. For these two survey points there is no significant difference between the coherence of the first flight and the coherence of the second flight. The coherence of the survey point "A16" variates strongly in dependence of the different acquisitions for both flights. One explanation for this variation is volume decorrelation, because at "A16" corn with a height of 190 cm was growing. However, an analysis of the height of ambiguity showed only partial correlation between the variations of the height of ambiguity and the coherence of "A16". Therefore, also other effects must have influenced the coherence of "A16".

This is different for the coherences of survey points "B18" and "B22", which are displayed in Figures 4.2.5 and 4.2.7. Here a significant difference between the coherence of the first and second flight is evident. The coherence of the first flight is much lower than the one of the second flight. This is considered to be due to moisture, because it was reported by the ground truth measurement teams that the grass was wetter in the morning than in the afternoon. The difference between the first and the second flight cannot be due to temporal decorrelation, because the wind velocity was higher during the second flight (see [1]) and because especially around the area of survey point "B18" the grass was too short to decorrelate temporally due to wind. A difference in the coherence between the first and second flight is not present for the survey points "A16" and "B01", because for pronounced vegetation other factors are more dominant than moisture. In the areas around survey points "B18" and "B22" a phase triplets analysis shows a closure phase which is unequal to zero, which is another indication that a difference in moisture has to be considered between the two flights. The phase triplets analysis can be found in Chapter 8. The coherence at the survey points "B18" and "B22" is significantly higher than the one at the survey points "A16" and "B01". This is because high vegetation decorrelates stronger due to temporal decorrelation and due to volume decorrelation.

Figure 4.2.9 shows the coherence at the survey point "A30". Here the coherence of the first flight is higher until the 5th acquisition for the odd bounce scattering and the volume scattering and later on the coherences of both flights are similar. The coherences at survey point "A30" are much lower than one would expect for short grass in comparison to the coherences of "B18" and "B22". This is probably due to the watering of the field in between the two flights.

In Figures 4.2.4, 4.2.6, 4.2.8 and 4.2.10 the coherence over time is evaluated with the same approach as the one in Figure 4.2.2, but for the survey points "B01", "B18", "B22" and "A30". Figures 4.2.2 and 4.2.4 show the coherence over time for the survey points "A16" and "B01", where high vegetation was present. These figures show that the coherences vary a lot and the coherences also differ for different Pauli composites. There is a drop in coherence be-

tween the first and second flight, but this drop is not very pronounced. This is very different for the coherences over time for the survey points "B18" and "B22", which are visible in Figures 4.2.6 and 4.2.8. Here a significant drop in coherence is evident between the first and second flight. The survey points "B18" and "B22" differ from the survey points "A16" and "B01" because here only grass was present during the data acquisition with no crops. The coherences in Figures 4.2.6 and 4.2.8 are almost equal for the different Pauli composites, but during the second flight a slightly higher difference is visible. The coherences at the "B22" survey point are lower than the ones at the "B18" survey point, because the grass was higher. A drop in the coherence between the first and second flight is also visible at the survey point "A30" in Figure 4.2.10. Here the coherence varies stronger for the different Pauli composites.

Figure 4.2.11 shows the coherence of the survey point "B03". Here the coherence of the first and second flight is similar until the third acquisition, but after the third acquisition the coherence of the second flight is significantly higher than the one of the first flight. The coherence is overall very low, which is surprising, because only grass with 40 cm height was recorded at this survey point. One possibility is that this field was watered, like the one at survey point "A30". Another possibility is that this survey point was documented wrongly. Figure 4.2.12 shows the coherence over time for the survey point "B03". Here no significant drop occurs between the first and the second flight.

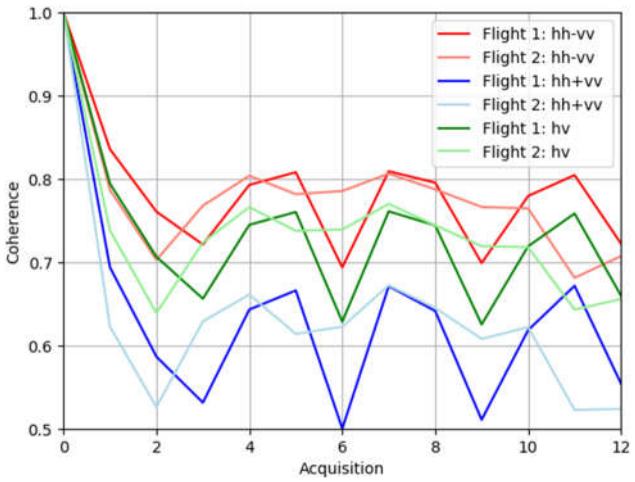

Figure 4.2.1: Coherence for survey point "A16" for all acquisitions with first acquisition of each flight as master for the different Pauli composites (Red: Even bounce scattering, green: Volume scattering, blue: Odd bounce scattering).

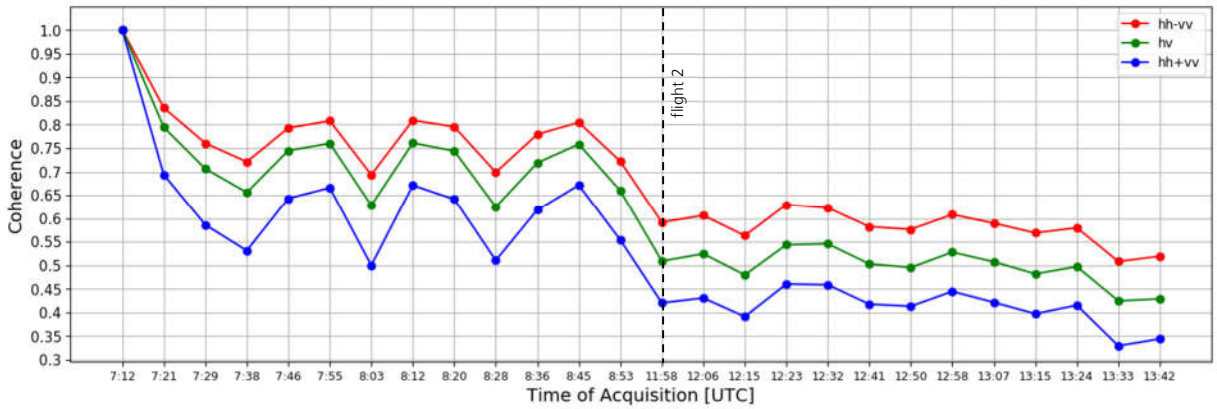

Figure 4.2.2: Coherence over time for survey point "A16" with first acquisition of first flight as master for the different Pauli composites (Red: Even bounce scattering, green: Volume scattering, blue: Odd bounce scattering).

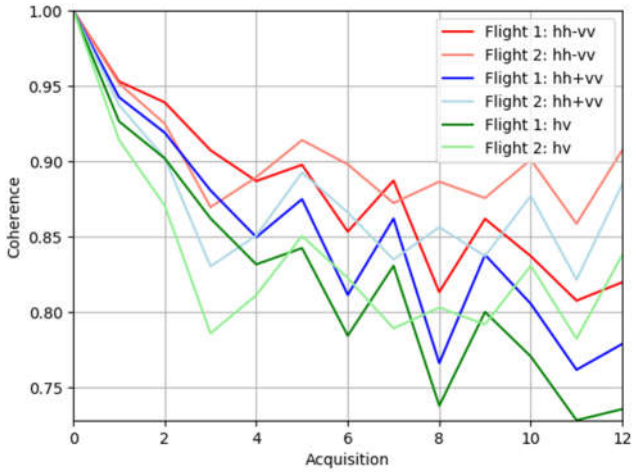

Figure 4.2.3: Coherence for survey point "B01" for all acquisitions with first acquisition of each flight as master for the different Pauli composites (Red: Even bounce scattering, green: Volume scattering, blue: Odd bounce scattering).

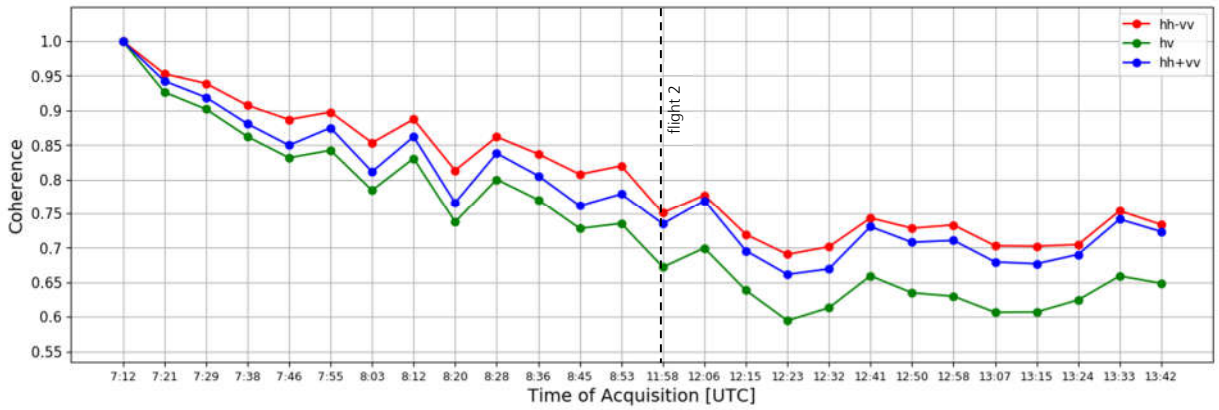

Figure 4.2.4: Coherence over time for survey point "B01" with first acquisition of first flight as master for the different Pauli composites (Red: Even bounce scattering, green: Volume scattering, blue: Odd bounce scattering).

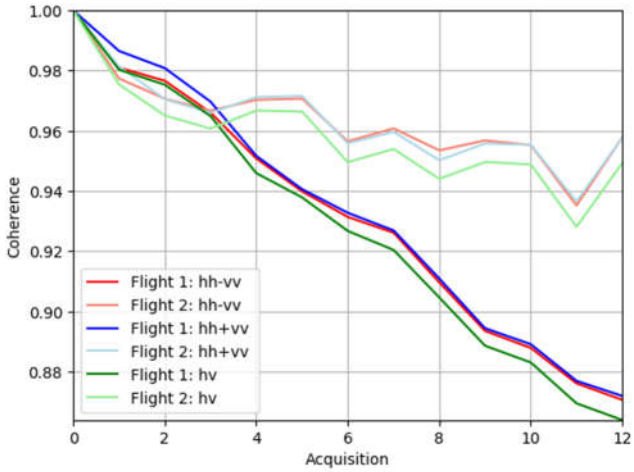

Figure 4.2.5: Coherence for survey point "B18" for all acquisitions with first acquisition of each flight as master for the different Pauli composites (Red: Even bounce scattering, green: Volume scattering, blue: Odd bounce scattering).

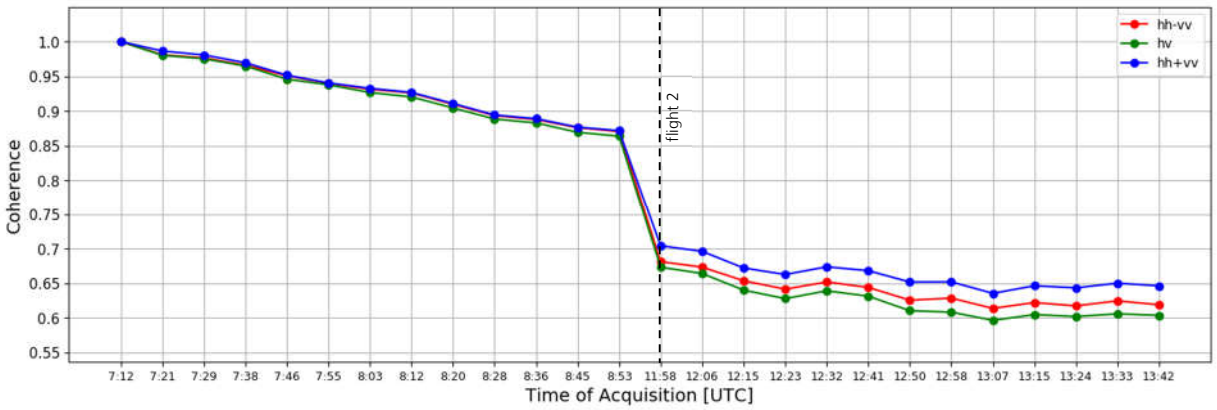

Figure 4.2.6: Coherence over time for survey point "B18" with first acquisition of first flight as master for the different Pauli composites (Red: Even bounce scattering, green: Volume scattering, blue: Odd bounce scattering).

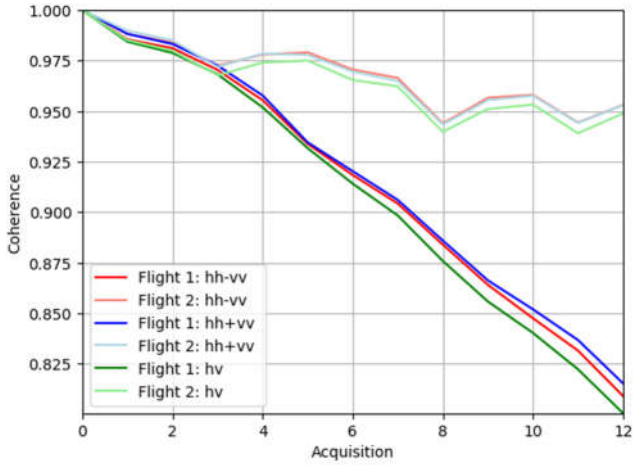

Figure 4.2.7: Coherence for survey point "B22" for all acquisitions with first acquisition of each flight as master for the different Pauli composites (Red: Even bounce scattering, green: Volume scattering, blue: Odd bounce scattering).

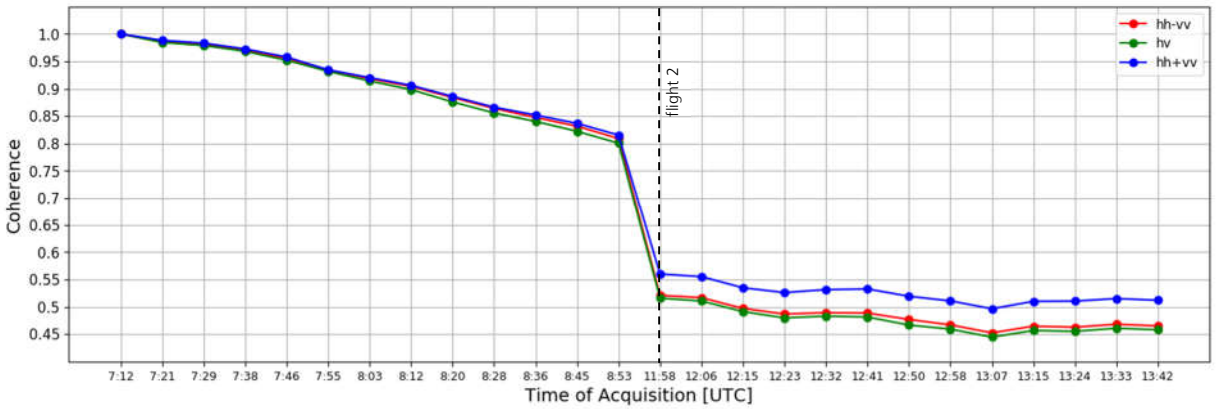

Figure 4.2.8: Coherence over time for survey point "B22" with first acquisition of first flight as master for the different Pauli composites (Red: Even bounce scattering, green: Volume scattering, blue: Odd bounce scattering).

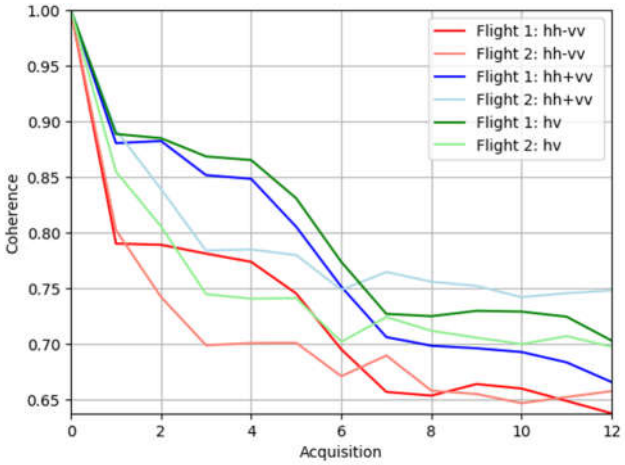

Figure 4.2.9: Coherence for survey point "A30" for all acquisitions with first acquisition of each flight as master for the different Pauli composites (Red: Even bounce scattering, green: Volume scattering, blue: Odd bounce scattering).

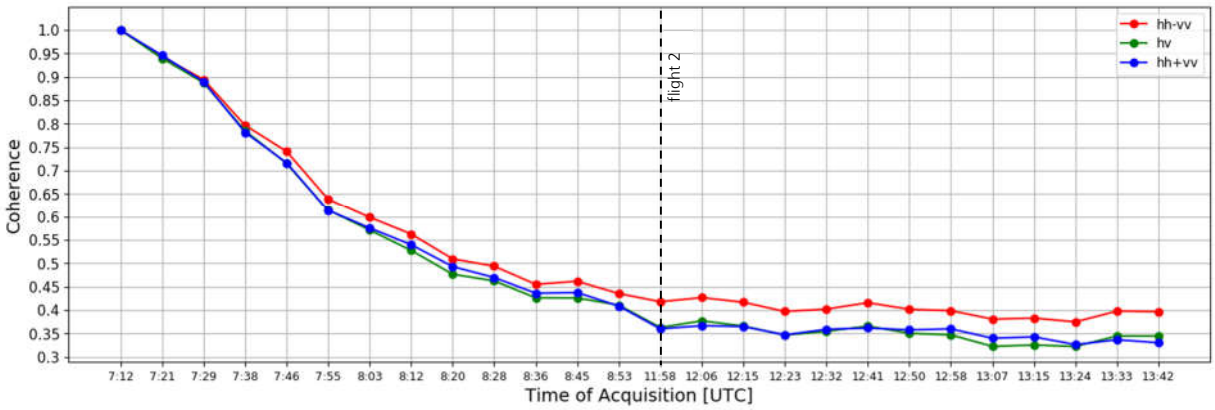

Figure 4.2.10: Coherence over time for survey point "A30" with first acquisition of first flight as master for the different Pauli composites (Red: Even bounce scattering, green: Volume scattering, blue: Odd bounce scattering).

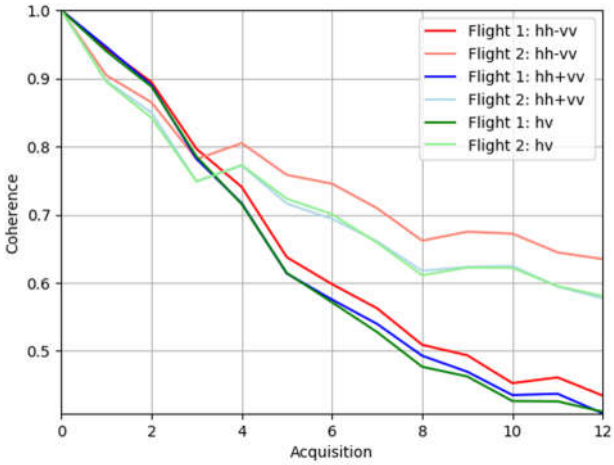

Figure 4.2.11: Coherence for survey point "B03" for all acquisitions with first acquisition of each flight as master for the different Pauli composites (Red: Even bounce scattering, green: Volume scattering, blue: Odd bounce scattering).

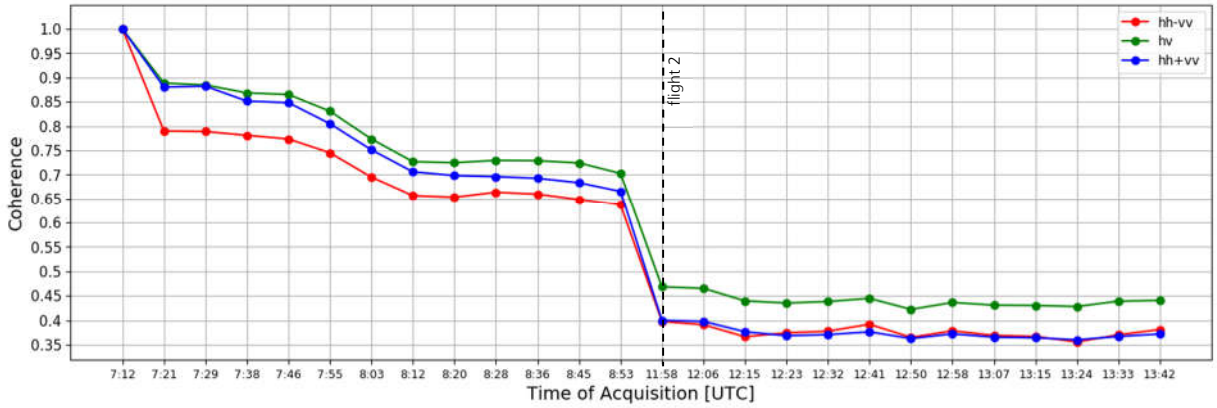

Figure 4.2.12: Coherence over time for survey point "B03" with first acquisition of first flight as master for the different Pauli composites (Red: Even bounce scattering, green: Volume scattering, blue: Odd bounce scattering).

4.3 Interferometric Phase Analysis at Survey Points

Figures 4.3.1 - 4.3.6 show on the right side the interferometric phase for the different survey points averaged over the areas which are marked by the red rectangles in Figures 4.1.1 - 4.1.6. The interferometric phase is evaluated for each acquisition and for the different Pauli composites with the first acquisition of the first flight as master. The black dotted line in the middle of the image indicates when the acquisitions correspond to the second flight. The right side of Figures 4.3.1 - 4.3.6 shows the height of ambiguity calculated from the spatial baseline also of the areas which are marked by the red rectangles in Figures 4.1.1 - 4.1.6. The spatial baseline is in reference to the first acquisition of the first flight. Ideally, the spatial baseline should be zero making the height of ambiguity infinitely large. However, Figures 4.3.1 - 4.3.6 show that for some acquisitions a change in the interferometric phase due to the height of ambiguity has to be considered.

All interferograms have been calibrated using a corner reflector in the image in order to align the interferometric phases. However, one can still observe a quasi-random behaviour of the interferometric phases, as well as the lack of correlation with the height of ambiguity, i.e., one would expect a small phase contribution in the presence of small interferometric baselines (i.e., large heights of ambiguity). The main reason for the disagreement is the fact that other effects are present in the interferograms, namely, residual topographic errors, residual motion errors and tropospheric errors. The topographic errors can be however assumed to be almost negligible, since a DEM was used to remove the topographic component. Residual motion errors occur due to the limited accuracy of the navigation system, which is in the order of 1 cm – 2 cm for F-SAR. Advanced calibration techniques have been applied within the operational processing chain in order to estimate and remove them, but small variations (~1 mm) cannot be discarded, which have a correlation length of a few hundred meters. Finally, a tropospheric signal is also present, since the F-SAR platform flies over the atmospheric boundary layer (ABL), which usually covers the first kilometre in elevation. The ABL represents the turbulent component of the low troposphere sensed by the SAR instrument, which can introduce phase fluctuations of 1 cm with correlation lengths of about 1 km. Concluding, a time-series analysis similar as conducted in the spaceborne case (i.e., persistent scatterer interferometry processing) would be necessary in order to filter out the aforementioned effects and retrieve the phase history related to the physical changes of the scatterers. Such an analysis is considered out of scope in this study. On the other hand, given the short time interval of less than one day, no phase changes are expected to be observed in the scene other than those related to moisture changes. In that case, a phase triplet analysis is more appropriate, since this kind of analysis automatically cancels out the deterministic signals mentioned before (residual topography, residual motion errors, tropospheric signal). The phase triplets analysis can be found in Chapter 8.

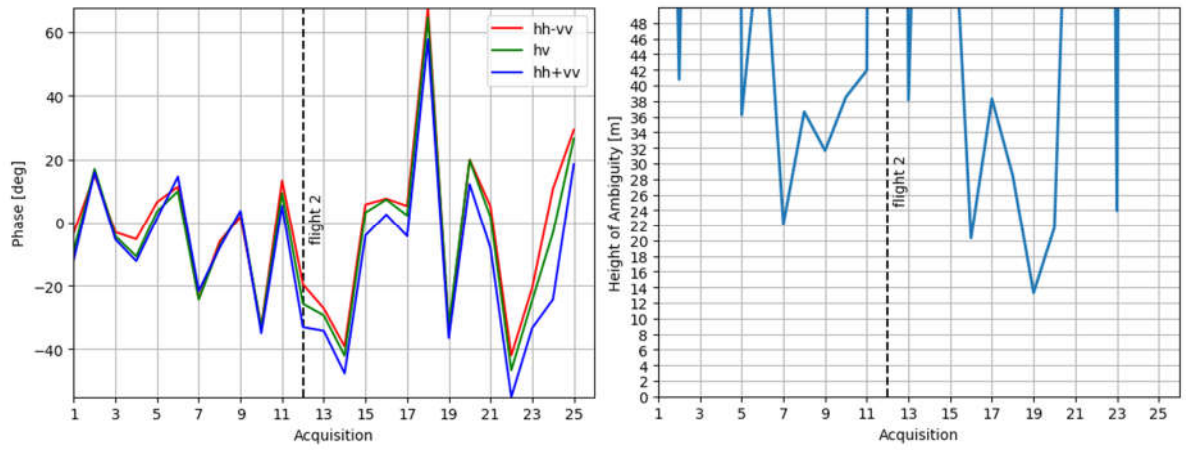

Figure 4.3.1: Left: Interferometric phase for survey point "A16" with first acquisition of first flight as master for the different Pauli composites (Red: Even bounce scattering, green: Volume scattering, blue: Odd bounce scattering). Right: Height of ambiguity for area around survey point "A16".

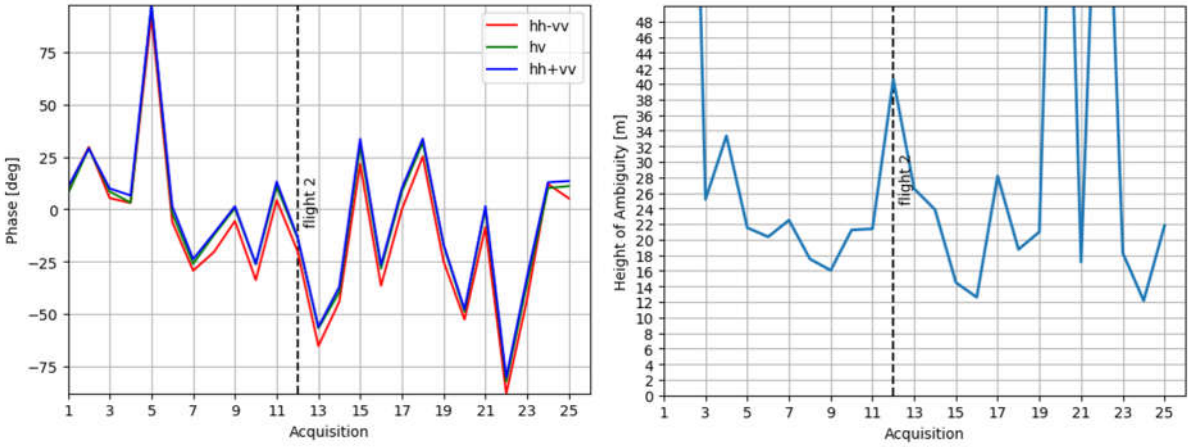

Figure 4.3.2: Left: Interferometric phase for survey point "B01" with first acquisition of first flight as master for the different Pauli composites (Red: Even bounce scattering, green: Volume scattering, blue: Odd bounce scattering). Right: Height of ambiguity for area around survey point "B01".

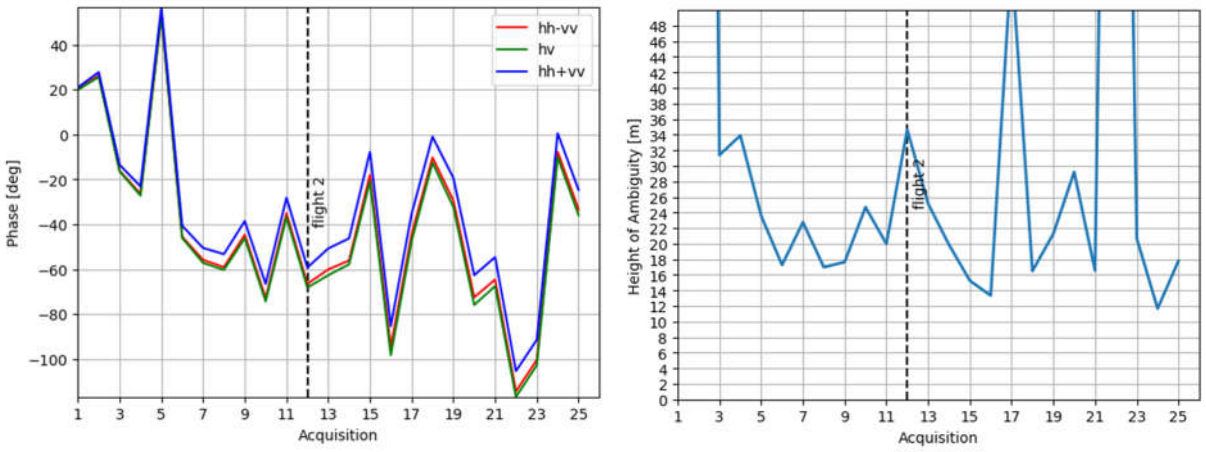

Figure 4.3.3: Left: Interferometric phase for survey point "B18" with first acquisition of first flight as master for the different Pauli composites (Red: Even bounce scattering, green: Volume scattering, blue: Odd bounce scattering). Right: Height of ambiguity for area around survey point "B18".

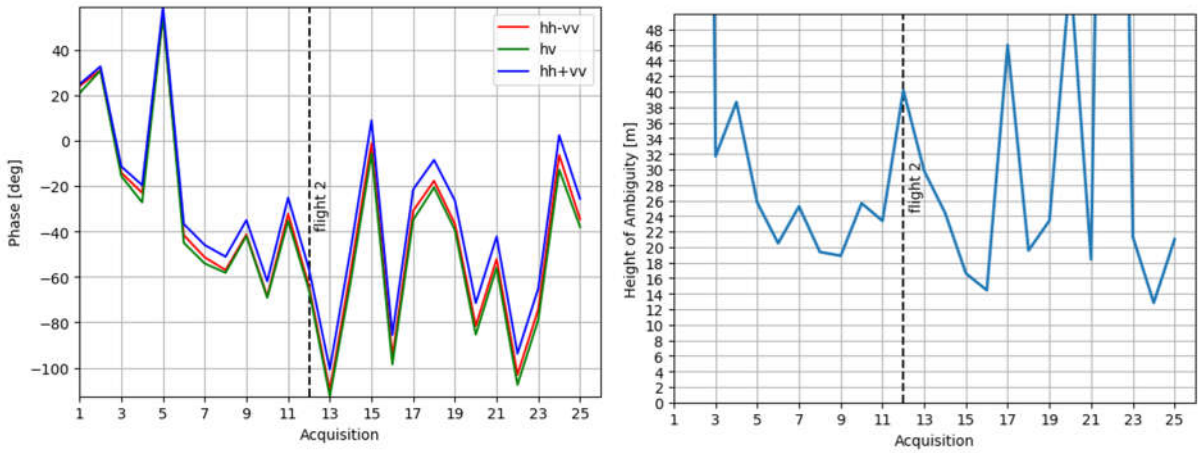

Figure 4.3.4: Left: Interferometric phase for survey point "B22" with first acquisition of first flight as master for the different Pauli composites (Red: Even bounce scattering, green: Volume scattering, blue: Odd bounce scattering). Right: Height of ambiguity for area around survey point "B22".

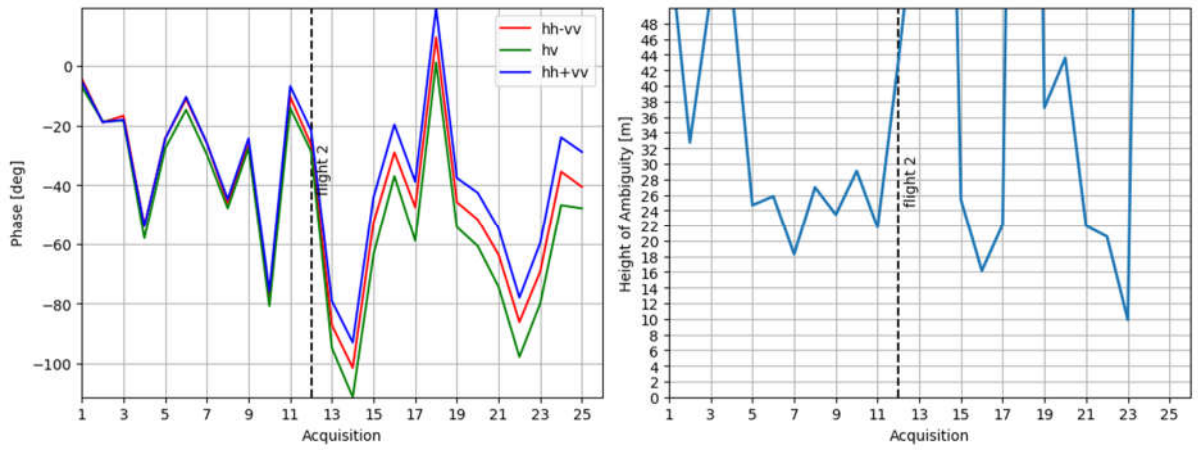

Figure 4.3.5: Left: Interferometric phase for survey point "A30" with first acquisition of first flight as master for the different Pauli composites (Red: Even bounce scattering, green: Volume scattering, blue: Odd bounce scattering). Right: Height of ambiguity for area around survey point "A30".

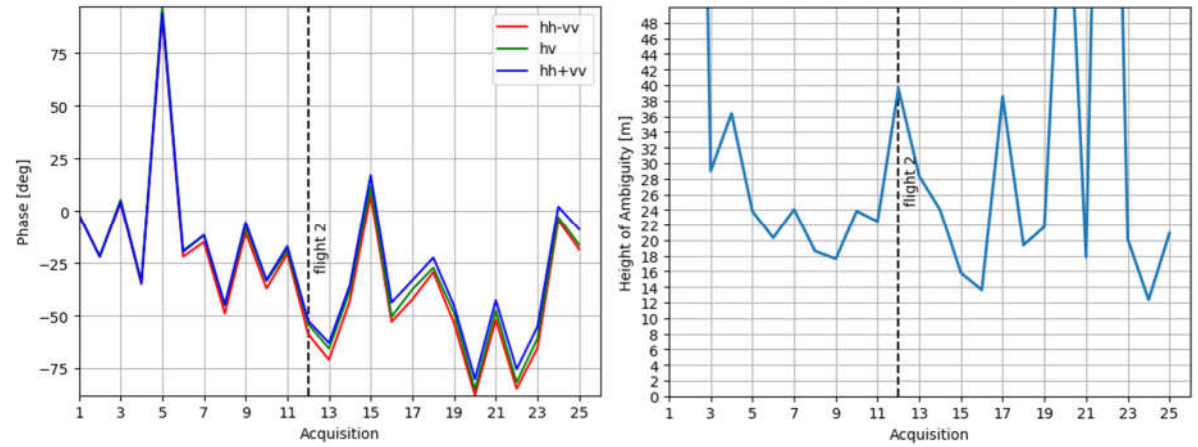

Figure 4.3.6: Left: Interferometric phase for survey point "B03" with first acquisition of first flight as master for the different Pauli composites (Red: Even bounce scattering, green: Volume scattering, blue: Odd bounce scattering). Right: Height of ambiguity for area around survey point "B03".

5 Survey Points Analysis for Time Series with Hydroterra Radar Parameters and Simulated Hydroterra Products

In this chapter the same analysis is performed as in Chapter 4, but for time series with Hydroterra parameters, which were described in Chapter 3. In Chapter 5.2 the coherences of the time series with Hydroterra parameters are also compared to the ones of simulated Hydroterra products.

The main purpose of this chapter is to analyse whether the properties of the different survey points change for Hydroterra parameters as compared to F-SAR parameters. One difference between the times series with Hydroterra parameters and the time series with F-SAR parameters is the different sampling size. Due to the lower resolution of the Hydroterra time series, fewer samples are available to estimate the different parameters of the fields at the survey points. The sampling size in azimuth is reduced by a factor of 14 and the sampling size in range is reduced by a factor of 64. Another difference between the time series with Hydroterra parameters and the time series with F-SAR parameters is the different NESZ. The F-SAR system has a significantly lower (better) NESZ, therefore thermal decorrelation does not have to be considered. This is however different for Hydroterra time series.

5.1 Survey Points Analysis of Time Series with Hydroterra Radar Parameters

In this section the intensity, coherence and interferometric phase of times series with Hydroterra radar parameters are analysed and compared to the ones of F-SAR.

In Figures 5.1.1 – 5.1.3 the intensities of Pauli composites of the time series with Hydroterra parameters of both flights are shown. The intensities vary more for each acquisition than the ones of the time series with F-SAR parameters which are shown in Figures 4.1.1 – 4.1.6. This is due to the smaller amount of samples which are available to estimate the intensities of each field. In azimuth the amount of samples is reduced by the factor of 14 and in range by a factor of 64 for Hydroterra data. The vegetation scattering component is always higher in Figures 5.1.1 – 5.1.3 than in Figures 4.1.1 – 4.1.6. This is because the intensity of the volume scattering component is very low and for Hydroterra noise already contributes at this intensity level. For the survey point "A30" in Figure 5.1.3 this is especially evident for the volume and the even bounce scattering components.

An increased intensity from the first to the second flight cannot be seen for the survey point "A30" for the Hydroterra time series, as opposed to the F-SAR time series shown in Figure 4.1.5. Figure 5.1.2 shows a drop of the intensity for the survey points "B18" and "B22" between the first and second flight for the Hydroterra time series, as this is also the case in Figures 4.1.3 and 4.1.4 for the F-SAR time series. However, because the intensities have larger variations, these drops are less pronounced. Figure 5.1.3 shows that for the survey point "B03" a drop in the intensity can only be observed for the volume scattering and the even bounce scattering component.

Figures 5.1.4 – 5.1.6 show the coherences for all acquisitions and the Pauli composites of the Hydroterra time series. Here the first acquisition of each flight is chosen as master. The coherences vary more and have lower values than the ones of F-SAR time series. The stronger variations are, again, due to the smaller amount of samples available for averaging. The lower coherence is due to the higher thermal decorrelation which has to be considered for Hydroterra data. In Figure 5.1.5 a pronounced difference between the coherences of the first and second flight is only visible for the odd and even bounce scattering components for the survey point "B18" and for the odd scattering component for the survey point "B22". The coherence of the volume scattering component is dominated by the thermal decorrelation, because the signal of the HV polarisation is much lower than the signals of other polarisations. The coherence of the survey point "B03", which is demonstrated on the right side of Figure 5.1.6, is significantly different between the first and second flight for the volume and odd bounce scattering component. A difference between the two flights for the even bounce scattering component is not visible

The coherence over time of Hydroterra time series is evaluated in Figures 5.1.7 – 5.1.12 for the different survey points and for different Pauli mechanisms with the first acquisition of the first flight as master. Like in Figures 5.1.4 – 5.1.6, these figures also show a higher variation of the coherence due to the smaller amount of samples available for averaging and lower values of the coherence due to higher thermal decorrelation as compared to F-SAR coherences. For the survey points "B18" and "B22" the coherence of the volume scattering component is much lower than the coherences of other components as shown in Figures 5.1.9 and 5.1.10 due to the lower signal-to-noise ratio of the HV polarisation. A drop in the coherence between the first and second flight is visible for the survey points "B18", "B22" and "A30" as this is also the case for F-SAR data. However, due to the higher thermal decorrelation and the higher variation of the coherences this drop is less pronounced.

In Figures 5.1.13 – 5.1.15 the interferometric phase is visualized for the different survey points. Here the first acquisition of the first flight is used as master and the phase is computed for different Pauli composites. The interferometric phases for time series with Hydroterra radar parameters are very similar to the ones of F-SAR radar parameters. For the survey points "A16" and "A30" the variations are higher due to a higher noise level and smaler amount of available samples for averaging.

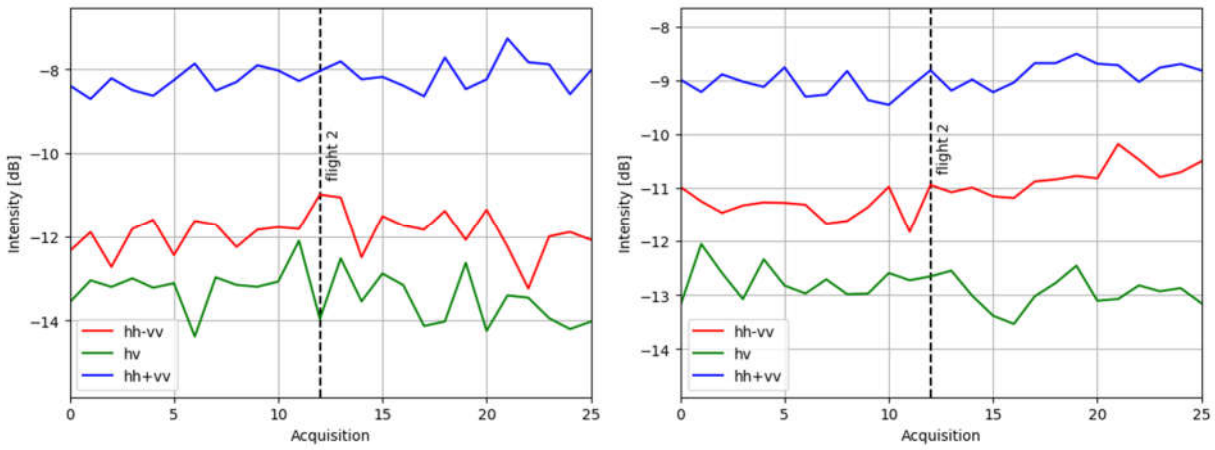

Figure 5.1.1: Intensity of Pauli composites for Hydroterra parameters. Left: For survey point "A16", right: For survey point "B01".

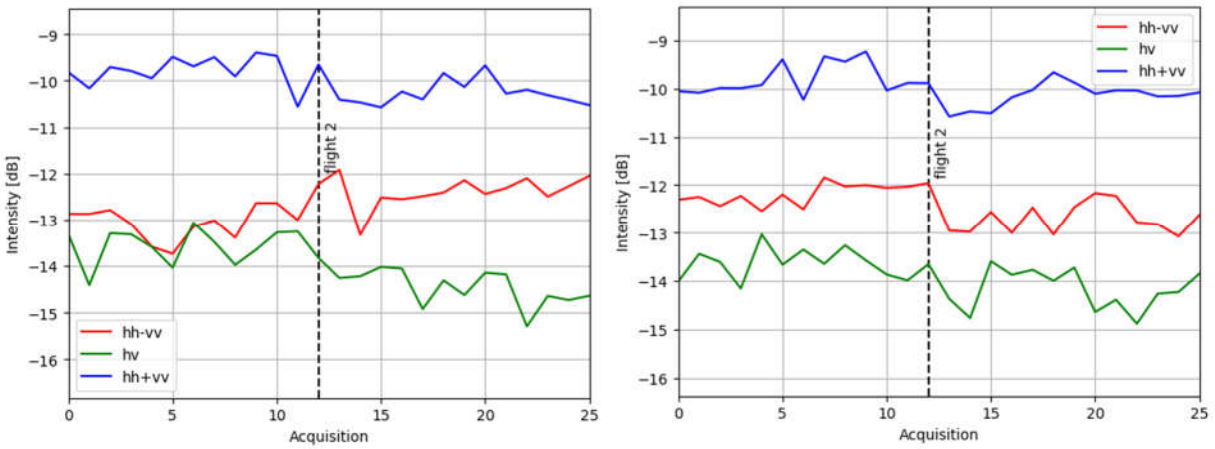

Figure 5.1.2: Intensity of Pauli composites for Hydroterra parameters. Left: For survey point "B18", right: For survey point "B22".

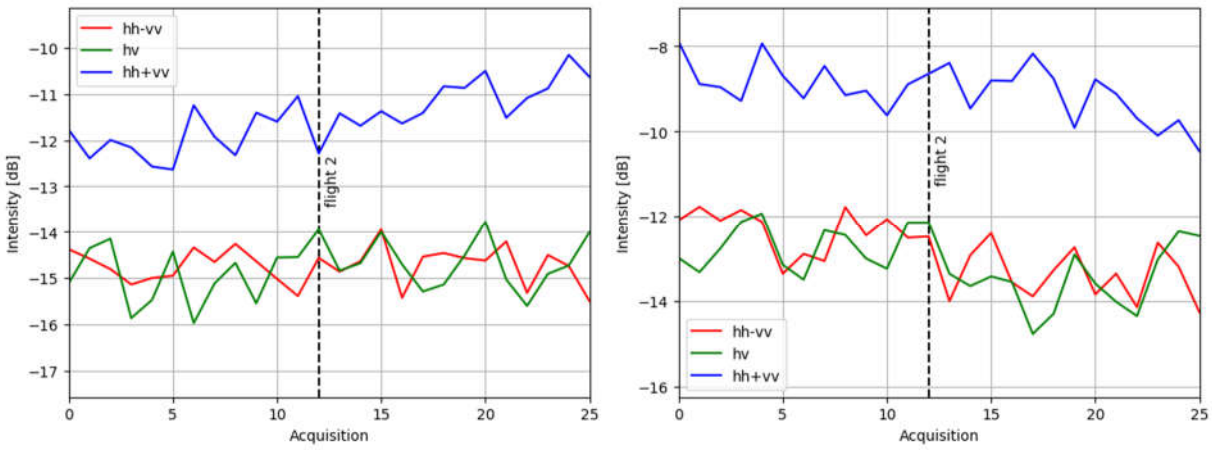

Figure 5.1.3: Intensity of Pauli composites for Hydroterra parameters. Left: For survey point "A30", right: For survey point "B03".

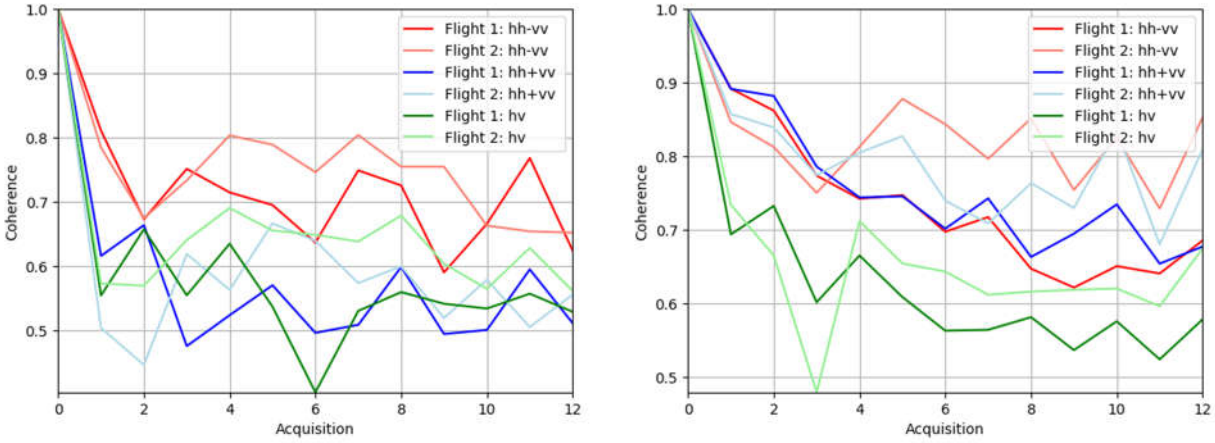

Figure 5.1.4: Coherence for Hydroterra parameters for all acquisitions with first acquisition of each flight as master for the different Pauli composites. Left: For survey point "A16", right: For survey point "B01".

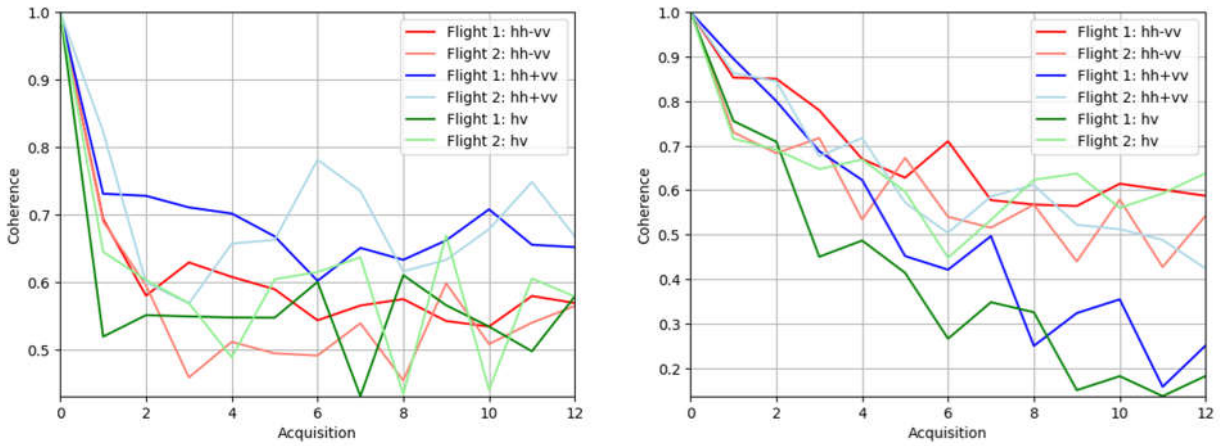

Figure 5.1.5: Coherence for Hydroterra parameters for all acquisitions with first acquisition of each flight as master for the different Pauli composites. Left: For survey point "B18", right: For survey point "B22".

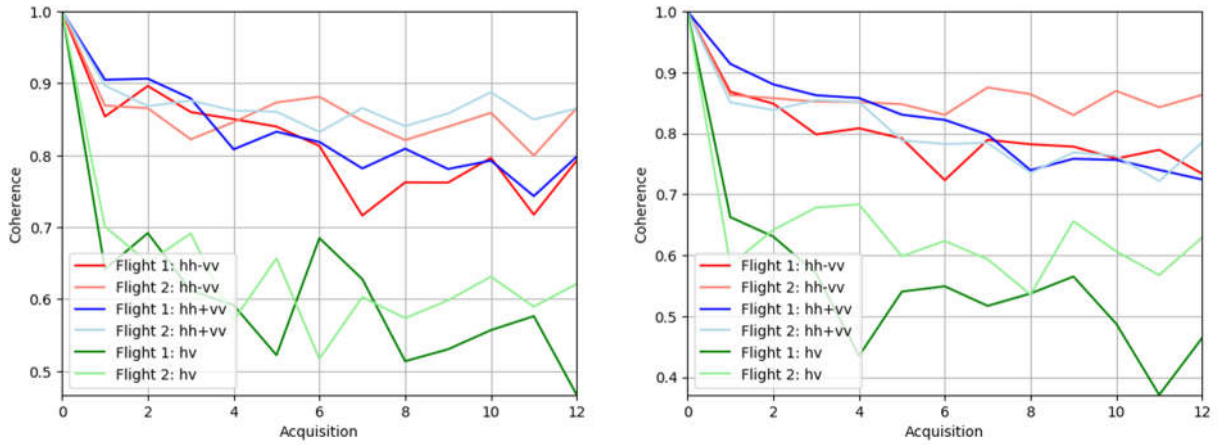

Figure 5.1.6: Coherence for Hydroterra parameters for all acquisitions with first acquisition of each flight as master for the different Pauli composites. Left: For survey point "A30", right: For survey point "B03".

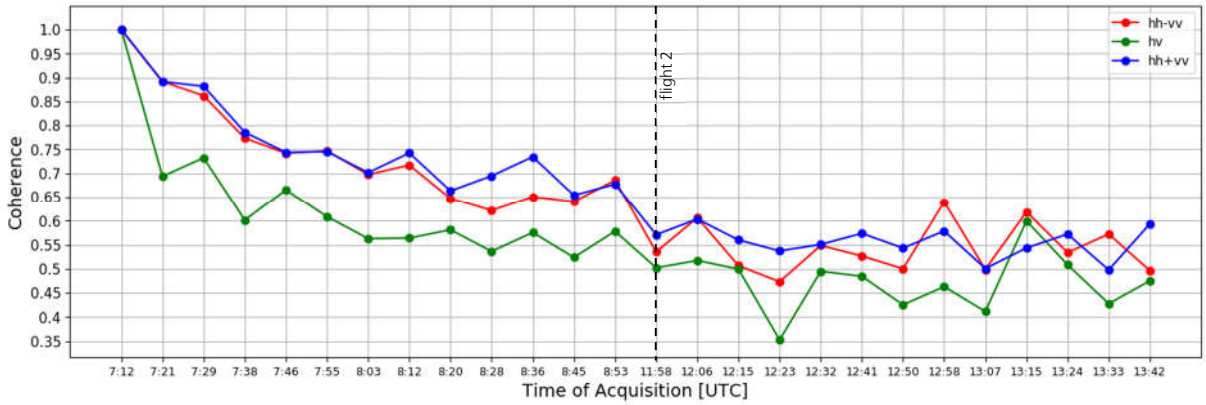

Figure 5.1.7: Coherence over time for Hydroterra parameters and survey point "A16" with first acquisition of first flight as master for the different Pauli composites.

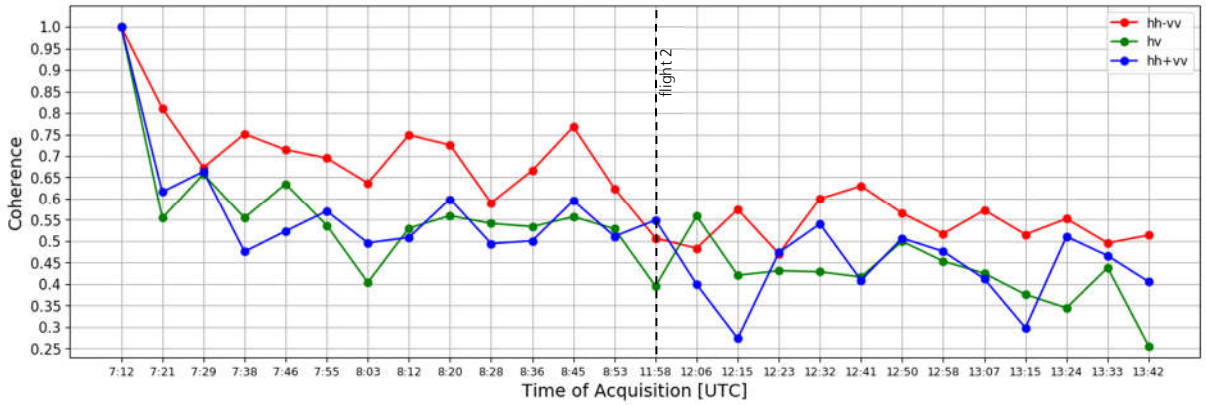

Figure 5.1.8: Coherence over time for Hydroterra parameters and survey point "B01" with first acquisition of first flight as master for the different Pauli composites.

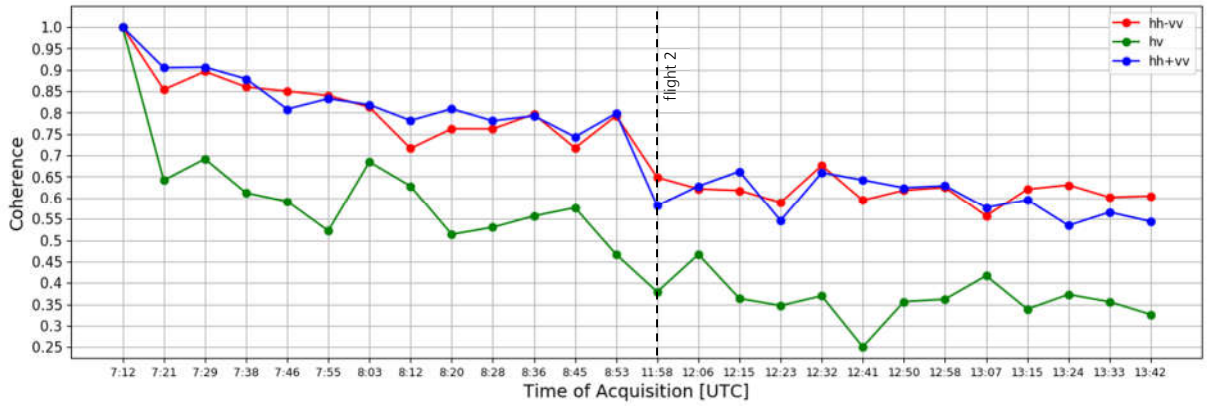

Figure 5.1.9: Coherence over time for Hydroterra parameters and survey point "B18" with first acquisition of first flight as master for the different Pauli composites.

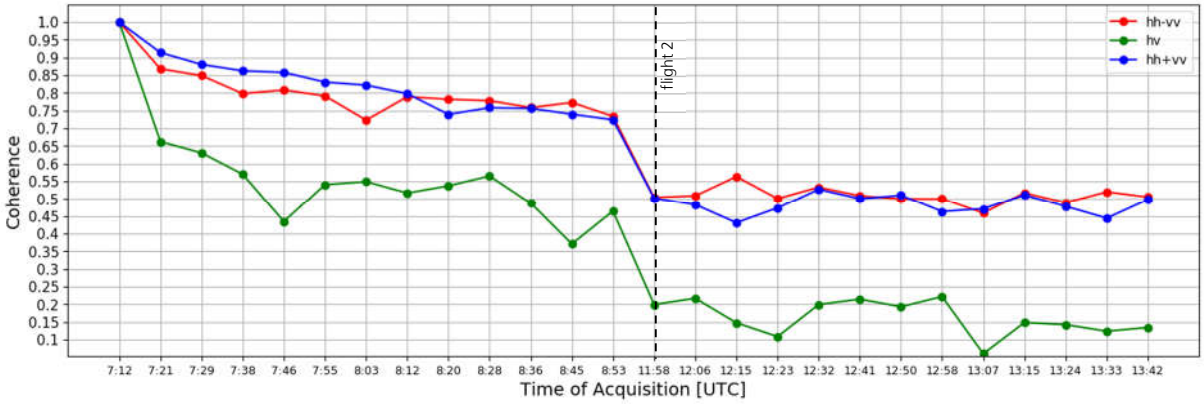

Figure 5.1.10: Coherence over time for Hydroterra parameters and survey point "B22" with first acquisition of first flight as master for the different Pauli composites.

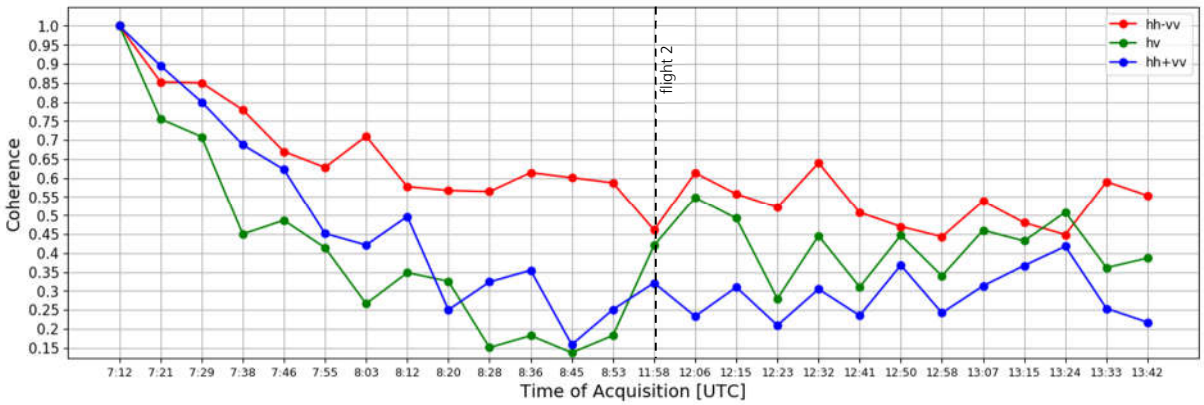

Figure 5.1.11: Coherence over time for Hydroterra parameters and survey point "A30" with first acquisition of first flight as master for the different Pauli composites.

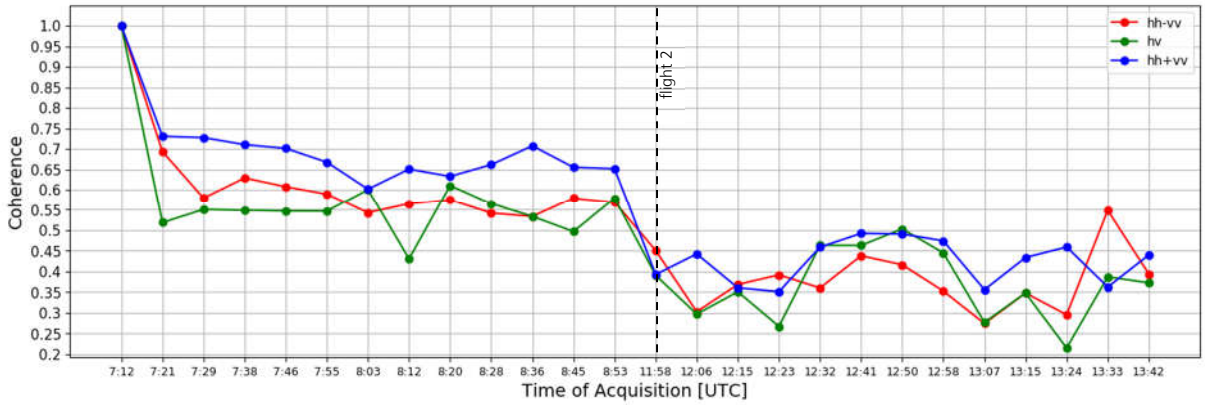

Figure 5.1.12: Coherence over time for Hydroterra parameters and survey point "B03" with first acquisition of first flight as master for the different Pauli composites.

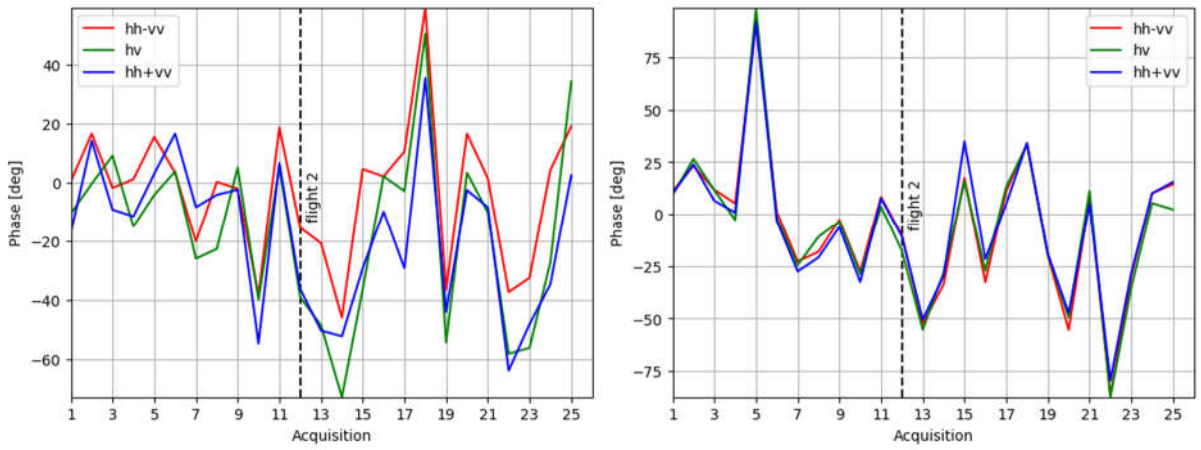

Figure 5.1.13: Interferometric phase for Hydroterra parameters with first acquisition of first flight as master for the different Pauli composites. Left: For survey point "A16", right: For survey point "B01".

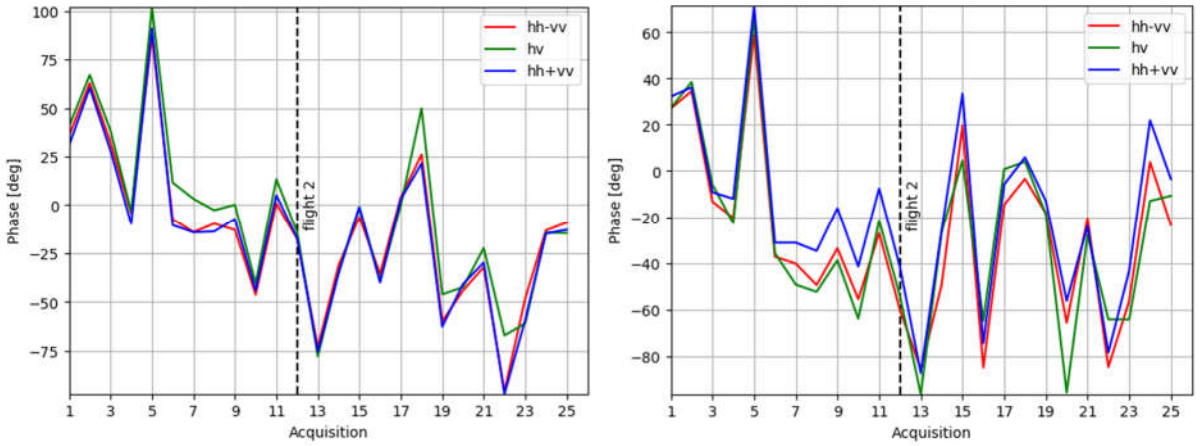

Figure 5.1.14: Interferometric phase for Hydroterra parameters with first acquisition of first flight as master for the different Pauli composites. Left: For survey point "B18", right: For survey point "B22".

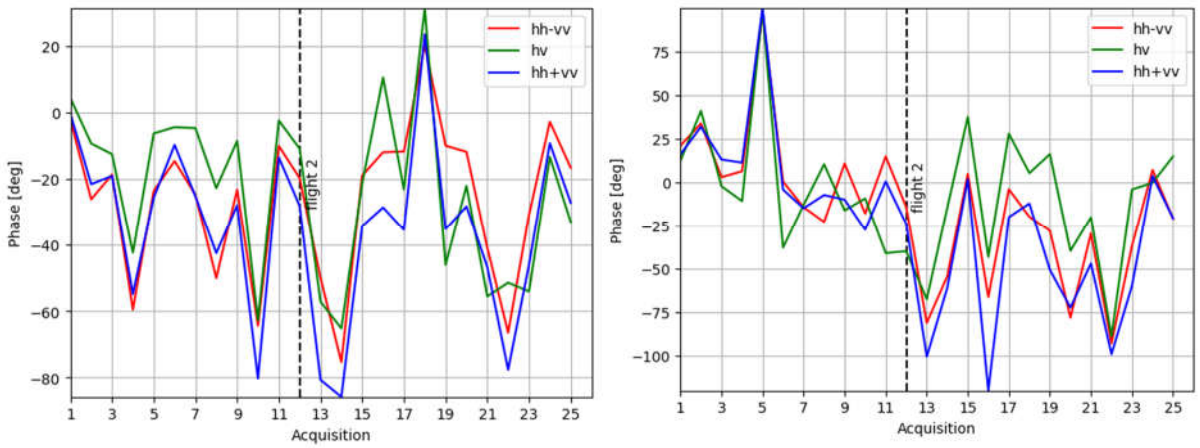

Figure 5.1.15: Interferometric phase for Hydroterra parameters with first acquisition of first flight as master for the different Pauli composites. Left: For survey point "A30", right: For survey point "B03".

5.2 Coherence Analysis of Simulated Hydroterra Products

In this section the coherence of the simulated Hydroterra products, which is described in Chapter 3.3, is compared to the one of the time series with Hydroterra radar parameters. The coherence of the simulated Hydroterra product is compared to the mean coherence of the Hydroterra time series. To compute the mean coherence, coherences with all acquisitions of the first flight as master and all acquisitions of the second flight as slave were estimated and the mean of these coherences were calculated. This comparison is summarized in Tables 5.2.1 – 5.2.3. Here the described mean coherence and Hydroterra coherence are compared to each other for each survey point and the different polarisations. The difference refers to Hydroterra coherence minus mean coherence. The comparison in Tables 5.2.1 – 5.2.3 shows that the two different coherences agree quite well.

Survey Point	Mean Coherence	Hydroterra Coherence	Difference
"A16"	0.518	0.559	0.041
"B01"	0.677	0.621	-0.057
"B18"	0.716	0.685	-0.031
"B22"	0.523	0.505	-0.018
"A30"	0.450	0.445	-0.005
"B03"	0.335	0.314	-0.021

Table 5.2.1: Comparison between mean and Hydroterra coherence for the HH polarisation. The mean coherence is computed from all coherences between flight 1 and flight 2. The Hydroterra coherence is calculated from the simulated Hydroterra products of flight 1 and flight 2.

Survey Point	Mean Coherence	Hydroterra Coherence	Difference
"A16"	0.444	0.519	0.074
"B01"	0.519	0.446	-0.073
"B18"	0.443	0.456	0.013
"B22"	0.307	0.301	-0.006
"A30"	0.383	0.443	0.060
"B03"	0.315	0.394	0.079

Table 5.2.2: Comparison between mean and Hydroterra coherence for the HV polarisation. The mean coherence is computed from all coherences between flight 1 and flight 2. The Hydroterra coherence is calculated from the simulated Hydroterra products of flight 1 and flight 2.

Survey Point	Mean Coherence	Hydroterra Coherence	Difference
"A16"	0.395	0.461	0.065
"B01"	0.587	0.609	0.022
"B18"	0.649	0.668	0.019
"B22"	0.520	0.566	0.046
"A30"	0.441	0.518	0.077
"B03"	0.183	0.197	0.014

Table 5.2.3: Comparison between mean and Hydroterra coherence for the VV polarisation. The mean coherence is computed from all coherences between flight 1 and flight 2. The Hydroterra coherence is calculated from the simulated Hydroterra products of flight 1 and flight 2.

6 Coherence for Urban and Forest Areas

In this chapter the coherence of three forested areas and three urban areas is evaluated for a times series with F-SAR radar parameters and a time series with Hydroterra parameters. These coherences are also compared to the coherences of the field areas of different survey points from Chapter 4 and to the coherence between the two simulated Hydroterra products.

Figure 6.1 shows the positions of the three forested areas and urban areas which will be analysed in this chapter in a Pauli composite image and Figures 6.2 and 6.3 provide a closer look of these areas. In Figures 6.2 and 6.3 the red rectangle indicates the areas where the coherence is evaluated.

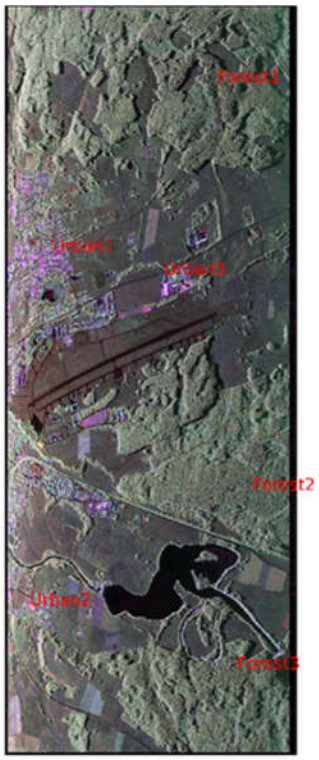

Figure 6.1: All forest and urban areas which will be further analysed in this chapter in Pauli composite image. (Red: Even bounce scattering, green: Volume scattering, blue: Odd bounce scattering).

Figure 6.2: Pauli composite images around forest areas which are further analysed. The red rectangle shows the areas which are used for all further evaluations. Left: "Forest 1" (area: 99 m x 90 m), middle: "Forest 2" (area: 132 m x 120 m), right: "Forest 3" (area: 165 m x 150 m).

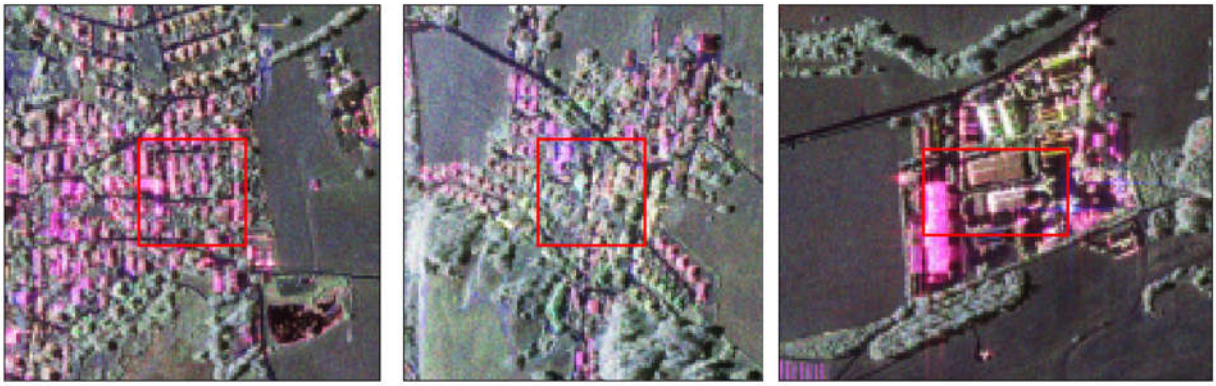

Figure 6.3: Pauli composite images around urban areas which are further analysed. The red rectangle shows the areas which are used for all further evaluations. Left: "Urban 1" (area: 132 m x 120 m), middle: "Urban 2" (area: 132 m x 120 m), right: "Urban 3" (area: 132 m x 210 m).

6.1 Coherence of Time Series with F-SAR Radar Parameters

In this section the coherences of three forested areas and three urban areas of time series with F-SAR radar parameters are evaluated and analysed.

On the left side of Figures 6.1.1 – 6.1.3 the coherence of the different forest areas is shown for the F-SAR radar parameters and different Pauli composites. Here the first acquisition of each flight is used as master and the coherence is calculated for each acquisition. On the right side of Figures 6.1.1 – 6.1.3 the height of ambiguity of the same areas is calculated. The coherence in Figures 6.1.1 – 6.1.3 shows that already for the second acquisition the coherence drops significantly. As one would expect, the coherence of forest areas is much lower than the one of field areas, which were shown in Chapter 4, due to temporal decorrelation. No significant difference is visible between the coherence of flight 1 and the one of flight 2. Some correlation is evident between the height of ambiguity on the right side of Figures 6.1.1 – 6.1.3 and the coherence. This is especially evident in Figure 6.1.3, where the coherences drop for the same acquisitions as the height of ambiguity drops due to volume decorrelation.

Figures 6.1.4 – 6.1.6 show the coherence over time for the three forested areas. Here the coherence is evaluated from the time series with F-SAR radar parameters for the different Pauli composites with the first acquisition of the first flight as master. These figures show that there is no drop in coherence between the first and second flight. The highest drop in coherence occurs for the second acquisition of the first flight. The coherence of the odd bounce scattering is always slightly higher for the forest areas, presumably due to the better temporal stability of the double bounce component given by the ground – trunk interaction.

The coherence of urban areas is visible on the left side of Figures 6.1.7 – 6.1.9. Here also the time series with F-SAR radar parameters is used and the coherence is calculated for different Pauli composites with the first acquisition of each flight as master. The right side of Figures 6.1.7 – 6.1.9 shows the height of ambiguity of the same areas. As one would expect, the coherence is higher for urban areas than for forested areas. Figures 6.1.7 – 6.1.9 also show that the coherence of urban areas is highly correlated with the height of ambiguity, more than for forest areas. On the one hand this is because on average the height of ambiguity is lower for the urban areas, because on this test site all urban areas are located in near range while the forest areas are located in far range. For near range the height of ambiguity is lower due to the smaller incidence angle. Note that a smaller height of ambiguity introduces volume decorrelation also in urban scenarios, which is the main decorrelation source in this case. On the other hand, for forested areas temporal decorrelation is the main decorrelation source which is not the case for urban areas. The coherence differences between flight 1 and flight 2 are all due to the differences of the height of ambiguity between flight 1 and flight 2.

In Figures 6.1.10 – 6.1.12 the coherence over time for the three urban areas is shown. The coherences are evaluated in the same manner as the ones in Figures 6.1.4 – 6.1.6. These figures show that there is no drop in coherence between the first and second flight.

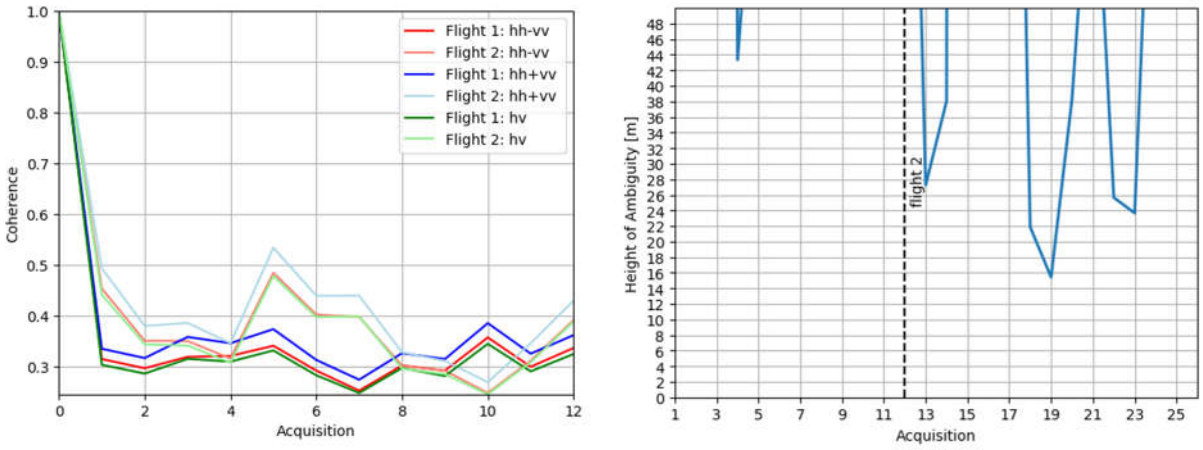

Figure 6.1.1: Left: Coherence of area "Forest 1" for F-SAR parameters for all acquisitions with first acquisition of each flight as master for the different Pauli composites. Right: Height of ambiguity of area "Forest 1".

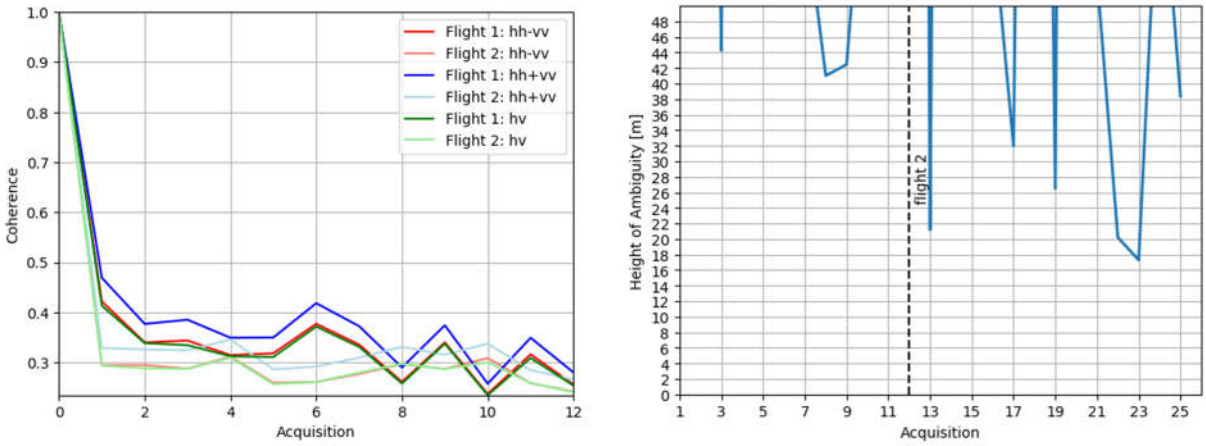

Figure 6.1.2: Left: Coherence of area "Forest 2" for F-SAR parameters for all acquisitions with first acquisition of each flight as master for the different Pauli composites. Right: Height of ambiguity of area "Forest 2".

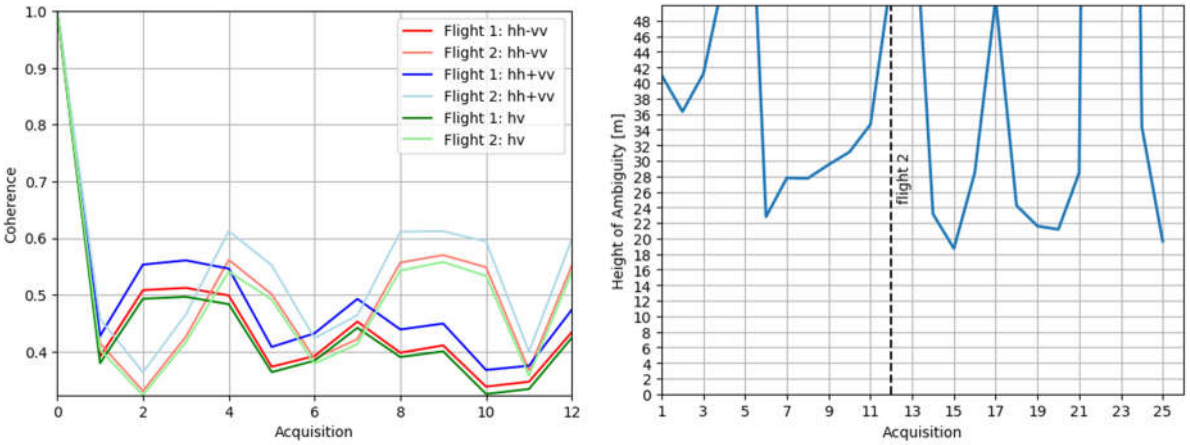

Figure 6.1.3: Left: Coherence of area "Forest 3" for F-SAR parameters for all acquisitions with first acquisition of each flight as master for the different Pauli composites. Right: Height of ambiguity of area "Forest 3".

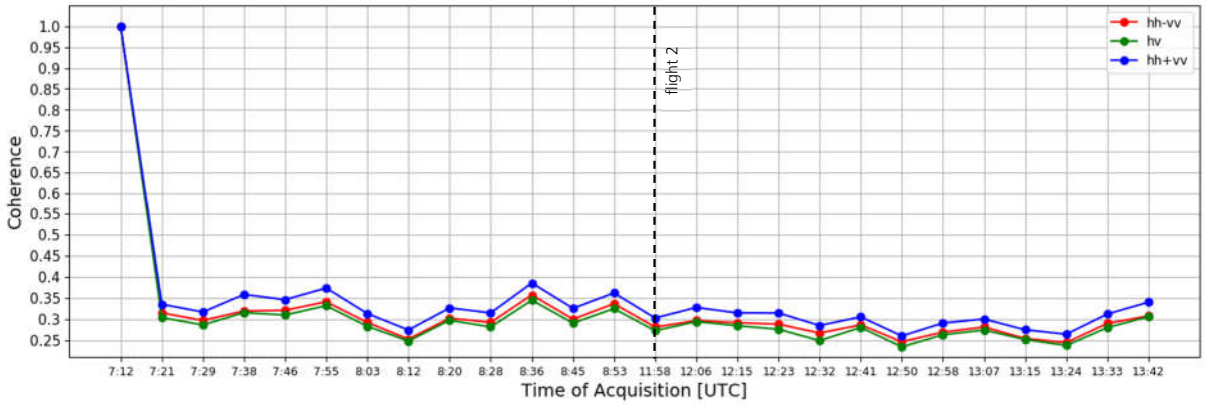

Figure 6.1.4: Coherence over time for F-SAR parameters and area "Forest 1" with first acquisition of first flight as master for the different Pauli composites.

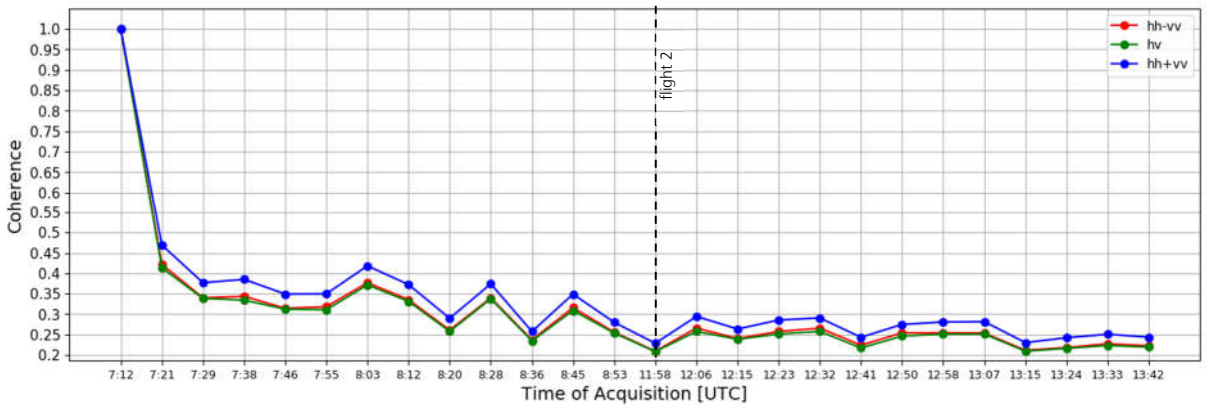

Figure 6.1.5: Coherence over time for F-SAR parameters and area "Forest 2" with first acquisition of first flight as master for the different Pauli composites.

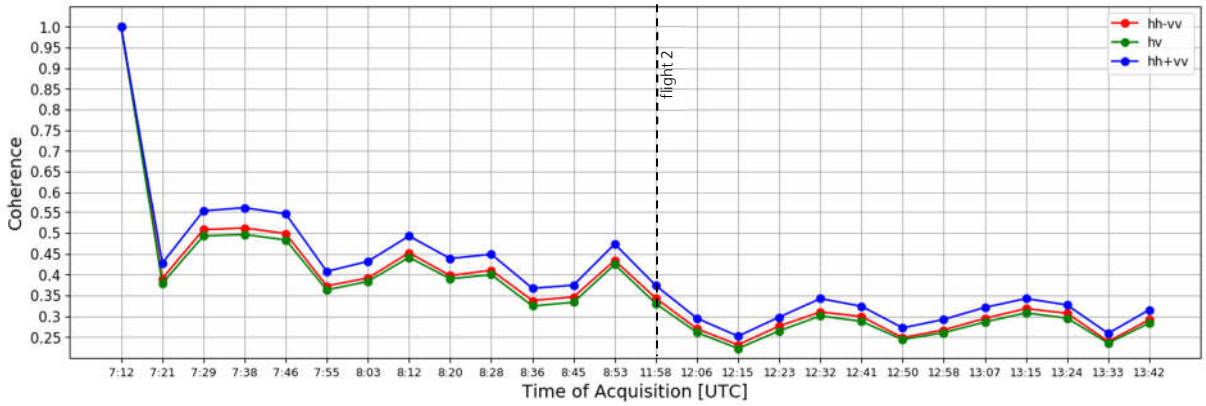

Figure 6.1.6: Coherence over time for F-SAR parameters and area "Forest 3" with first acquisition of first flight as master for the different Pauli composites.

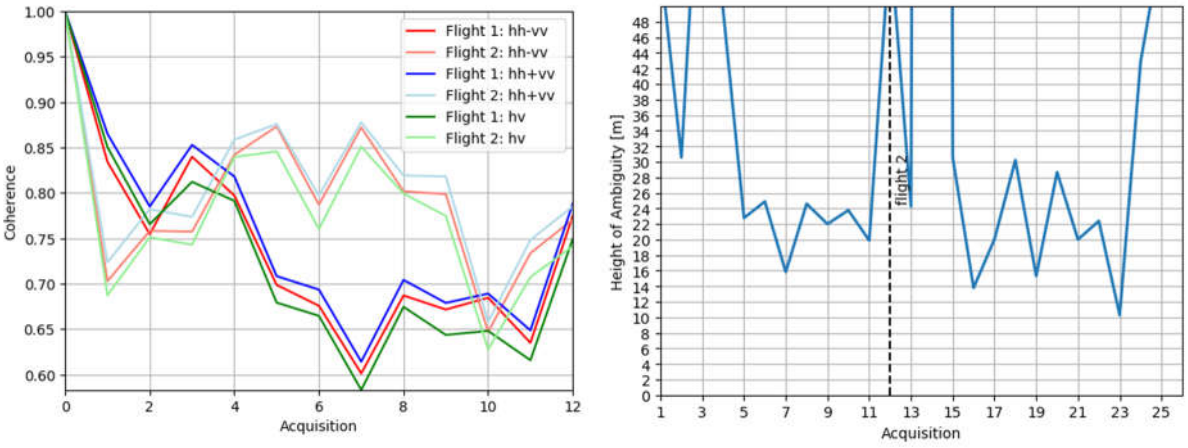

Figure 6.1.7: Left: Coherence of area "Urban 1" for F-SAR parameters for all acquisitions with first acquisition of each flight as master for the different Pauli composites. Right: Height of ambiguity of area "Urban 1".

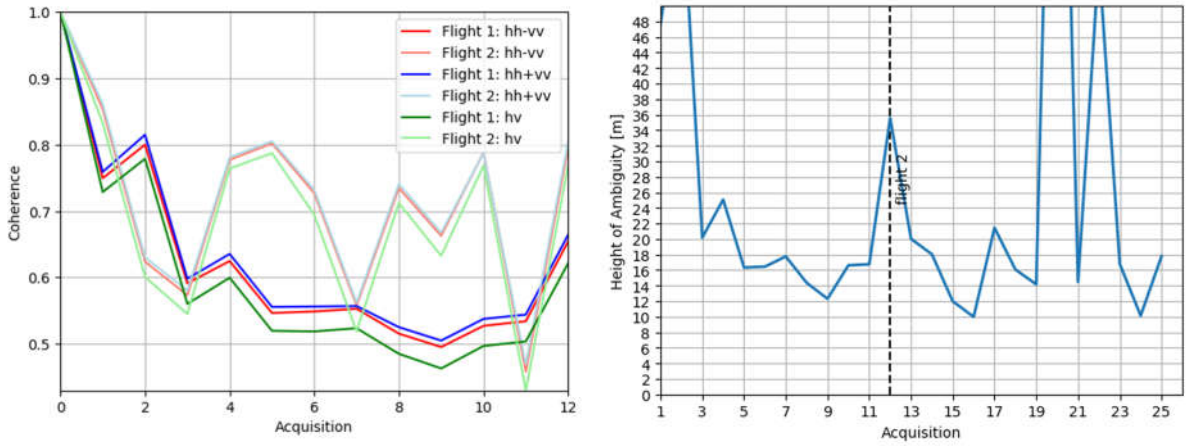

Figure 6.1.8: Left: Coherence of area "Urban 2" for F-SAR parameters for all acquisitions with first acquisition of each flight as master for the different Pauli composites. Right: Height of ambiguity of area "Urban 2".

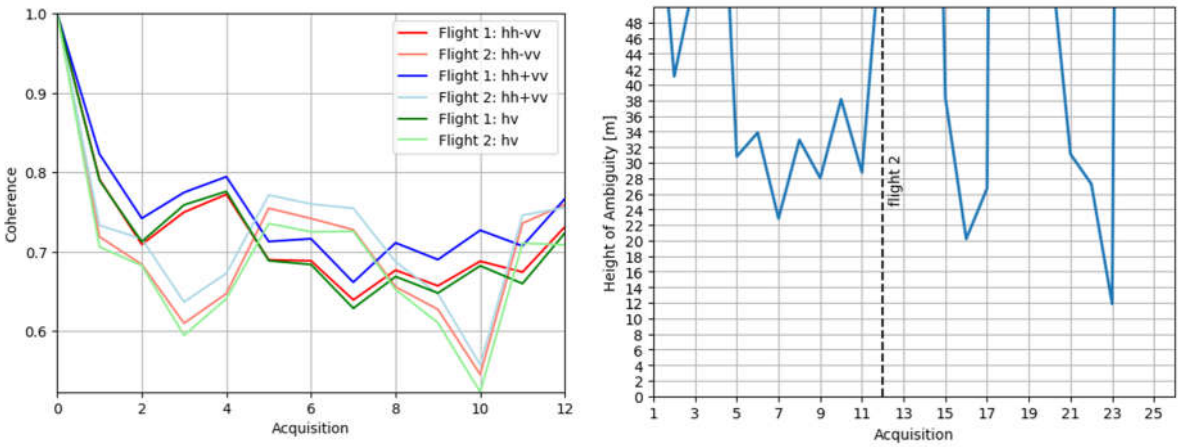

Figure 6.1.9: Left: Coherence of area "Urban 3" for F-SAR parameters for all acquisitions with first acquisition of each flight as master for the different Pauli composites. Right: Height of ambiguity of area "Urban 3".

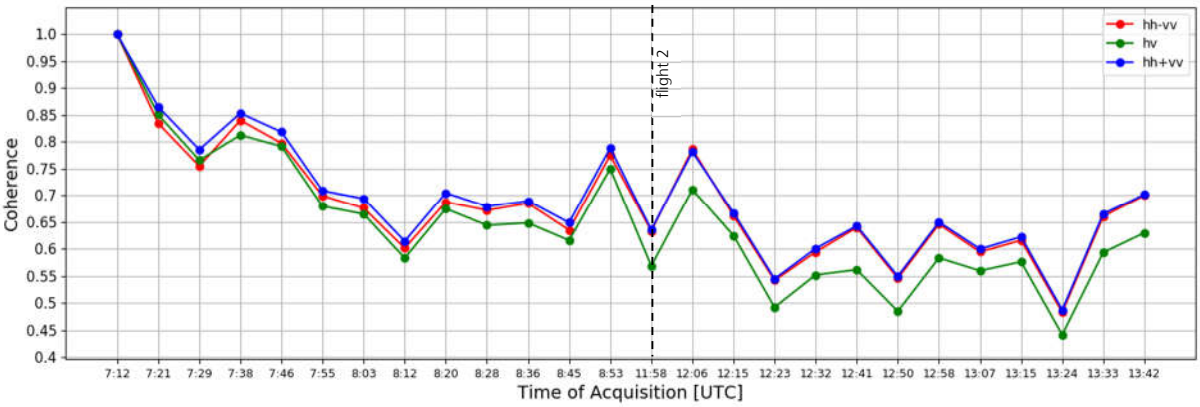

Figure 6.1.10: Coherence over time for F-SAR parameters and area "Urban 1" with first acquisition of first flight as master for the different Pauli composites.

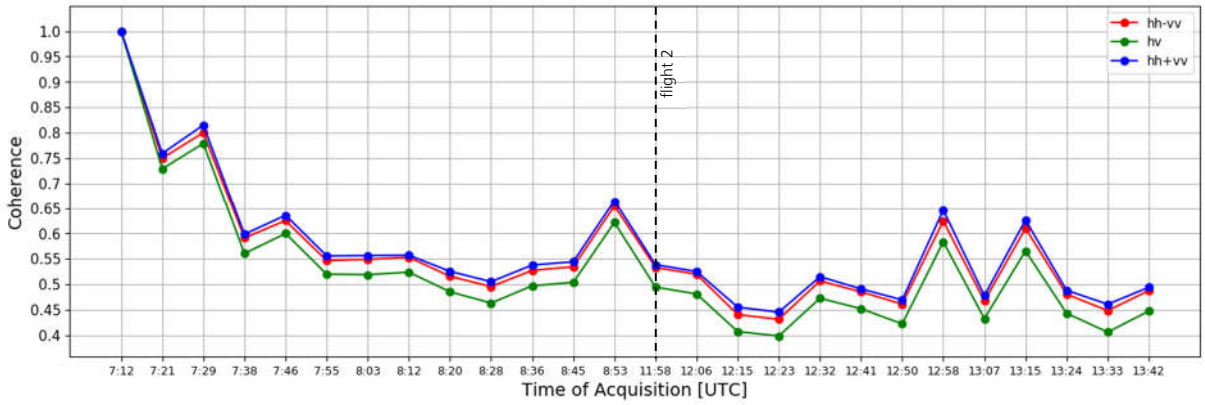

Figure 6.1.11: Coherence over time for F-SAR parameters and area "Urban 2" with first acquisition of first flight as master for the different Pauli composites.

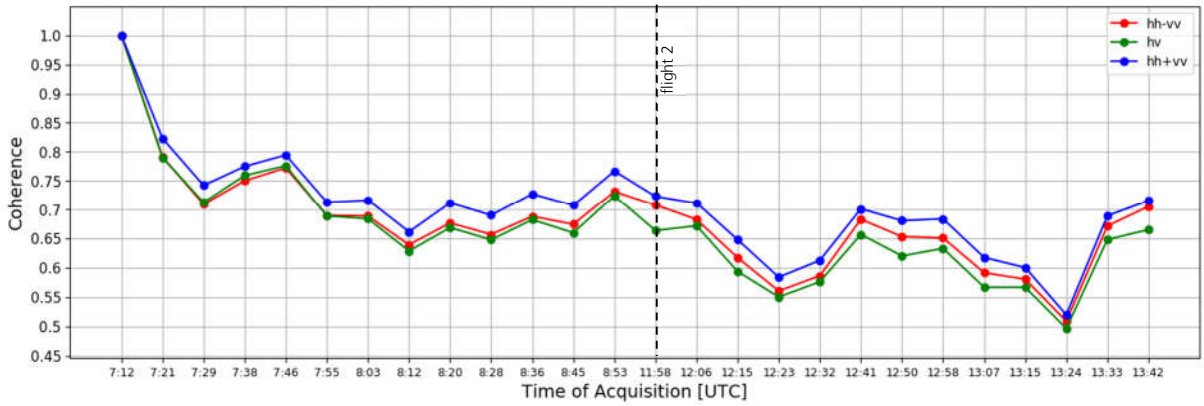

Figure 6.1.12: Coherence over time for F-SAR parameters and area "Urban 3" with first acquisition of first flight as master for the different Pauli composites.

6.2 Coherence of Time Series with Hydroterra Radar Parameters

In this section the coherences of forest and urban areas are evaluated for the time series with Hydroterra radar parameters and compared to the ones of the time series with F-SAR radar parameters from Chapter 6.1.

Figure 6.2.1 shows the coherences of the three forested areas for time series with Hydroterra parameters. The coherences are evaluated for the different Pauli composites and for each acquisition. The first acquisition of each flight is used as master. The coherences of the forest areas are lower for Hydroterra time series than for F-SAR time series, because of the higher thermal decorrelation due to a lower signal-to-noise ratio (SNR). For forest areas "Forest 1" and "Forest 2" the coherence drops at the second acquisition and no variations due to volume decorrelation are visible. For the area "Forest 3" similar variations due to volume decorrelation can be seen as for the coherences with F-SAR parameters in Figure 6.1.3. Here the coherence of volume scattering is lower due to the lower SNR as compared to the other Pauli composites.

Figure 6.2.2 shows the coherences of time series with Hydroterra parameters of the three urban areas. The coherences are evaluated in the same manner as in Figure 6.2.1. A comparison of these coherences to the ones for F-SAR parameters in Figures 6.1.7 – 6.1.9 shows that variations occur for the same acquisitions due to changes of the height of ambiguity. The variations of the coherences for Hydroterra parameters are however significantly more pronounced. This is due to a reduced amount of samples which are available to estimate the coherence in time series with Hydroterra parameters as compared to the time series with F-SAR parameters. For F-SAR time series 400 x 400 samples are available at each acquisition to estimate the coherences of the areas "Urban 1" and "Urban 2" and 500 x 500 samples are available at each acquisition to estimate the coherences of the area "Urban 3". For Hydroterra time series 28 x 6 samples are available at each acquisition to estimate the coherences of the areas "Urban 1" and "Urban 2" and 35 x 7 samples are available at each acquisition to estimate the coherences of the area "Urban 3". The coherences of urban areas for Hydroterra parameters are not generally lower than the ones of F-SAR parameters. This is because the SNR is relatively high in urban areas; therefore thermal decorrelation does not impact the coherence significantly.

Figures 6.2.4 – 6.2.9 show the coherences over time for the three forest and urban areas. Like for the coherences over time from Chapter 6.1, also here no coherence drop is visible between flight 1 and flight 2.

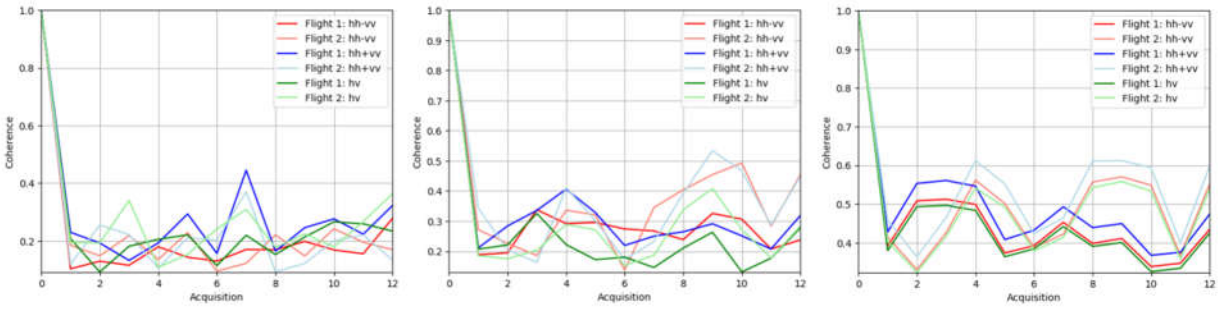

Figure 6.2.1: Coherence for Hydroterra parameters for all acquisitions with first acquisition of each flight as master for the different Pauli composites. Left: "Forest 1", middle: "Forest 2", right: "Forest 3".

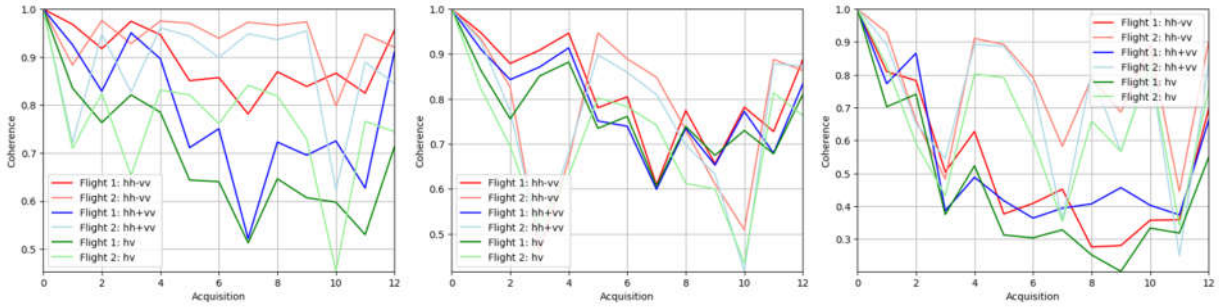

Figure 6.2.2: Coherence for Hydroterra parameters for all acquisitions with first acquisition of each flight as master for the different Pauli composites. Left: "Urban 1", middle: "Urban 2", right: "Urban 3".

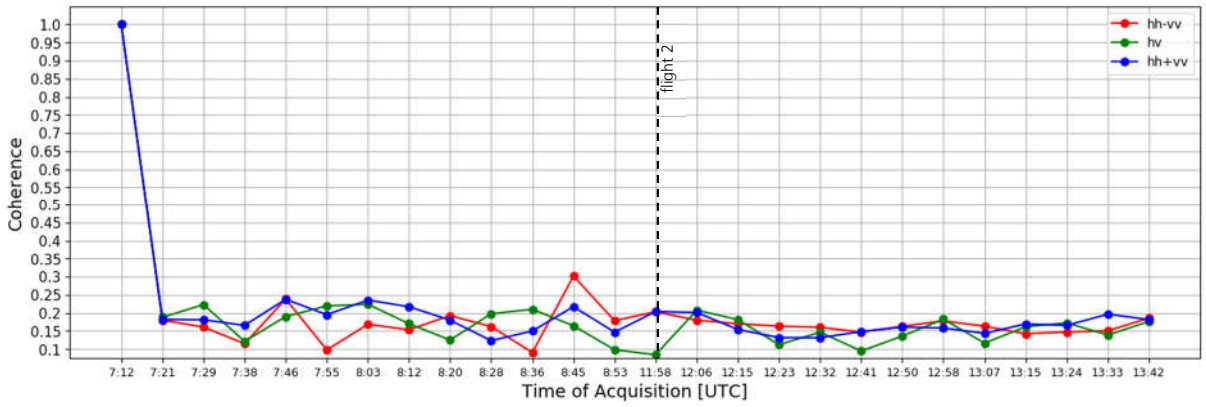

Figure 6.2.4: Coherence over time for Hydroterra parameters and area "Forest 1" with first acquisition of first flight as master for the different Pauli composites.

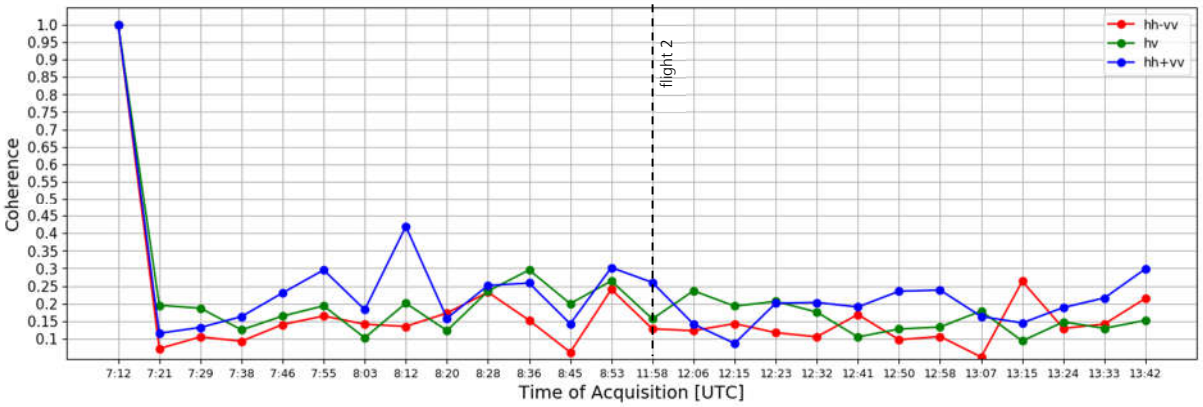

Figure 6.2.5: Coherence over time for Hydroterra parameters and area "Forest 2" with first acquisition of first flight as master for the different Pauli composites.

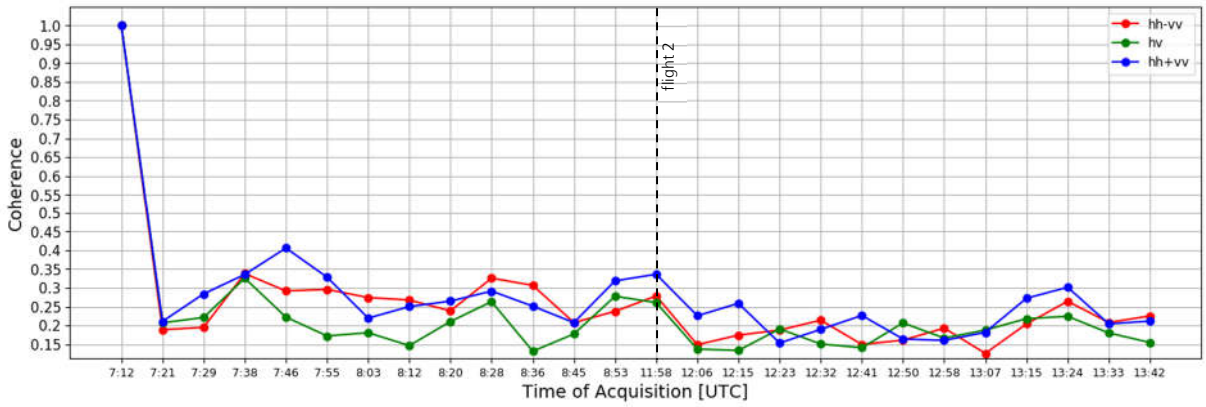

Figure 6.2.6: Coherence over time for Hydroterra parameters and area "Forest 3" with first acquisition of first flight as master for the different Pauli composites.

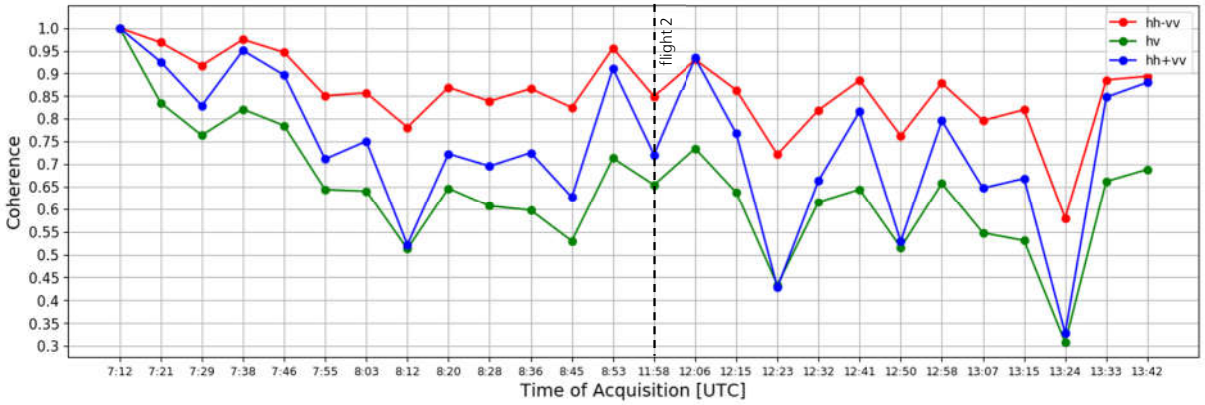

Figure 6.2.7: Coherence over time for Hydroterra parameters and area "Urban 1" with first acquisition of first flight as master for the different Pauli composites.

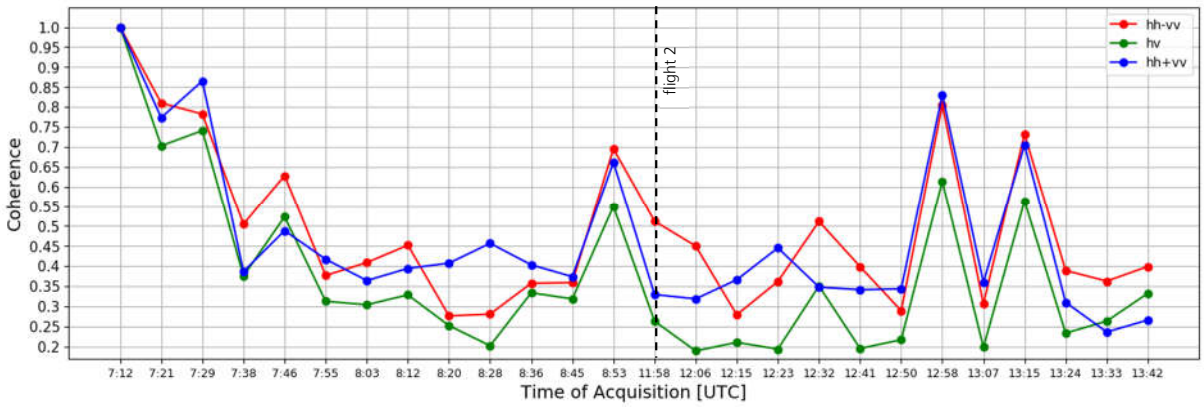

Figure 6.2.8: Coherence over time for Hydroterra parameters and area "Urban 2" with first acquisition of first flight as master for the different Pauli composites.

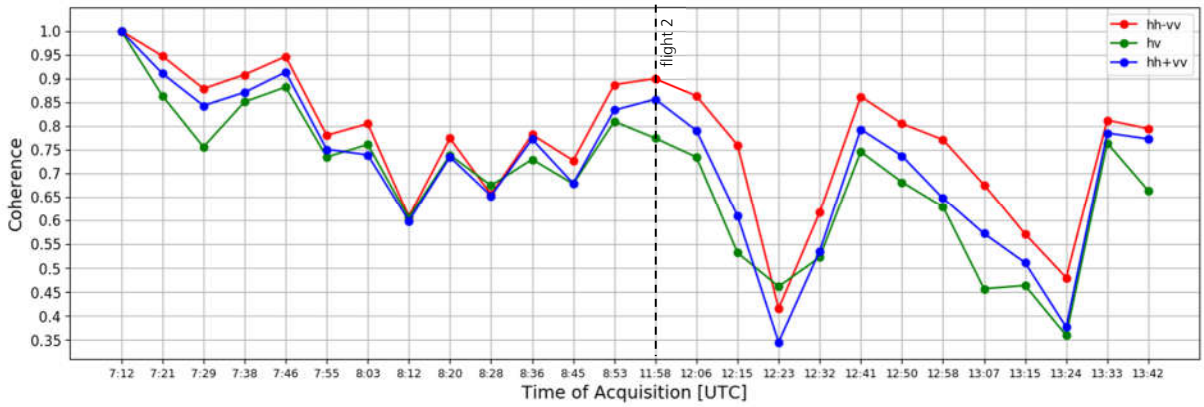

Figure 6.2.9: Coherence over time for Hydroterra parameters and area "Urban 3" with first acquisition of first flight as master for the different Pauli composites.

6.3 Coherence Analysis of Simulated Hydroterra Products

Like in Chapter 5.2, also in this section the coherence of the simulated Hydroterra products is evaluated and compared to the one of the time series with Hydroterra radar parameters. Here this is performed for the three forested and urban areas.

Tables 6.3.1 – 6.3.2 show the mean coherence, the Hydroterra coherence and the difference between them for all polarisations. The mean coherence refers to the average of all coherences between all acquisitions of the first flight and all acquisitions of the second flight. Tables 6.3.1 – 6.3.2 show that the mean and Hydroterra coherences are very similar, except for the urban area "Urban 2". Here the coherences differ, because moving targets were present in the scene for some acquisitions.

Survey Point	Mean Coherence	Hydroterra Coherence	Difference
"Forest 1"	0.137	0.126	-0.011
"Forest 2"	0.124	0.068	-0.058
"Forest 3"	0.138	0.137	-0.001
"Urban 1"	0.872	0.814	-0.058
"Urban 2"	0.601	0.333	-0.268
"Urban 3"	0.780	0.870	0.089

Table 6.3.1: Comparison between mean and Hydroterra coherence for the HH polarisation. The mean coherence is computed from all coherences between flight 1 and flight 2. The Hydroterra coherence is calculated from the simulated Hydroterra products of flight 1 and flight 2.

Survey Point	Mean Coherence	Hydroterra Coherence	Difference
"Forest 1"	0.120	0.071	-0.049
"Forest 2"	0.120	0.040	-0.063
"Forest 3"	0.095	0.059	-0.037
"Urban 1"	0.645	0.613	-0.032
"Urban 2"	0.495	0.326	-0.169
"Urban 3"	0.610	0.683	0.073

Table 6.3.2: Comparison between mean and Hydroterra coherence for the HV polarisation. The mean coherence is computed from all coherences between flight 1 and flight 2. The Hydroterra coherence is calculated from the simulated Hydroterra products of flight 1 and flight 2.

Survey Point	Mean Coherence	Hydroterra Coherence	Difference
"Forest 1"	0.120	0.221	0.101
"Forest 2"	0.103	0.042	-0.062
"Forest 3"	0.141	0.146	0.004
"Urban 1"	0.817	0.762	-0.055
"Urban 2"	0.574	0.268	-0.306
"Urban 3"	0.672	0.797	0.125

Table 6.3.3: Comparison between mean and Hydroterra coherence for the VV polarisation. The mean coherence is computed from all coherences between flight 1 and flight 2. The Hydroterra coherence is calculated from the simulated Hydroterra products of flight 1 and flight 2.

7 Survey Point Analysis with SSM Agro Parameters

As part of 'WP400 – Time Series with SSM Agro Parameters', DLR has simulated single-look complex (SLC) and multi-look detected (ML) time series from F-SAR data with Hydroterra soil moisture for agriculture product (SSM Agro) parameters. The relevant SSM Agro parameters are summarized in Table 7.1, while Figure 7.1 shows single-look complex images for all polarizations in slant-range geometry of the first acquisition of the time series with SSM Agro parameters, corresponding to the first flight. To simulate time series with Hydroterra parameters, each acquisition of the F-SAR time series is filtered to the resolution of the SSM Agro parameters in slant range and azimuth, the sampling is adjusted and energy normalization is performed. Additionally, the NESZ of each acquisition is adjusted to the one of the SSM Agro product. This procedure is also described in [8].
In this chapter the intensity, coherence and interferometric phase of F-SAR data are compared to the ones of simulated Hydroterra time series with SSM Agro parameters. In chapter 4 the intensity, coherence and interferometric phase were analyzed making use of the Pauli decomposition, since each of its components can be directly related to nominal scattering mechanisms (double bounce, single bounce and volume) and allows for a better qualitative interpretation of the resulting RGB images. In this chapter, however, the lexicographic decomposition is used, because a single polarization is the threshold requirement for the Hydroterra mission.
In Figures 7.2 – 7.4 the intensity of the six survey points of the F-SAR time series are presented for the different polarizations. Figures 7.5 – 7.13 show the coherence and Figures 7.14 – 7.16 present the interferometric phase. The only difference between the intensity, coherence and interferometric phase shown in this chapter and the ones in Chapter 4 is the different polarimetric decomposition, as noted above. Here the different parameters of the F-SAR time series are demonstrated for the lexicographic decompositions, to have a better comparison to the ones of the simulated time series with SSM Agro parameters. The results found in Figures 7.2 – 7.16 do not differ from the ones in Chapter 4. They are therefore not again described in this chapter. In Figures 7.2 – 7.4 the intensity of the HH polarization is higher for all the survey points except for "A30", while in Chapter 4.1 the odd bounce scattering has the highest signal.
Figures 7.17 – 7.31 show the intensity, coherence and interferometric phase of simulated Hydroterra time series with SSM Agro parameters for the different polarizations. These images are similar to the ones shown in Chapter 5. In Chapter 5 the intensity, coherence and interferometric phase of time series with Hydroterra parameters of the scenario 4 were analyzed for the different Pauli components. One difference is the intensity of the SSM Agro times series in Figures 7.17 – 7.19, due to the different resolution and sampling size. In Figures 7.17 – 7.19 a drop between the first and second flight is visible for the survey points "B18", "B22" and "B03". A rise of the intensity is also evident for the survey point "A30" in Figure 7.19. A drop or rise of the intensity was less evident for the Hydroterra scenario 4 time series in Chapter 5. Other differences are the higher coherence of the HV polarization as this is the case in Chapter 5. This is due to the lower NESZ of the SSM Agro time series as compared to the one of the Hydroterra scenario 4 time series. Other differences are that the interferometric phase of the survey point "A30" in Figure 7.31 is different for the HV polarization as compared to the HH and VV polarizations for the second flight. In Chapter 5 such a difference was not observed for the Pauli decomposition. For the survey point "B03" a difference in the coherence between the first and the second flight in Figure 7.22 is only visible for the HH polarization, while in Chapter 5 a difference for the volume and odd bounce scattering component was observed.
For a comparison of the intensity, coherence and interferometric phase between the F-SAR data and the simulated Hydroterra time series with SSM Agro parameters, the reader is referred to Chapter 5, since the results of this comparison are equal to the ones which are found in Chapter 5.

Parameter	Value
Single-look azimuth resolution	11.1 m
Multi-look azimuth resolution	199.8 m
Number of azimuth looks	18
Range bandwidth	8.8 MHz
Single-look slant range resolution	15.2 m
Multi-look slant range resolution	106.1 m
Number of range looks	7
NESZ	-22.4 dB

Table 7.1: Relevant parameters of scenario 3 used for Hydroterra time series simulation.

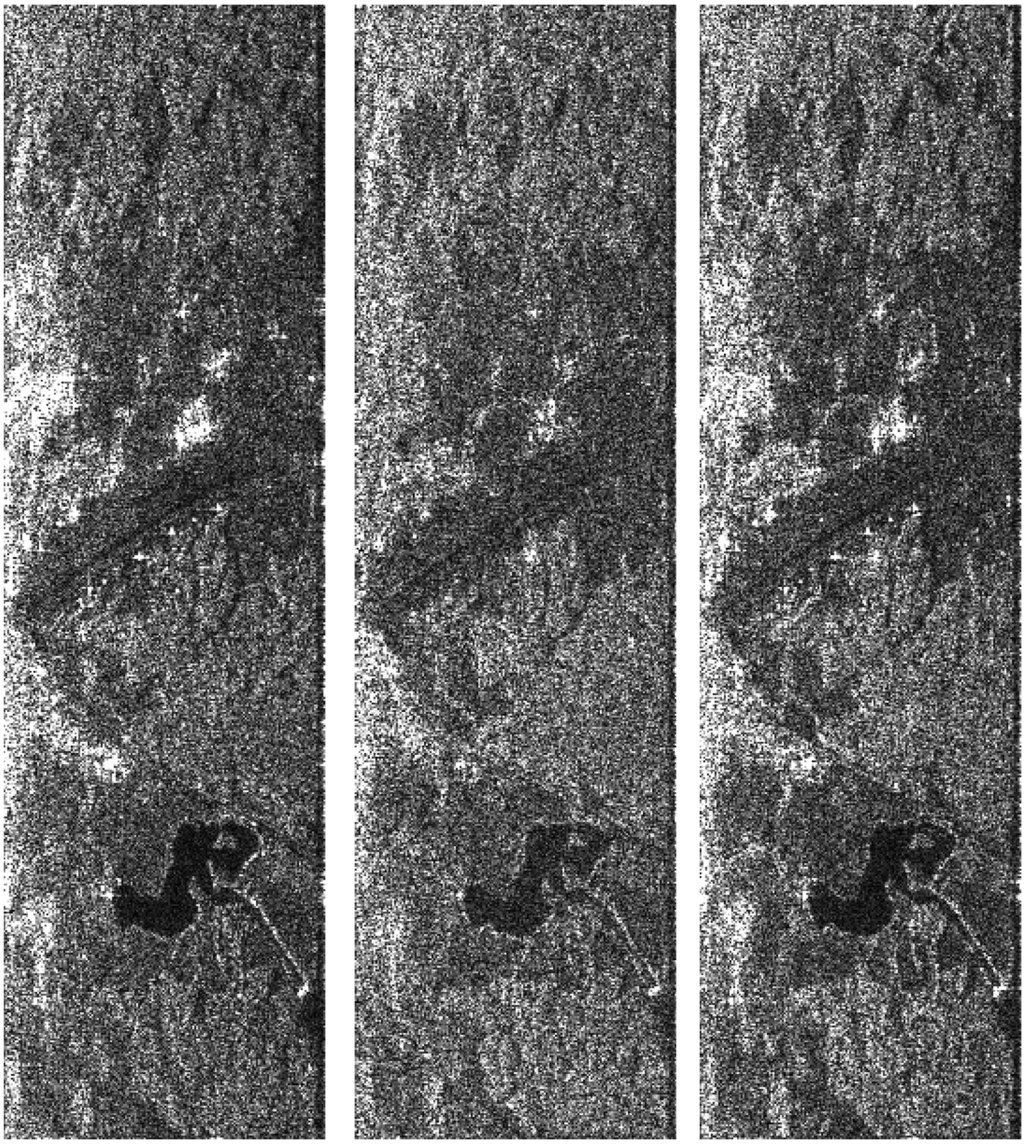

Figure 7.1: Amplitude of single-look complex image in slant range geometry of first acquisition of time series with SSM Agro parameters of first flight. Left: HH polarization, middle: HV polarization, right VV polarization. Image size: 6503.06 m in azimuth x 2258.48 m in slant range.

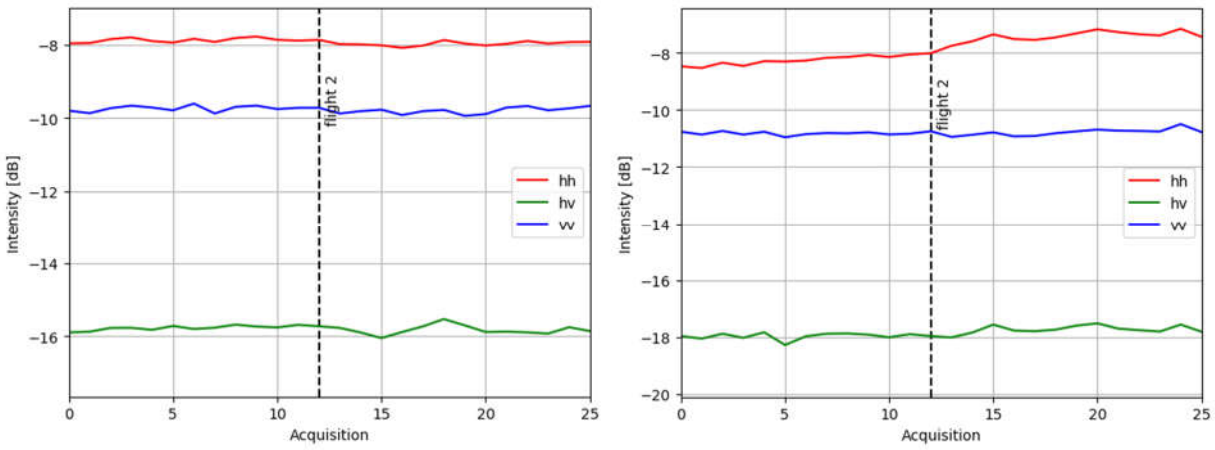

Figure 7.2: Intensity of the different polarimetric channels for F-SAR parameters. Left: For survey point "A16", right: For survey point "B01".

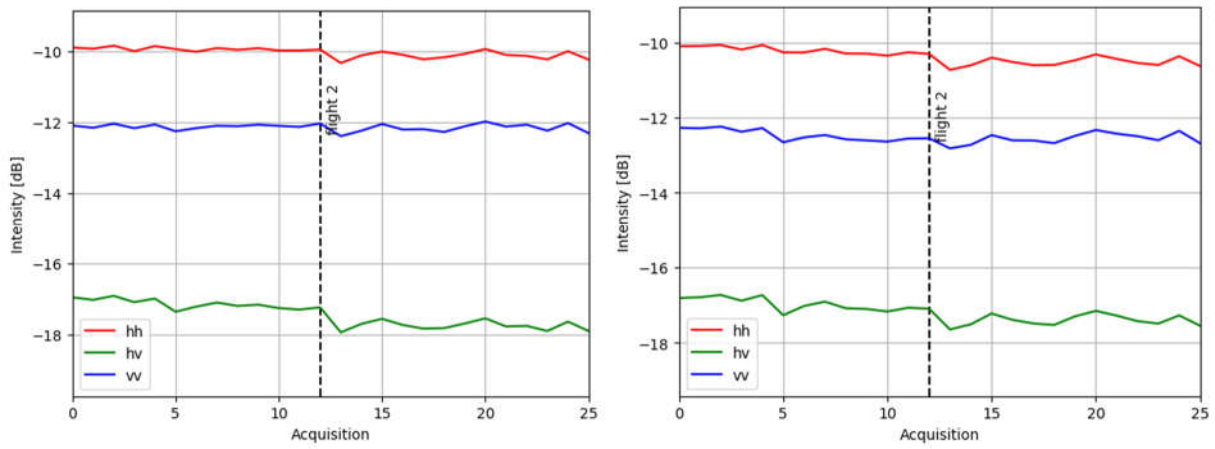

Figure 7.3: Intensity of the different polarimetric channels for F-SAR parameters. Left: For survey point "B18", right: For survey point "B22".

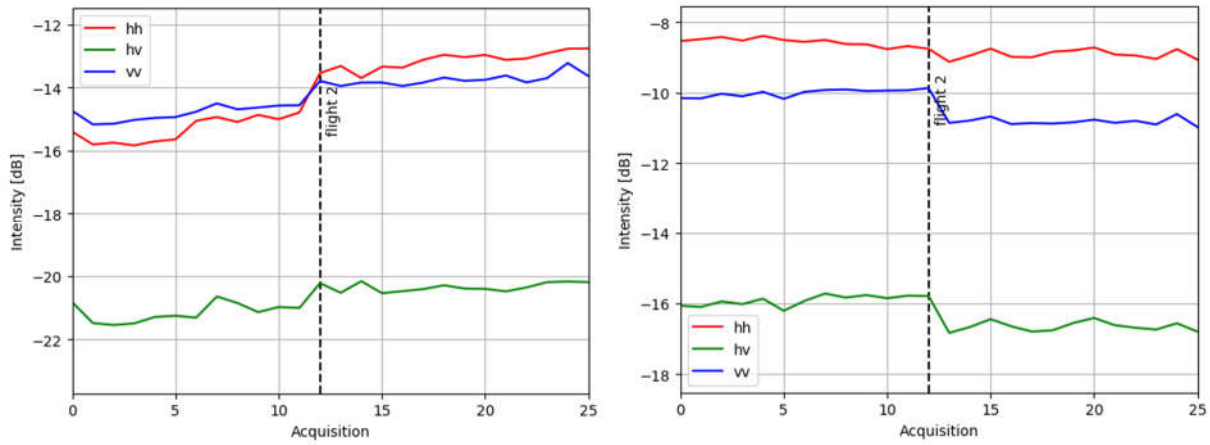

Figure 7.4: Intensity of the different polarimetric channels for F-SAR parameters. Left: For survey point "A30", right: For survey point "B03".

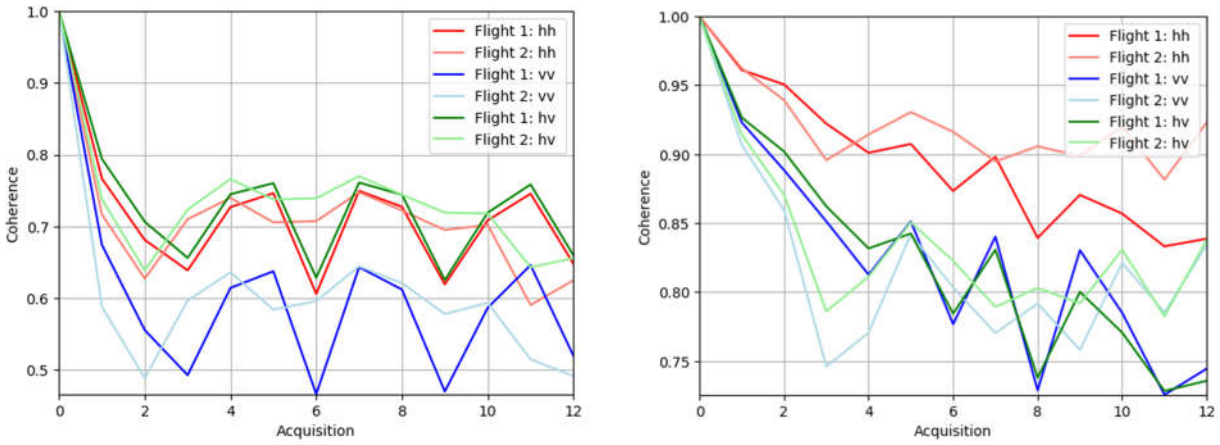

Figure 7.5: Coherence for F-SAR parameters for all acquisitions with first acquisition of each flight as master for the different polarimetric channels. Left: For survey point "A16", right: For survey point "B01".

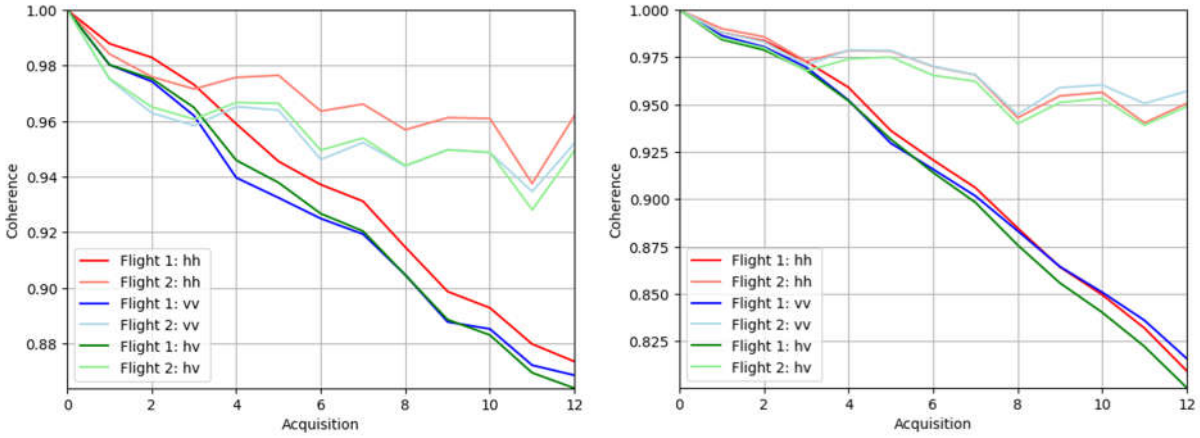

Figure 7.6: Coherence for F-SAR parameters for all acquisitions with first acquisition of each flight as master for the different polarimetric channels. Left: For survey point "B18", right: For survey point "B22".

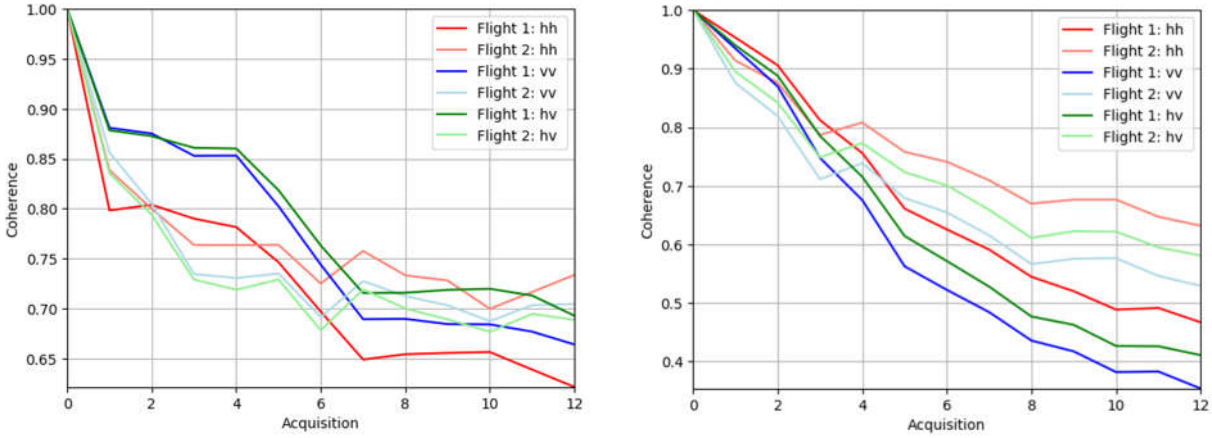

Figure 7.7: Coherence for F-SAR parameters for all acquisitions with first acquisition of each flight as master for the different polarimetric channels. Left: For survey point "A30", right: For survey point "B03".

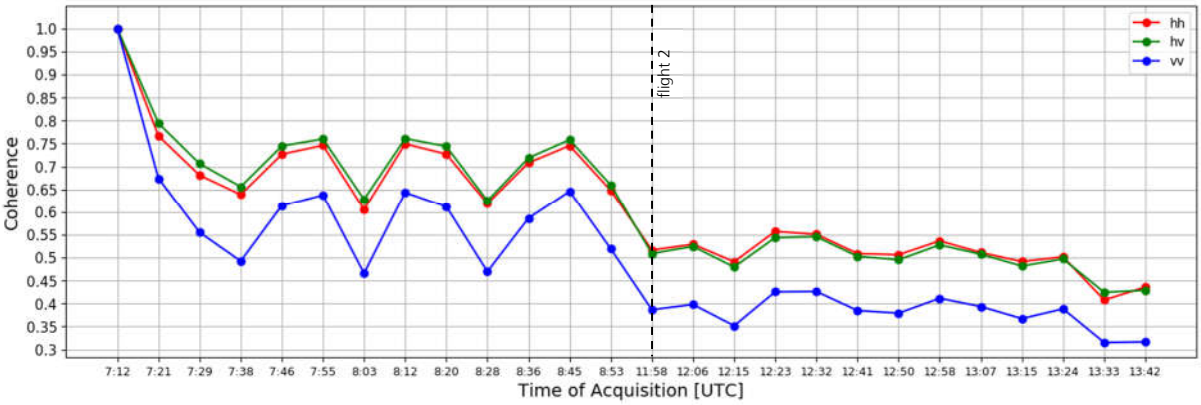

Figure 7.8: Coherence over time for F-SAR parameters and survey point "A16" with first acquisition of first flight as master for the different polarimetric channels.

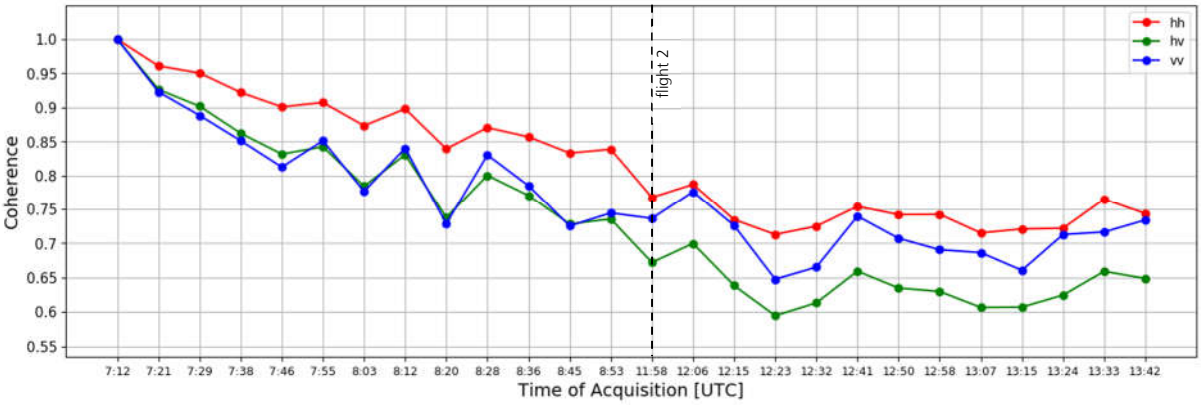

Figure 7.9: Coherence over time for F-SAR parameters and survey point "B01" with first acquisition of first flight as master for the different polarimetric channels.

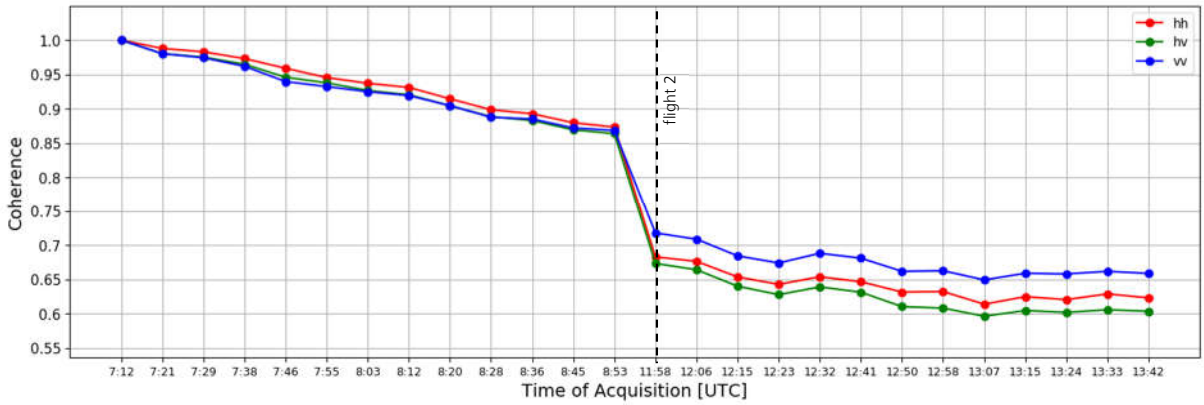

Figure 7.10: Coherence over time for F-SAR parameters and survey point "B18" with first acquisition of first flight as master for the different polarimetric channels.

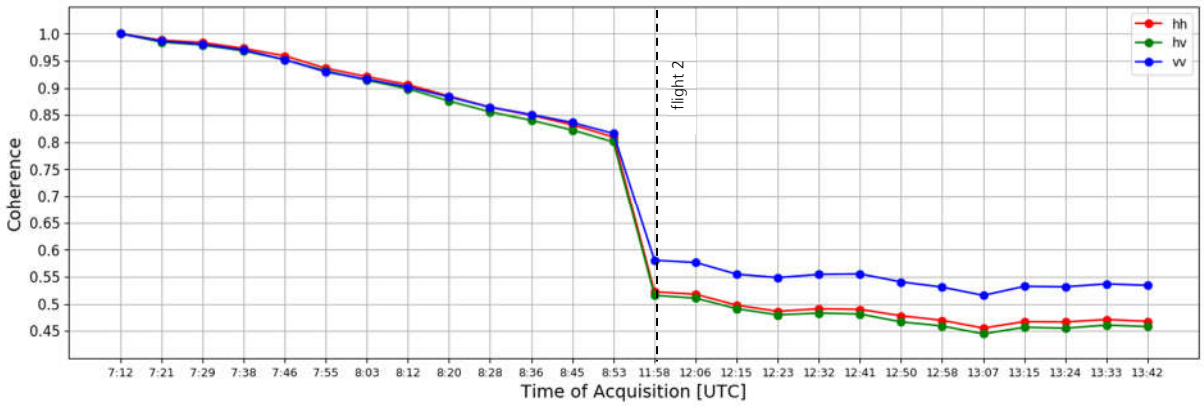

Figure 7.11: Coherence over time for F-SAR parameters and survey point "B22" with first acquisition of first flight as master for the different polarimetric channels.

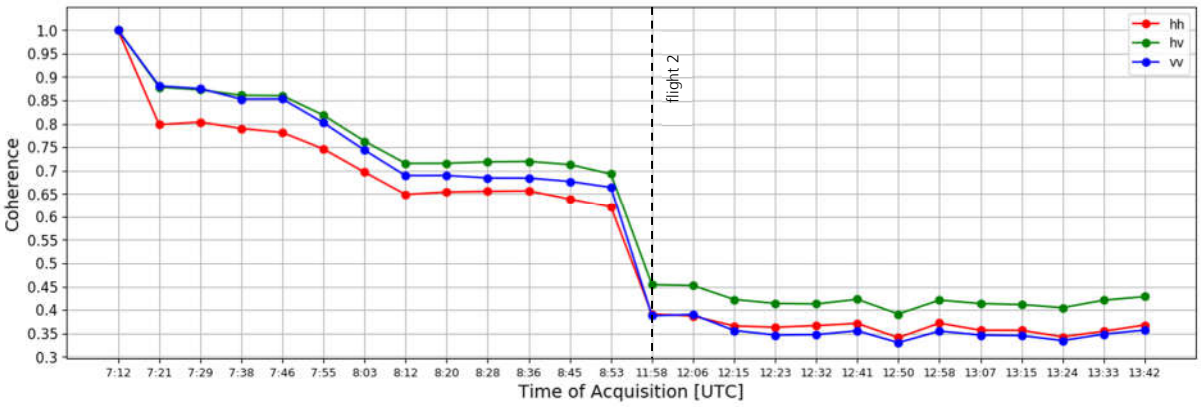

Figure 7.12: Coherence over time for F-SAR parameters and survey point "A30" with first acquisition of first flight as master for the different polarimetric channels.

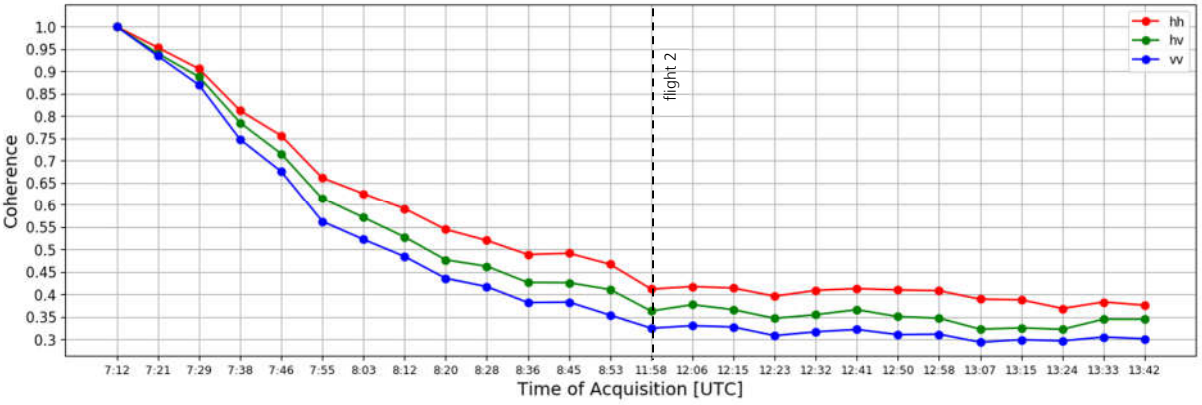

Figure 7.13: Coherence over time for F-SAR parameters and survey point "B03" with first acquisition of first flight as master for the different polarimetric channels.

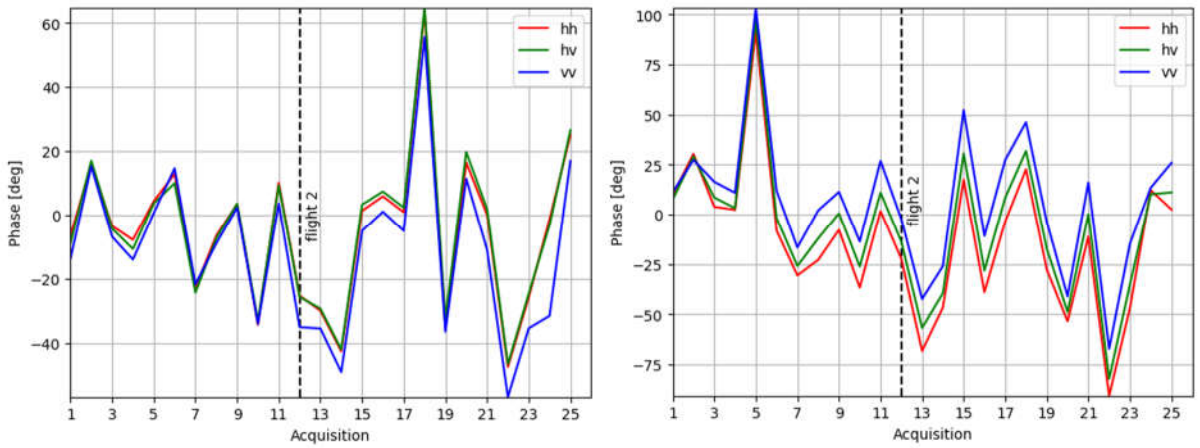

Figure 7.14: Interferometric phase for F-SAR parameters with first acquisition of first flight as master for the different polarimetric channels. Left: For survey point "A16", right: For survey point "B01".

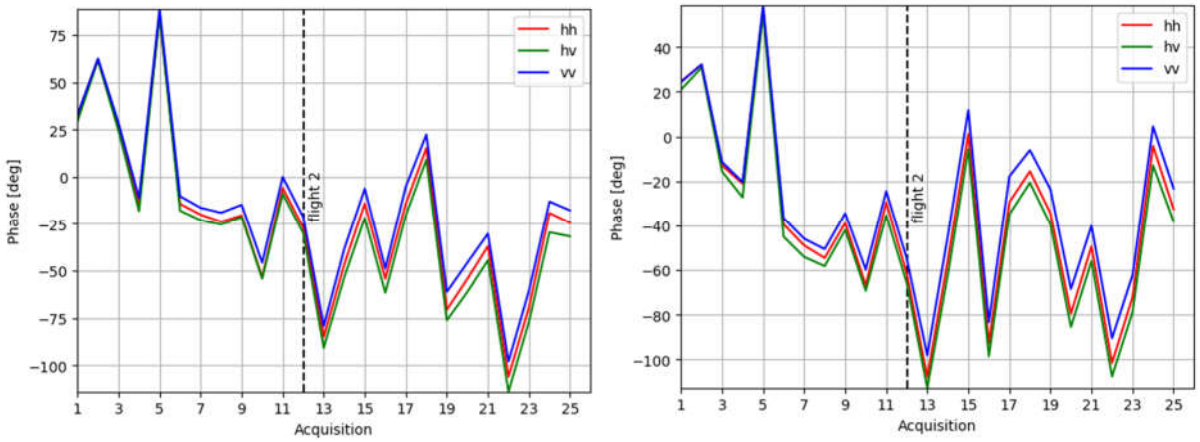

Figure 7.15: Interferometric phase for F-SAR parameters with first acquisition of first flight as master for the different polarimetric channels. Left: For survey point "B18", right: For survey point "B22".

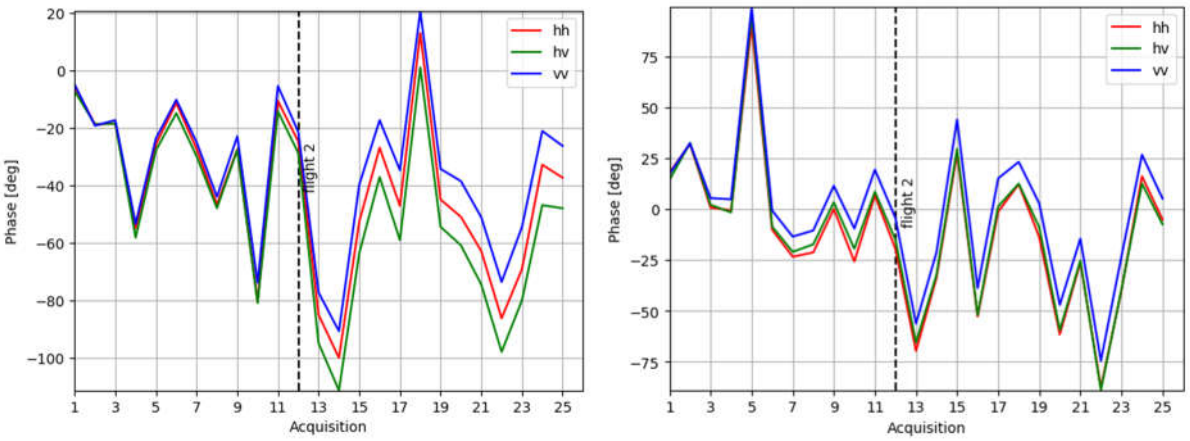

Figure 7.16: Interferometric phase for F-SAR parameters with first acquisition of first flight as master for the different polarimetric channels. Left: For survey point "A30", right: For survey point "B03".

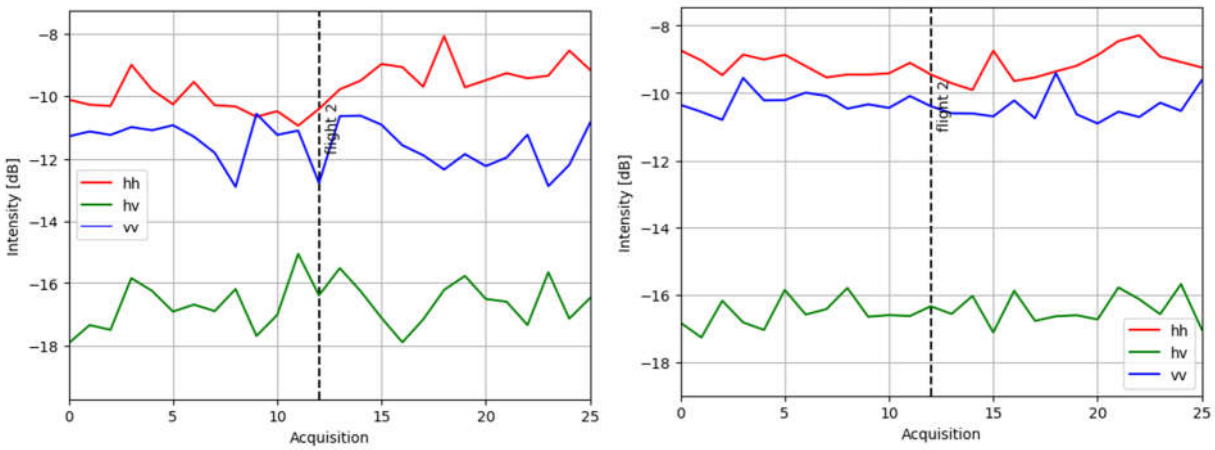

Figure 7.17: Intensity of the different polarimetric channels for Hydroterra parameters. Left: For survey point "A16", right: For survey point "B01".

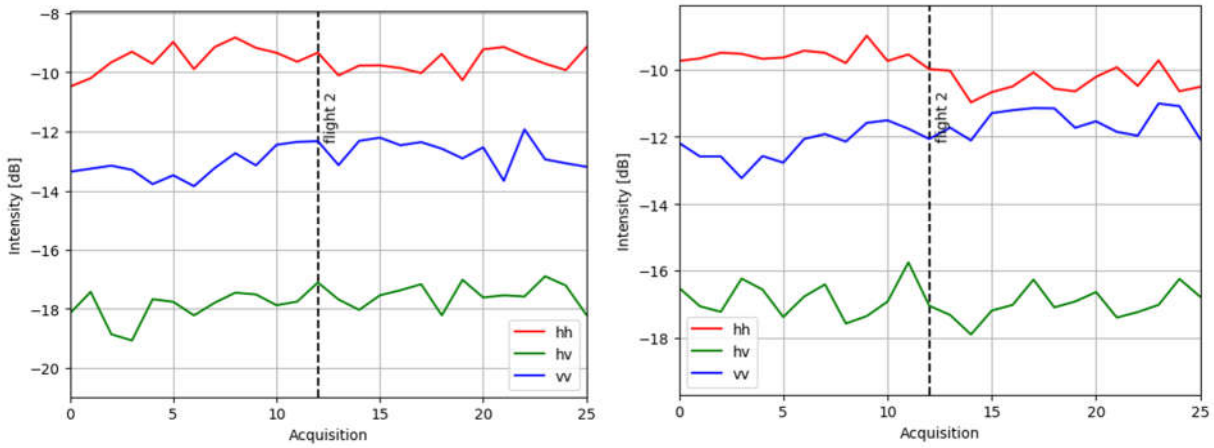

Figure 7.18: Intensity of the different polarimetric channels for Hydroterra parameters. Left: For survey point "B18", right: For survey point "B22".

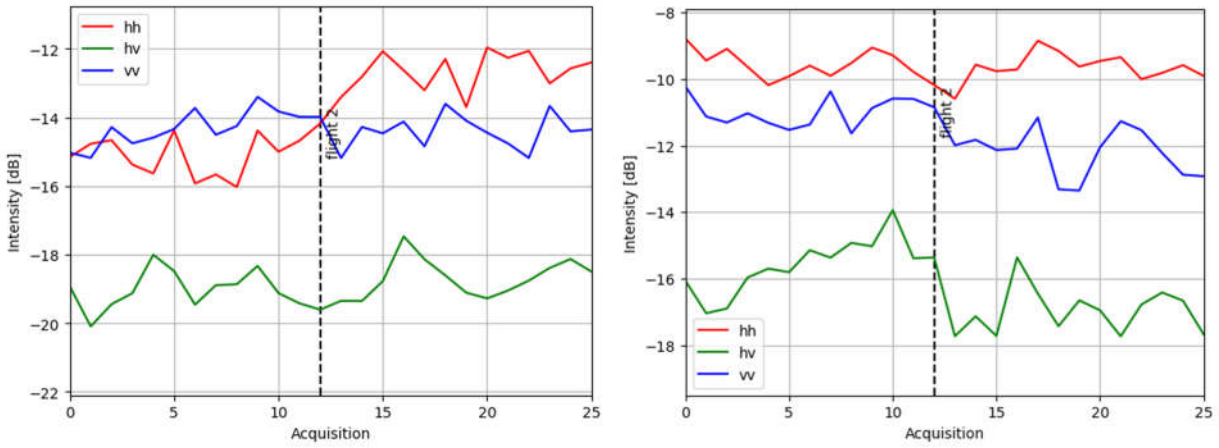

Figure 7.19: Intensity of the different polarimetric channels for Hydroterra parameters. Left: For survey point "A30", right: For survey point "B03".

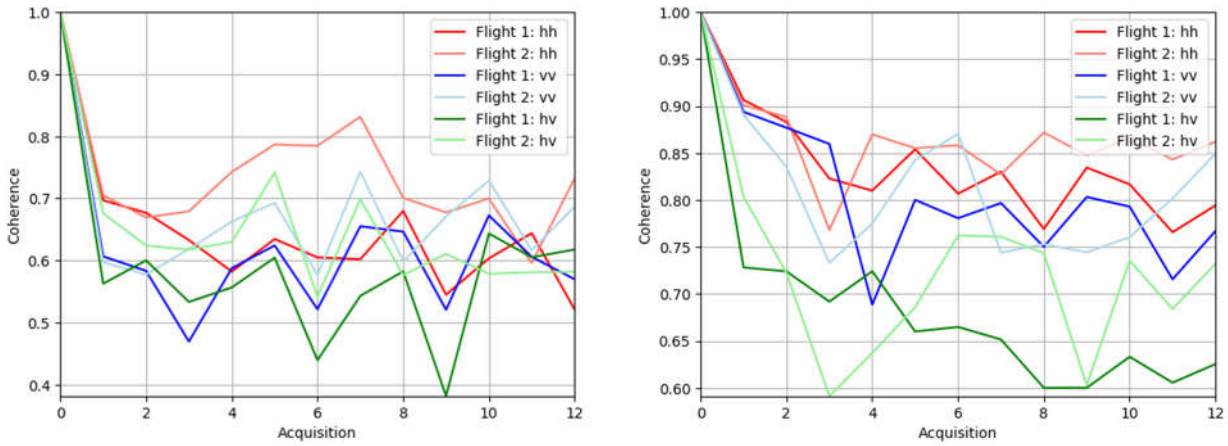

Figure 7.20: Coherence for Hydroterra parameters for all acquisitions with first acquisition of each flight as master for the different polarimetric channels. Left: For survey point "A16", right: For survey point "B01".

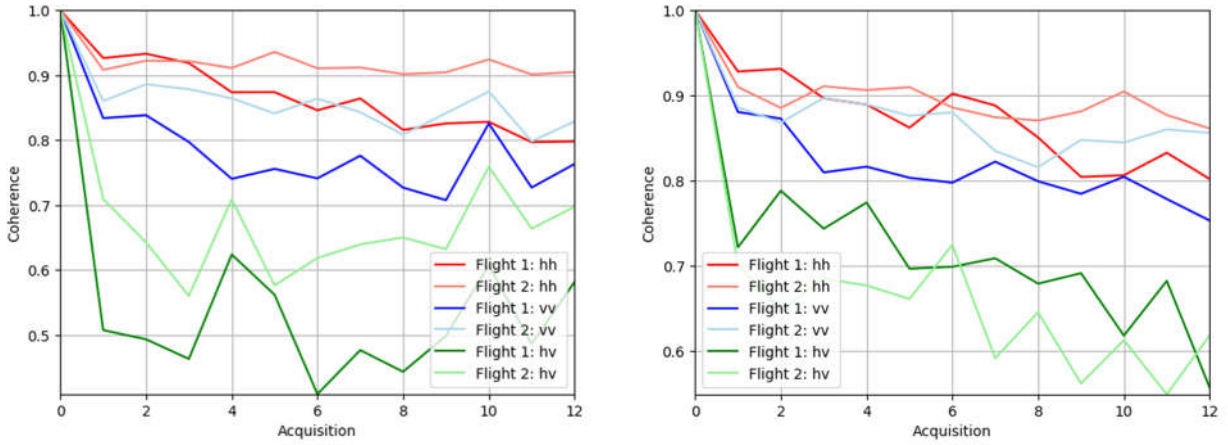

Figure 7.21: Coherence for Hydroterra parameters for all acquisitions with first acquisition of each flight as master for the different polarimetric channels. Left: For survey point "B18", right: For survey point "B22".

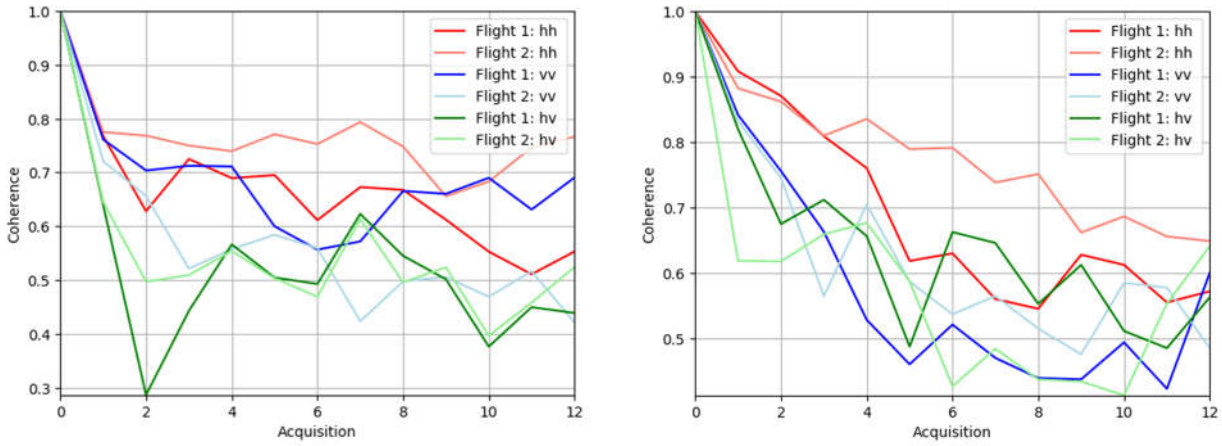

Figure 7.22: Coherence for Hydroterra parameters for all acquisitions with first acquisition of each flight as master for the different polarimetric channels. Left: For survey point "A30", right: For survey point "B03".

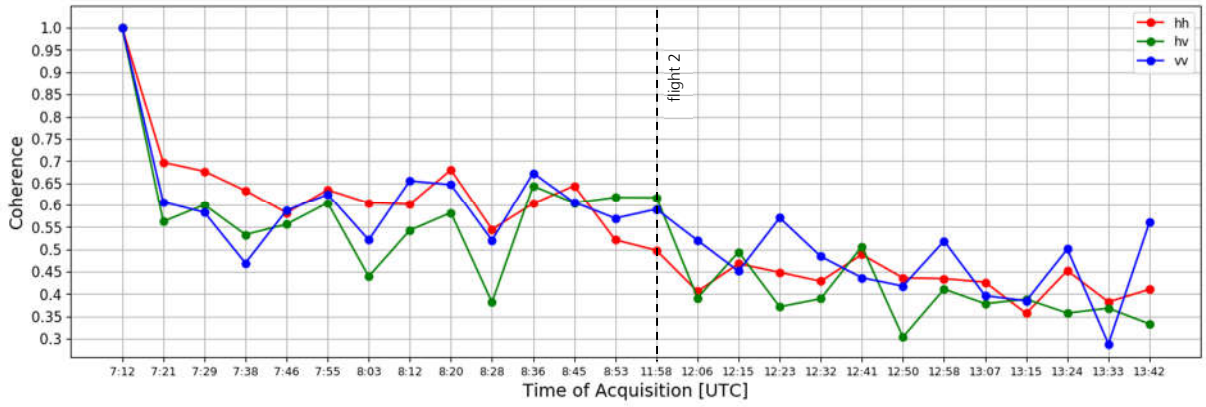

Figure 7.23: Coherence over time for Hydroterra parameters and survey point "A16" with first acquisition of first flight as master for the different polarimetric channels.

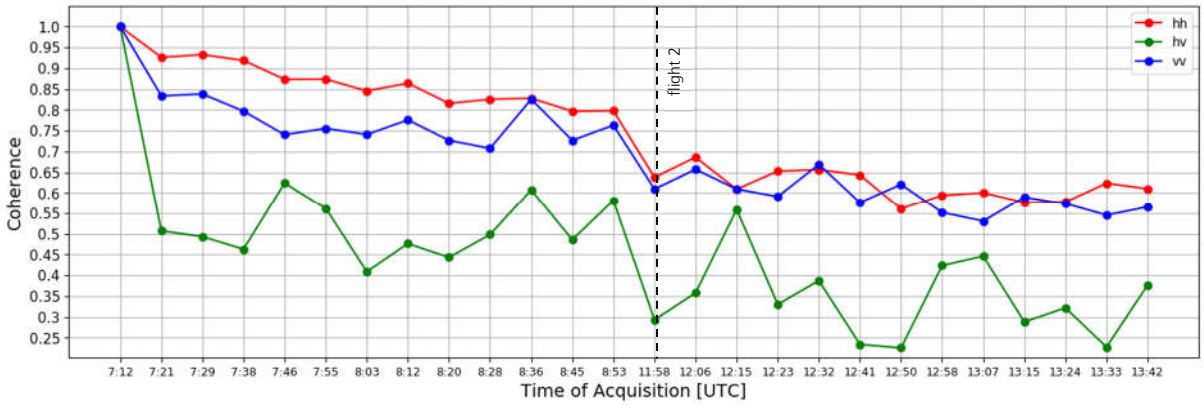

Figure 7.24: Coherence over time for Hydroterra parameters and survey point "B01" with first acquisition of first flight as master for the different polarimetric channels.

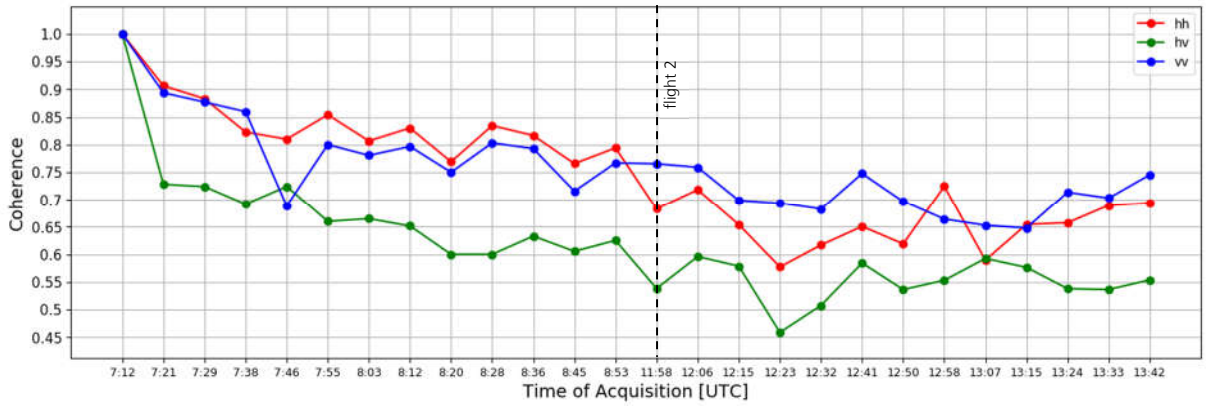

Figure 7.25: Coherence over time for Hydroterra parameters and survey point "B18" with first acquisition of first flight as master for the different polarimetric channels.

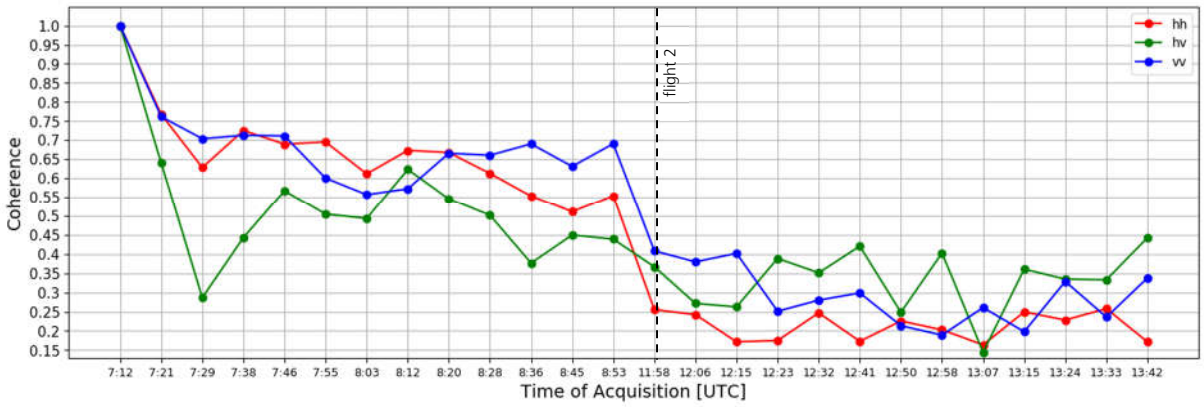

Figure 7.26: Coherence over time for Hydroterra parameters and survey point "B22" with first acquisition of first flight as master for the different polarimetric channels.

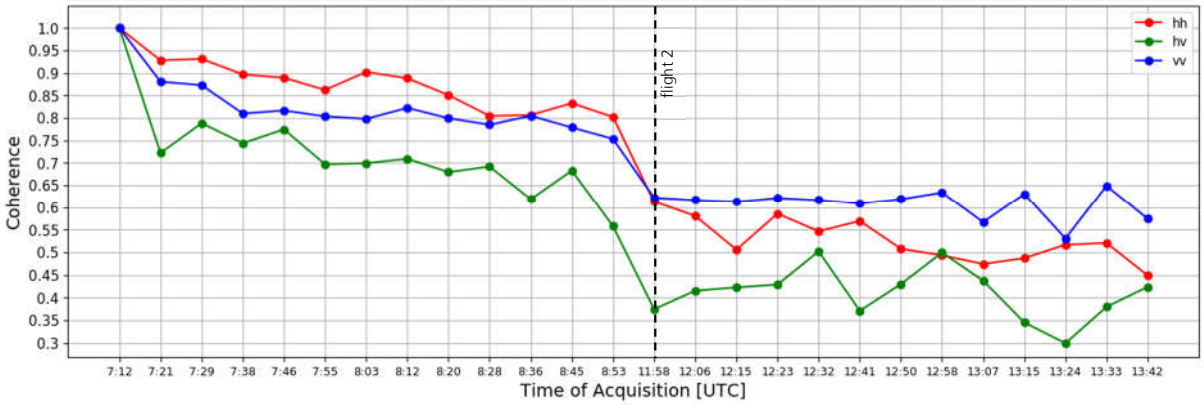

Figure 7.27: Coherence over time for Hydroterra parameters and survey point "A30" with first acquisition of first flight as master for the different polarimetric channels.

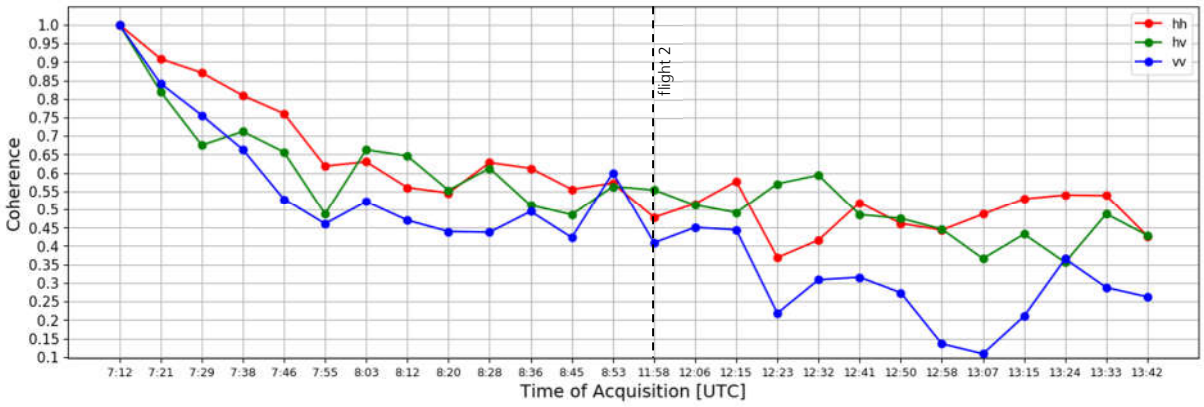

Figure 7.28: Coherence over time for Hydroterra parameters and survey point "B03" with first acquisition of first flight as master for the different polarimetric channels.

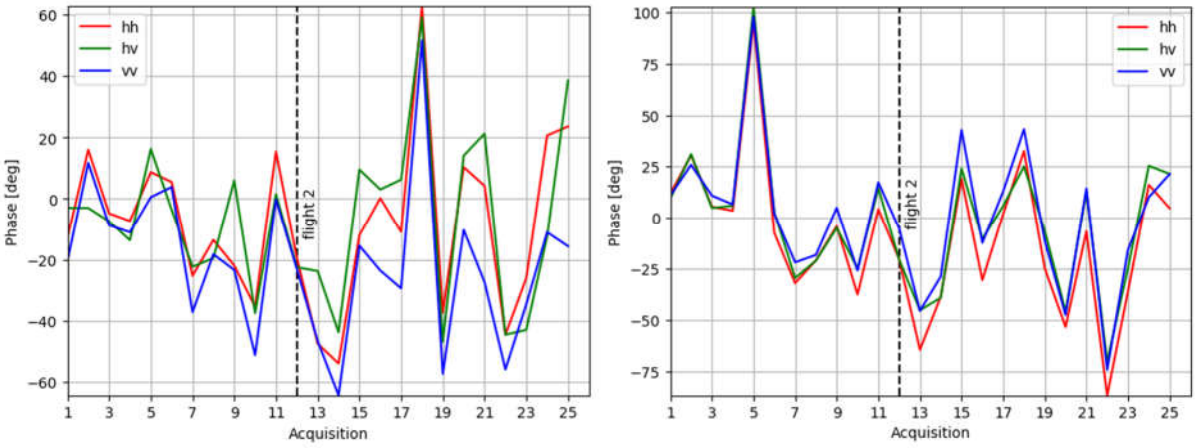

Figure 7.29: Interferometric phase for Hydroterra parameters with first acquisition of first flight as master for the different polarimetric channels. Left: For survey point "A16", right: For survey point "B01".

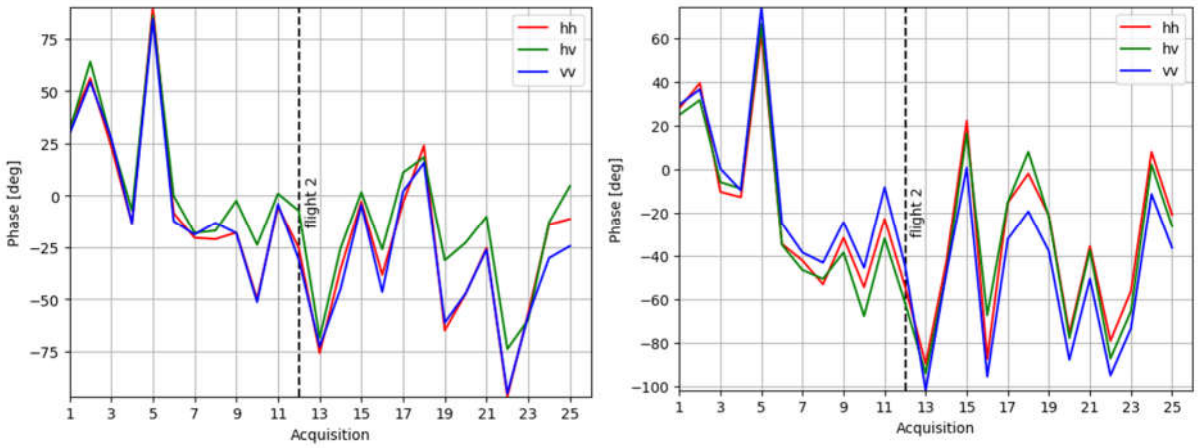

Figure 7.30: Interferometric phase for Hydroterra parameters with first acquisition of first flight as master for the different polarimetric channels. Left: For survey point "B18", right: For survey point "B22".

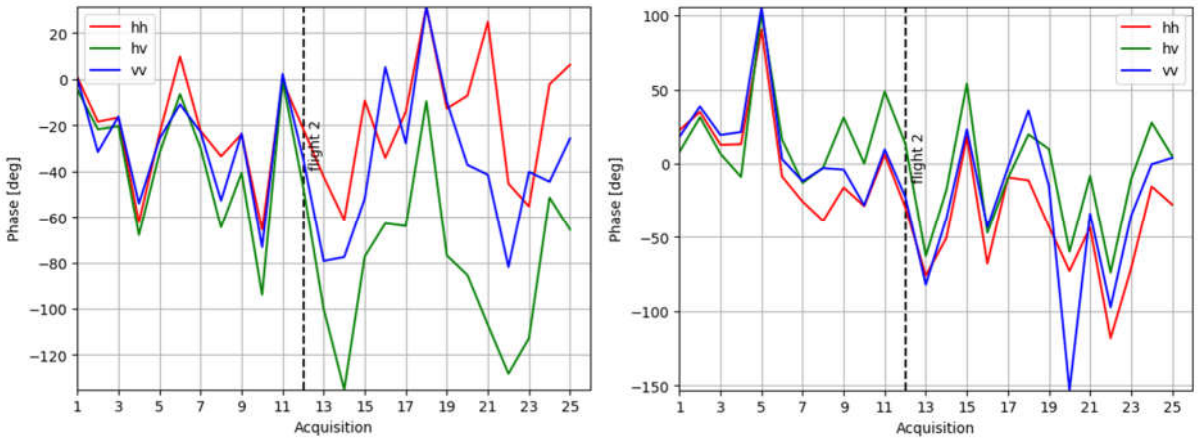

Figure 7.31: Interferometric phase for Hydroterra parameters with first acquisition of first flight as master for the different polarimetric channels. Left: For survey point "A30", right: For survey point "B03".

8 Phase Triplets Analysis

In this chapter phase triplets, as described in [9] and [10], were calculated and analysed. The idea of computing phase triplets is to evaluate whether the closure phase, i.e., the phase of the three multi-looked interferograms that can be generated with three images, is zero or not. In the presence of different scatterings mechanisms in the same resolution cell with different amplitude and phase behaviours, phase inconsistencies arise. As shown in the literature, this phase inconsistency can be related to soil or vegetation moisture changes. The evaluation of phase triplets in this study is conducted due to their potential to detect diurnal changes of land surface parameters while being immune to phase calibration. Note that phase inconsistencies also arise in SAR tomography in the presence of semi-transparent media and the change of the tomographic baselines.

Figure 8.1 shows the closure phase between the first and last acquisition of the first flight and the last acquisition of the second flight, overlaid with the amplitude image. Here the whole test site is shown for the HH polarisation. The colour range of the images varies between -30° and +30°. The left side of Figure 8.1 shows the closure phase of the F-SAR data while the right side displays the closure phase of the Hydroterra simulated time series with SSM Agro parameters. To analyse the closure phase, spatial averaging has to be performed. Here for both data sets first a moving average filter of 10 x 10 pixels was applied, followed by the application of a moving average filter with 2 x 2 pixels two additional times in order to improve the spatial and frequency resolution of the filter.

For the F-SAR data closure phases which are unequal to zero are visible at several positions. Also, a clear correlation between closure phase signals and fields can be seen in this image. This is especially evident on the top right side of the image under the forested area and on the bottom left side of the image under the lake. These phase inconsistencies are most probably an indication of moisture changes, be it in the ground or in the vegetation.

Also, at several different field positions non-zero closure phases are visible for the simulated Hydroterra time series data. Several fields can be identified which have a closure phase signal for the F-SAR data as well as for the simulated Hydroterra time series data. One example is the field under the forested area on the right top side of both images. Another example are the fields under the lake on the left side and also on the bottom left side of both images. However, unfortunately it is more difficult to identify the different fields in the simulated Hydroterra time series data than in the F-SAR data; due to the coarser spatial resolution. To analyse the closure phase a significant amount of spatial averaging has to be performed to mitigate the noise enough in order to properly observe the physical signal, as described in [11]. But due to the coarser resolution of the simulated Hydroterra time series data and due to the small size of the fields in the test site, the amount of samples to be averaged for each individual field is very limited. Therefore, after spatial averaging the signal of the fields is mixed with signals of their surroundings. One can therefore conclude that the final performance of the Hydroterra mission in the retrieval of diurnal changes of land surface parameters exploiting phase triplets will finally depend on the size of the region of interest.

In Chapter 8.1 a phase triplets analysis of the six survey points which are described in Chapter 4, is performed. Due to the small size of the fields, this analysis is only carried out for F-SAR data.

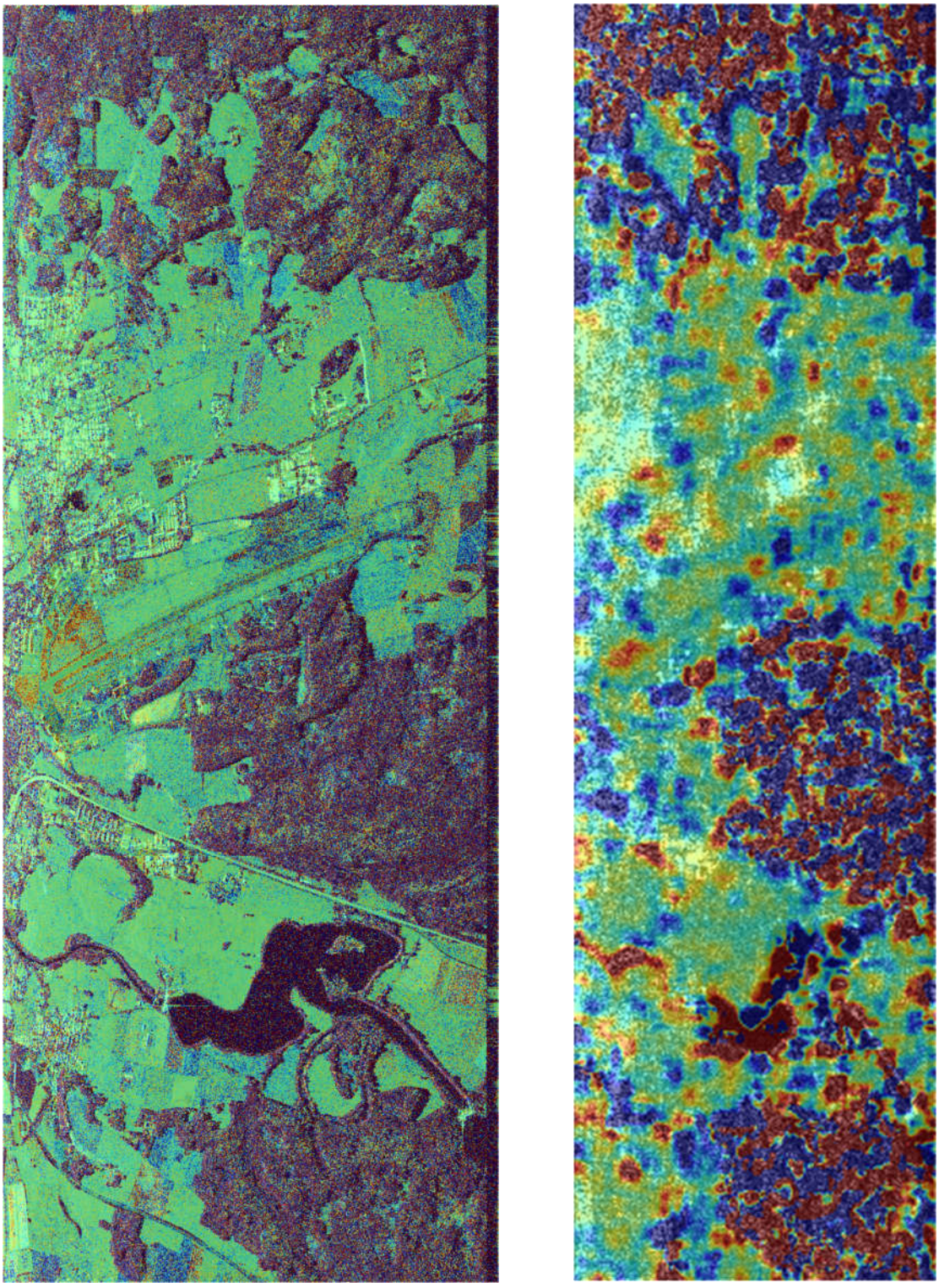

Figure 8.1: Left: Closure phase overlaid with amplitude image of F-SAR data for HH polarisation. The colour scale is ± 30°. Right: Closure phase overlaid with amplitude image of simulated Hydroterra data with SSM Agro parameters for HH polarisation. The colour scale is ± 30°.

8.1 Phase Triplets Analysis of F-SAR Data

Figures 8.1.1-8.1.6 show the closure phases which were evaluated at the six survey points, which are described in Chapter 4. The left side of Figures 8.1.1-8.1.6 shows the closure phase between the first and last acquisition of the first flight and the last acquisition of the second flight. Here a spatial averaging of 10 x 10 pixels was performed. The colour scale of these images varies from -30° to +30° and the polarization is HH. The red rectangle in these images shows the area over which the closure phase is averaged for the images on the right side of Figures 8.1.1-8.1.6. Here several closure phases are evaluated between three images: the first acquisition of the first flight, the last acquisition of the second flight, and a third image is represented in the x-axis. The closure phase is evaluated for all polarisations.

Figure 8.1.1 shows the closure phase of the survey point "A16". On the left side of this figure, a strong signal of the closure phase is visible. However, the values of the closure phase vary between positive and negative values, therefore the averaged closure phase inside the rectangle, which is shown on the left side of Figure 8.1.1, appears to be lower than it actually is. At the survey point "A16" corn with a height of 1.90 m was growing during the data acquisition. It is therefore unclear if the signal of the closure phase is due to moisture or due to volume scattering. The right side of Figure 8.1.1 shows no difference of the closure phase for different polarisations.

The closure phase at the survey point "B01" can be seen in Figure 8.1.2. Both images of Figure 8.1.2 show that the signal of the closure phase is very small for this survey point. For this field there are no differences between the different polarisations.

The left side of Figure 8.1.3 shows the signal of the closure phase of the survey point "B18". The closure phase is non-zero, but the signal is not very large. The values inside the rectangle vary between positive and negative values. The right side of Figure 8.1.3 shows that the closure phase is higher for the HH and HV polarisations than for the VV polarisation for some evaluated acquisitions.

A strong signal of the closure phase is visible on the left side of Figure 8.1.4, where the closure phase around the survey point "B20" is displayed. The right side of this figure also shows high values for most acquisitions. The HV polarisation has the highest values.

Figure 8.1.5 shows the closure phase of the survey point "A30". The left side of Figure 8.1.5 displays that the closure phase has high values at the lower part of the red rectangle and less high values at the upper part of the rectangle. The position and extent of the rectangle was chosen to fit the field from the amplitude image. This rectangle is therefore inside the same field. The ground truth team observed how the field at the survey point "A30" was watered. Probably only one part of the field was watered during the data acquisition. The right side of Figure 8.1.5 shows that the HV polarisation has slightly different closure phases than the HH and VV polarisations.

Very high values are visible on the left side of Figure 8.1.6. Here the closure phase of the survey point "B03" is shown. The closure phase varies for this survey point between positive and negative values. The high signal is therefore less pronounced in the image on the right side. This evaluation shows, however, that for some acquisitions the closure phase of the VV polarisation has higher values.

Due to the lack of ground-truth it is not possible to draw any particular conclusion to the results obtained with the current data set. Also, for this same reason no inversion of moisture was per-

formed. However, given the baselines of the acquisitions are small, it can be stated that the effects being observed are most probably related to changes in soil moisture either of the soil or of the vegetation.

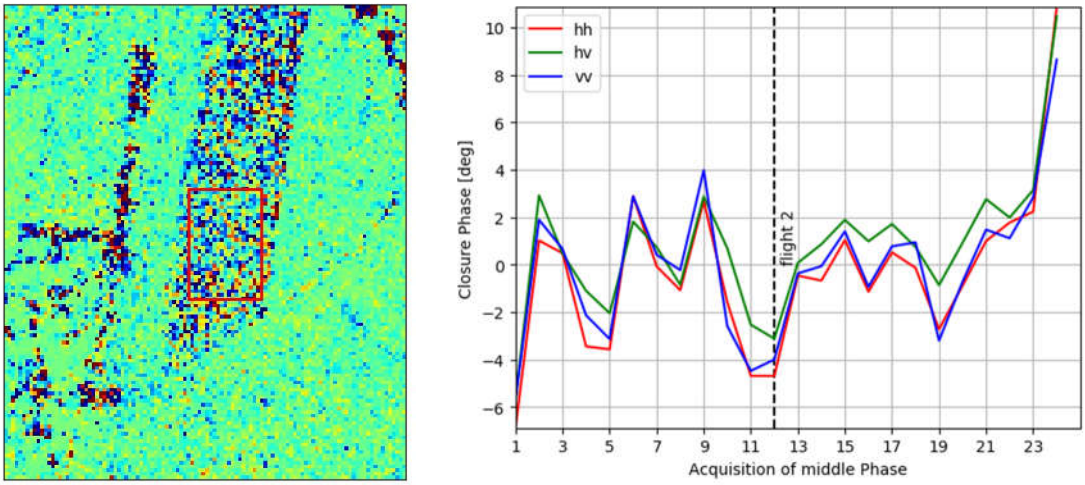

Figure 8.1.1: Left: Closure phase between first and last acquisition of first flight and last acquisition of second flight for HH polarisation of survey point "A16". The colour scale is ± 30° and spatial averaging of 10 x 10 pixels was performed. Right: Averaged closure phase inside red rectangle from the left figure for the different polarizations between the first acquisition of the first flight, the last acquisition of the second flight and one varying acquisition.

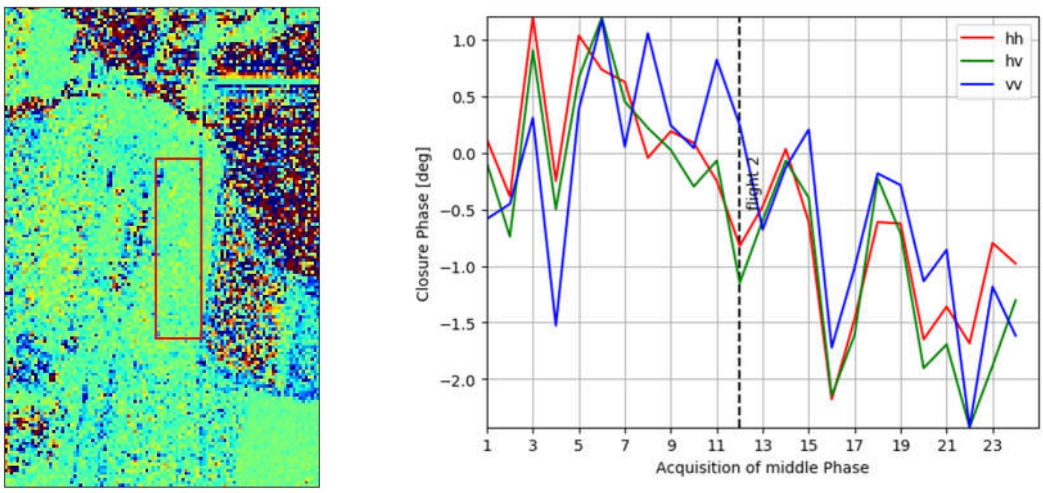

Figure 8.1.2: Left: Closure phase between first and last acquisition of first flight and last acquisition of second flight for HH polarisation of survey point "B01". The colour scale is ± 30° and spatial averaging of 10 x 10 pixels was performed. Right: Averaged closure phase inside red rectangle from the left figure for the different polarizations between the first acquisition of the first flight, the last acquisition of the second flight and one varying acquisition.

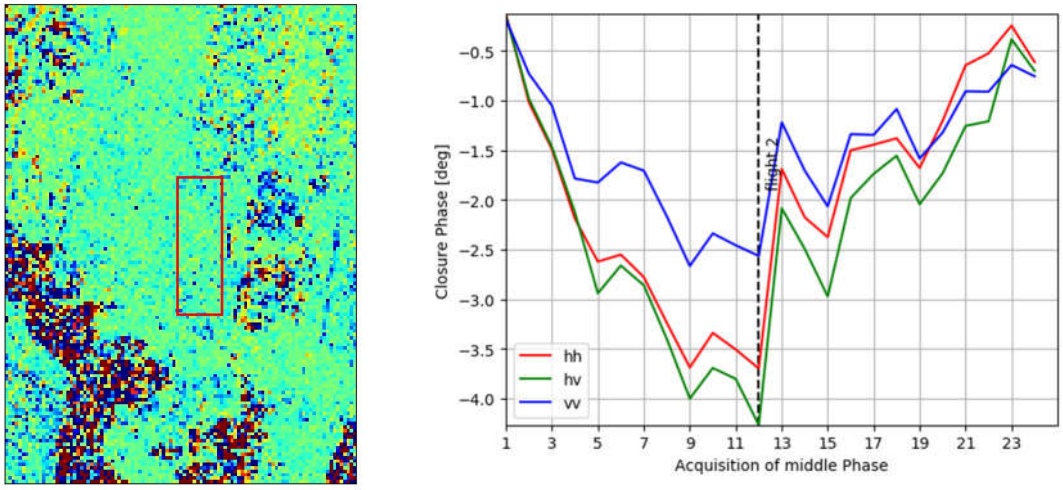

Figure 8.1.3: Left: Closure phase between first and last acquisition of first flight and last acquisition of second flight for HH polarisation of survey point "B18". The colour scale is ± 30° and spatial averaging of 10 x 10 pixels was performed. Right: Averaged closure phase inside red rectangle from the left figure for the different polarizations between the first acquisition of the first flight, the last acquisition of the second flight and one varying acquisition.

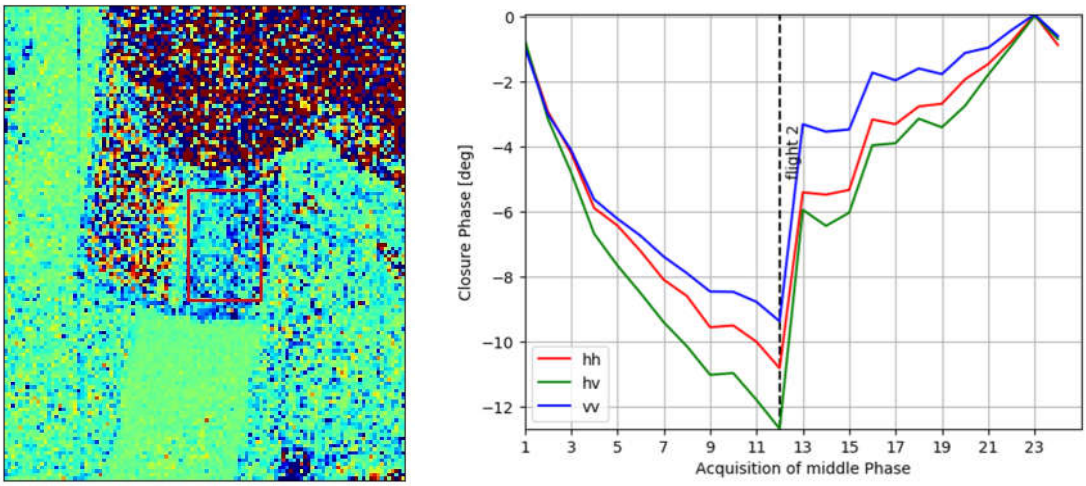

Figure 8.1.4: Left: Closure phase between first and last acquisition of first flight and last acquisition of second flight for HH polarisation of survey point "B22". The colour scale is ± 30° and spatial averaging of 10 x 10 pixels was performed. Right: Averaged closure phase inside red rectangle from the left figure for the different polarizations between the first acquisition of the first flight, the last acquisition of the second flight and one varying acquisition.

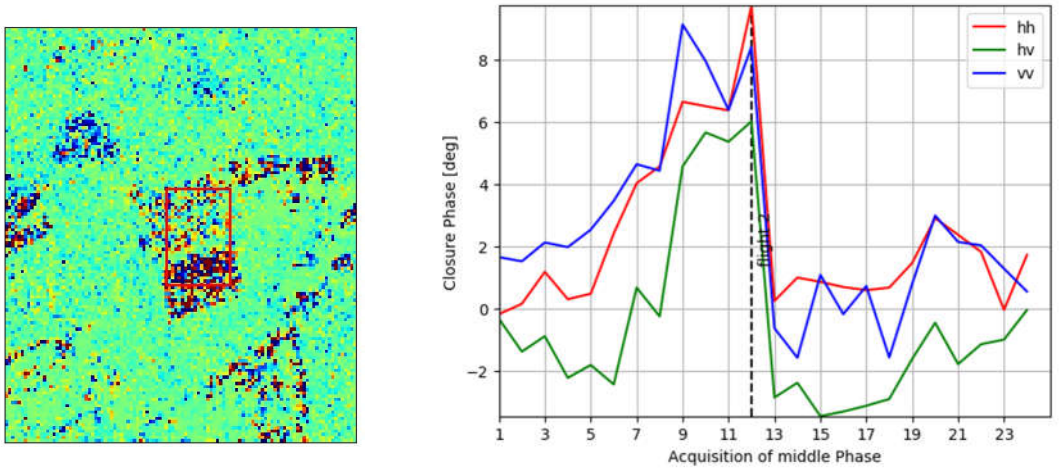

Figure 8.1.5: Left: Closure phase between first and last acquisition of first flight and last acquisition of second flight for HH polarisation of survey point "A30". The colour scale is ± 30° and spatial averaging of 10 x 10 pixels was performed. Right: Averaged closure phase inside red rectangle from the left figure for the different polarizations between the first acquisition of the first flight, the last acquisition of the second flight and one varying acquisition.

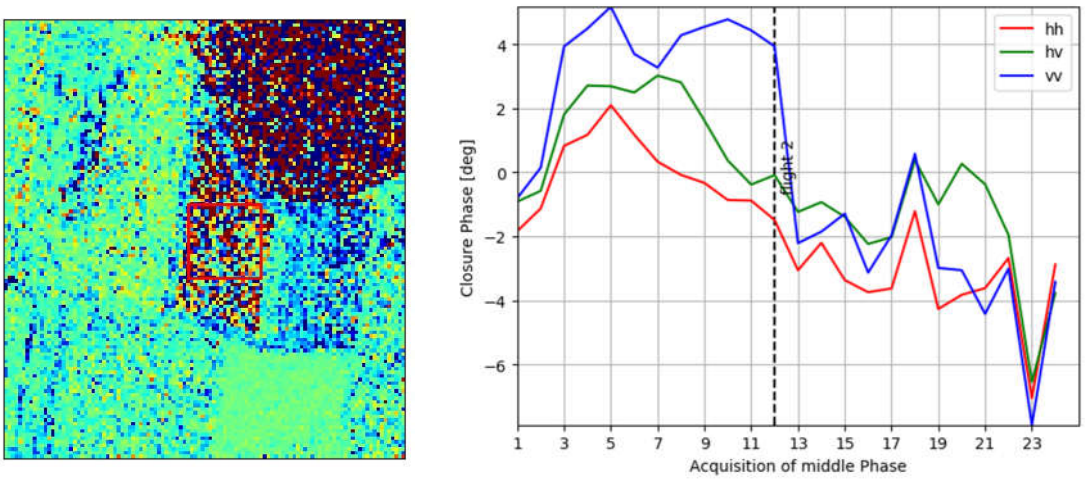

Figure 8.1.6: Left: Closure phase between first and last acquisition of first flight and last acquisition of second flight for HH polarisation of survey point "B03". The colour scale is ± 30° and spatial averaging of 10 x 10 pixels was performed. Right: Averaged closure phase inside red rectangle from the left figure for the different polarizations between the first acquisition of the first flight, the last acquisition of the second flight and one varying acquisition.

9 Hydroterra Images with different Wind Conditions

9.1 Wind-Blown Clutter Simulation Procedure

This chapter describes how Hydroterra data are simulated incorporating wind-blown clutter from high vegetation. The input to this simulation are the 2 simulated Hydroterra products, generated from each of the 2 F-SAR flights from the 2019 campaign over Kaufbeuren airfield, as described in [3] and Chapter 3 of this report. The F-SAR airborne campaign is described in more detail in [1].

The simulation of wind-blown clutter is based on the model derived from BOREALSCAT measurements conducted in Sweden over boreal forest using a tower-based C-band radar sensor with incidence angles comparable to the one of Hydroterra [12]. This radar system also operates in P- and L-band

The wind-blown clutter simulation uses the following basic operations.

- Generation of a most realistic vegetation mask, to identify regions to be defocused.
- Computation of phase distortion vectors to be applied to the before identified regions.
- Simulation of the wind-blown clutter distorted images, with different parameterisation, according to wind speed and polarisation.

These steps are described in detail in the following sections.

9.1.1 Vegetation mask

The vegetation mask is derived from the high resolution, fully polarimetric F-SAR data acquired during the flight campaign. First, an entropy-alpha decomposition of the polarimetric data has been performed, providing 8 classes. Four classes were jointly identified as being representative of forest areas and higher vegetation. In a second step, also the interferometric coherence between the first two passes of flight 1 was used. Only those areas where the repeat-pass coherence of the VV polarisation is below 0.75 were selected for the final vegetation mask. Morphological closing and opening operators were employed to ensure a more homogeneous, planar vegetation cover, as depicted in Figure 9.1.

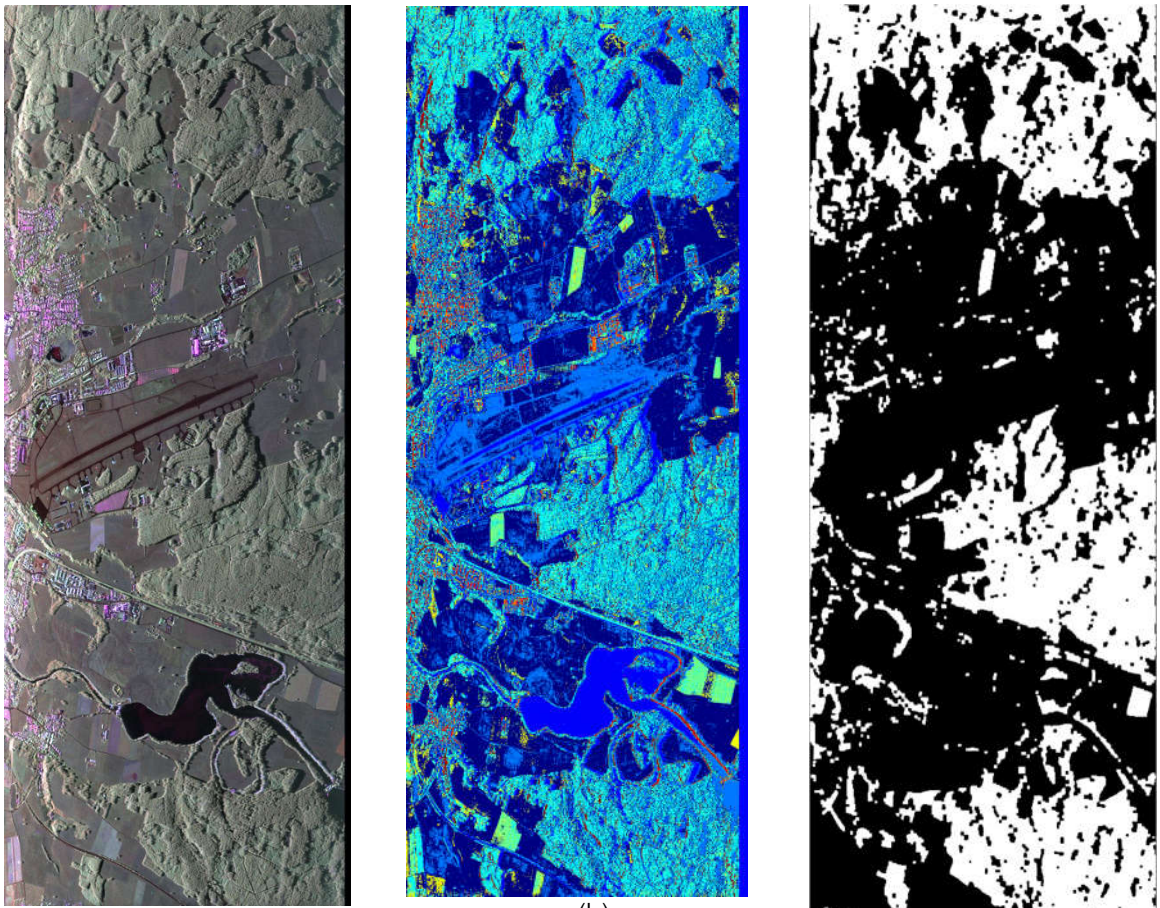

(a) (b) (c)

Figure 9.1: (a) F-SAR full resolution polarimetric data used as input for the derivation of the vegetation mask. (b) Entropy-alpha classification. (c) Vegetation mask.

9.1.1.1 BOREALSCAT model

The BOREALSCAT model is an adaptation of Billingeley's wind clutter model [12]. In both cases the total power spectral density is described as a combination of a stable scattering component (Dirac at zero Doppler frequency/wind speed) and a model for the statistical part.

$$P_t(v) = \frac{r}{r+1}\delta(v) + \frac{1}{r+1}P_{ac}(v) \tag{9.1-1}$$

The power ratio r of the direct component (DC) to the alternating component (AC) is a function of wind speed w and polarisation. BOREALSCAT proposed the following dependencies, which are slightly different than the ones of the original Billingeley model:

$$10\,log_{10}\,r = -15.5\,log_{10}\frac{w}{0.447} - 12.1\,log_{10}\,f_0 + 61.2 \tag{9.1-2}$$

$$10\,log_{10}\,r = -15.5\,log_{10}\frac{w}{0.447} - 12.1\,log_{10}\,f_0 + 60.2 \tag{9.1-3}$$

The first equation is for the co-polar case and the second one for the cross-polar one. (In [12], pg. 38 the equations are reversed, but looking at Fig. 30 of that same report, it is clear, that the co-polarized ratio must be higher than the cross-polarised one, which is also intuitive, since co-polarised echoes are expected from the more stable parts of the trees.)

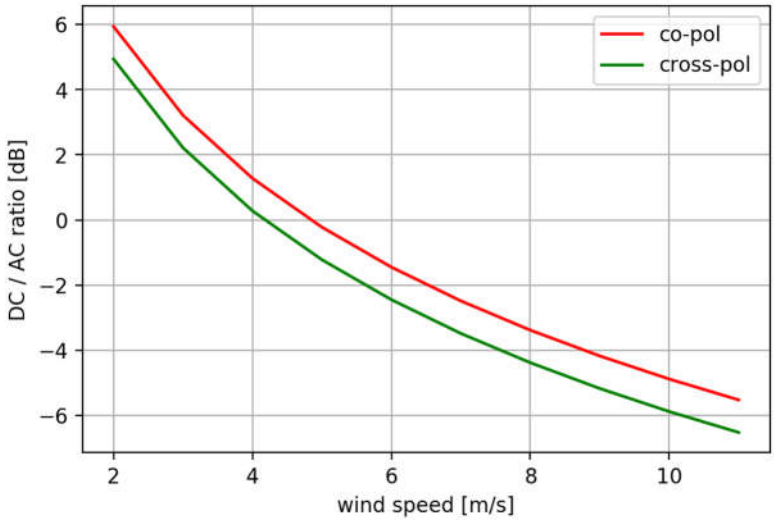

Figure 9.2: DC/AC ratio for different wind speeds. For co-polarised data, the power of the wind clutter equals the one of the stationary energy at 5m/s (DC/AC = 0dB). For cross-pol data, more relative energy contributes to wind clutter.

BOREALSCAT measurements also showed that a power law model is more suitable and better describes the measurements than the originally proposed exponential model. For simulating the wind-clutter effect, we therefore use the suggested model from [12] (pg. 37, Table 2.1) for $P_{av}(v)$.

Polarisation	**Parameters for power law(*):** $P_{ac}(v) = \frac{n\sin\left(\frac{\pi}{n}\right)}{2\pi v_c} \cdot \frac{1}{1+\left(\frac{\lvert v\rvert}{v_c}\right)^n}$
HH	$n = 0.14w + 1.25$ $v_c = 0.0024w - 0.01$
VV	$n = 0.14w + 1.3$ $v_c = 0.0027w - 0.01$
HV	$n = 2$ $v_c = 0.0018w - 0.005$

Table 9.1: Power law model for the AC component of the power spectral density [12]. The parameters of the model (n and v_c) are a function of wind speed w.

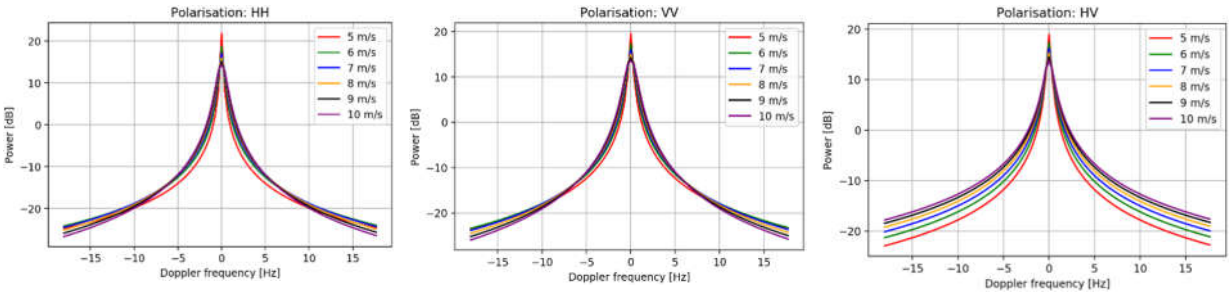

Figure 9.3: Power spectral densities according to BOREALSCAT model of Table 9.1.

The AC model component is used to generate statistical realisations of Doppler phase distortion vectors, which are then superimposed to the SAR data in addition to the ideal Doppler modulation due to sensor target range difference. For processing reasons, the length/temporal extend of the vector slightly exceeds the synthetic aperture of Hydroterra, comprising all looks of a product.

An example of such a distortion phase is given in Figure 9.4 below.

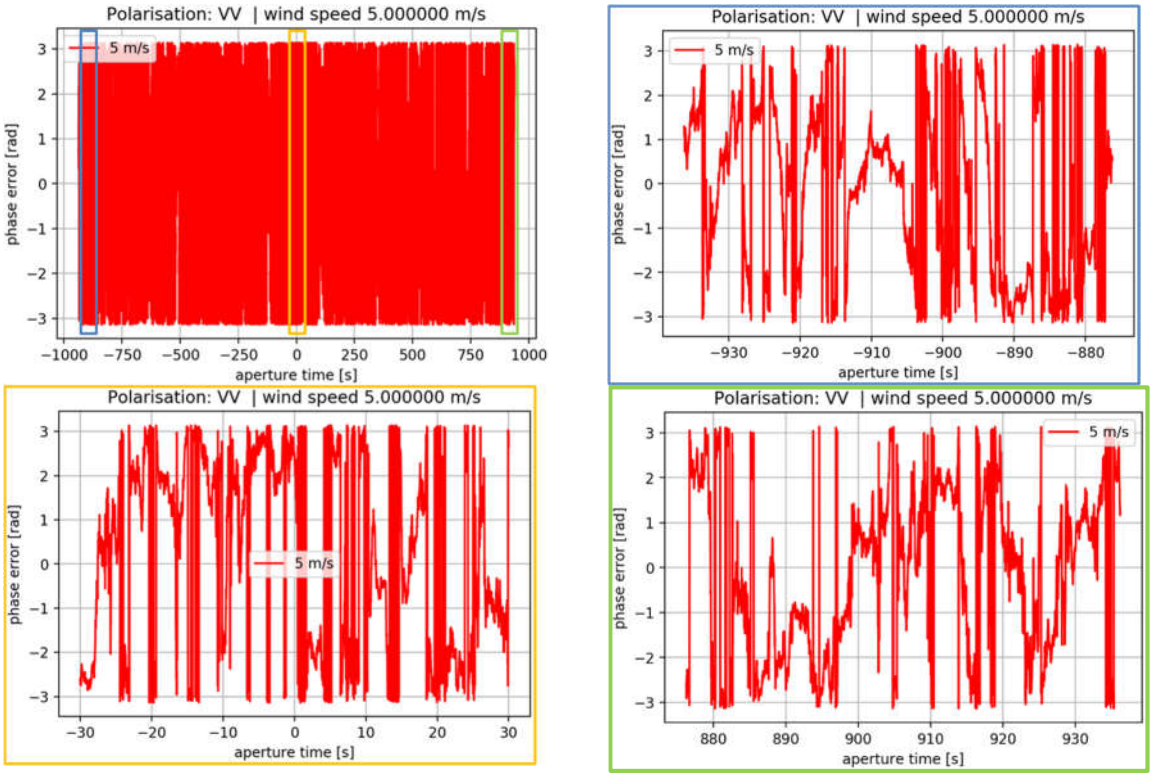

Figure 9.4: Realisation of a Doppler phase distortion according to the power law model of Table 9.1 for a wind speed of 5 m/s and VV polarisation (full length of synthetic aperture and 3 zooms).

9.1.1.2 Simulation approach

For demonstration purposes, the simulation approach for wind clutter defocusing of Hydroterra SAR data is first implemented for a single point target. It is then generalized for simulating a full scene taking into account the vegetation mask derived above.

9.1.1.2.1 Single point target simulation

The generation of the azimuth chirp, the application of the wind distortion phase and the subsequent focusing are performed according to the block diagram in Figure 9.5. In the diagram on the left, the complete energy is defocused, whereas on right only a fraction according to the DC/AC ratio is defocused.

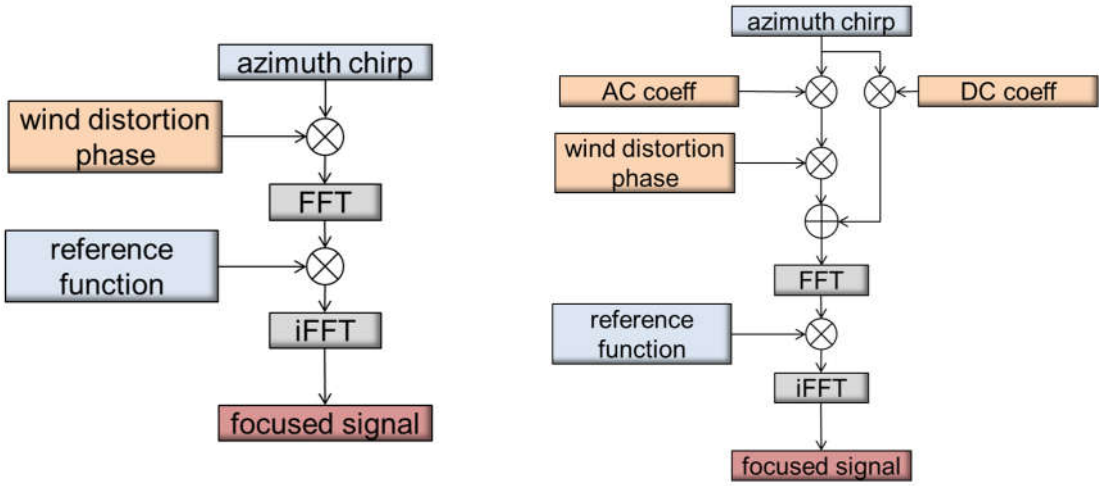

(a) (b)

Figure 9.5: Implementation of wind distortion for a single azimuth chirp for the AC case and for a finite DC/AC ratio.

The resulting distorted IRF functions are shown in Fig 9.5 in red vs. their ideal counterparts in green. Depending on the DC/AC ratio, all or a considerable part of the energy is spread over the lengths of the complete raw data signal.

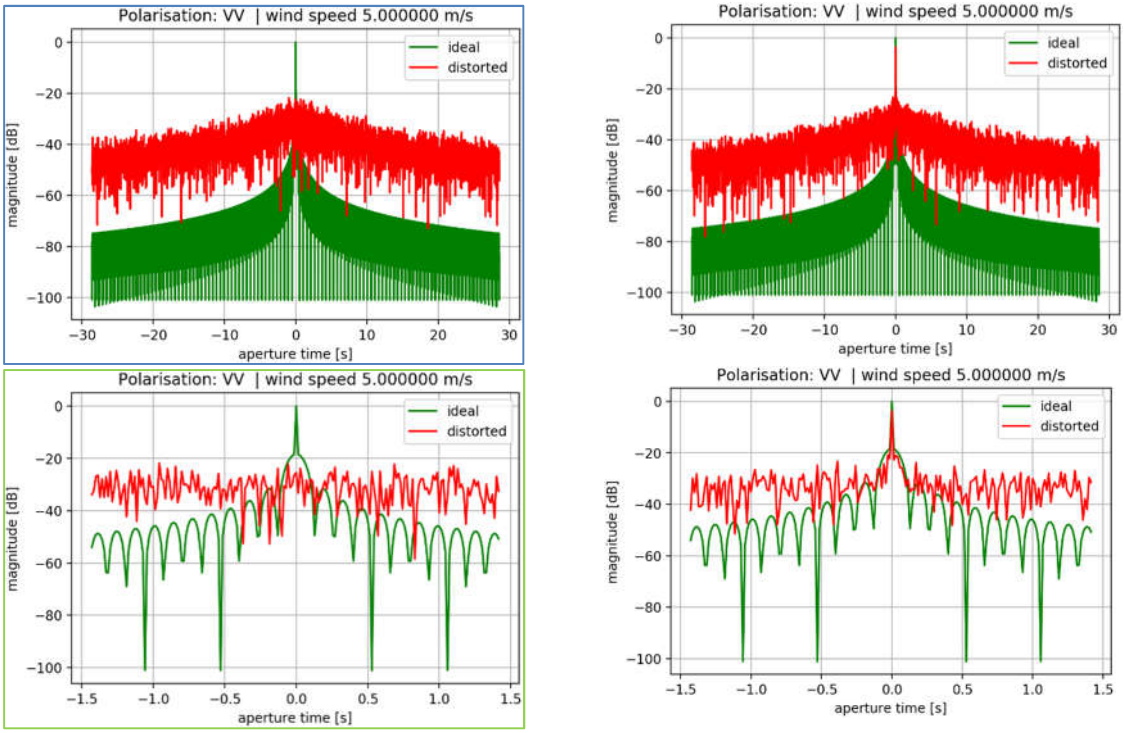

Figure 9.6: IRF for the two simulation cases of Figure 9.5. On the right, the DC/AC ratio was 0dB.

Although, the relative power (sidelobe energy) of the defocused signal appears rather low, it must be noted that in a real scenario, the defocused energies of a plenty of targets overlay, which can cause a considerable increase of apparent noise.

9.1.1.2.2 Complete scene simulation

For simulating a complete scene, only the fractional area contributing to wind clutter needs to be considered. The stationary parts of the scene will not be defocused. However, they will be affected by the defocused energy of the vegetated areas, which causes a decrease of the apparent SNR of the data and/or, to a less apparent extent, an increase of the observed backscatter for low reflectivity areas. The simulation is conducted according to the block diagram in Figure 9.7.

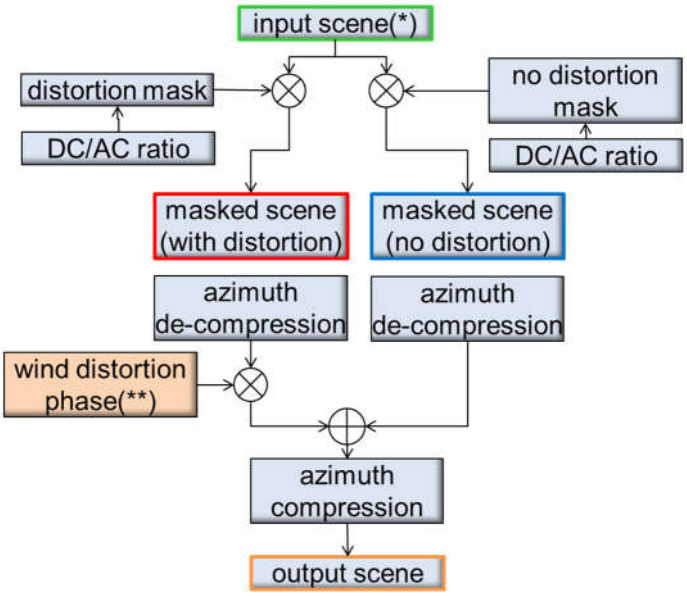

Figure 9.7: Simulation flow for the defocusing of vegetated scene content as a function of wind speed. The distortion mask is the one from Fig. 9.1.

The wind distortion phase is recomputed for each range sample and several realisations are used along azimuth and applied randomly to avoid correlated noise.

9.1.1.3 Wind simulation products

The wind simulation is applied to all polarisations of the two simulated Hydroterra products, corresponding to morning and afternoon data acquisitions of the F-SAR campaign.

The simulation is repeated for wind speeds from 2 m/s up to 10 m/s. The DC/AC ratio is steadily decreased according to eq. (9.1-2) and (9.1-3) as going from low wind speeds to the higher ones. However, the minimum wind speed for the AC component was set to 4.2 m/s, 3.5 m/s and 2.8 m/s (for HH, VV and HV polarisations), since the BOREALSCAT model is not well defined for low wind speeds, probably due to the lack of data. This means, the simulation results for the low wind speeds of 2 and 3 m/s are rather conservative in the sense that the defocusing amount is potentially exaggerated but not the amount of defocused energy.

For demonstration purposes, the simulation results for VV polarisation are presented for the wind speeds of 3 m/s and 6 m/s in Figure 9.9 and Figure 9.10 respectively. For ease of assessment, the original input image, the applied vegetation mask and its average profile along the range direction are shown in Figure 9.8.

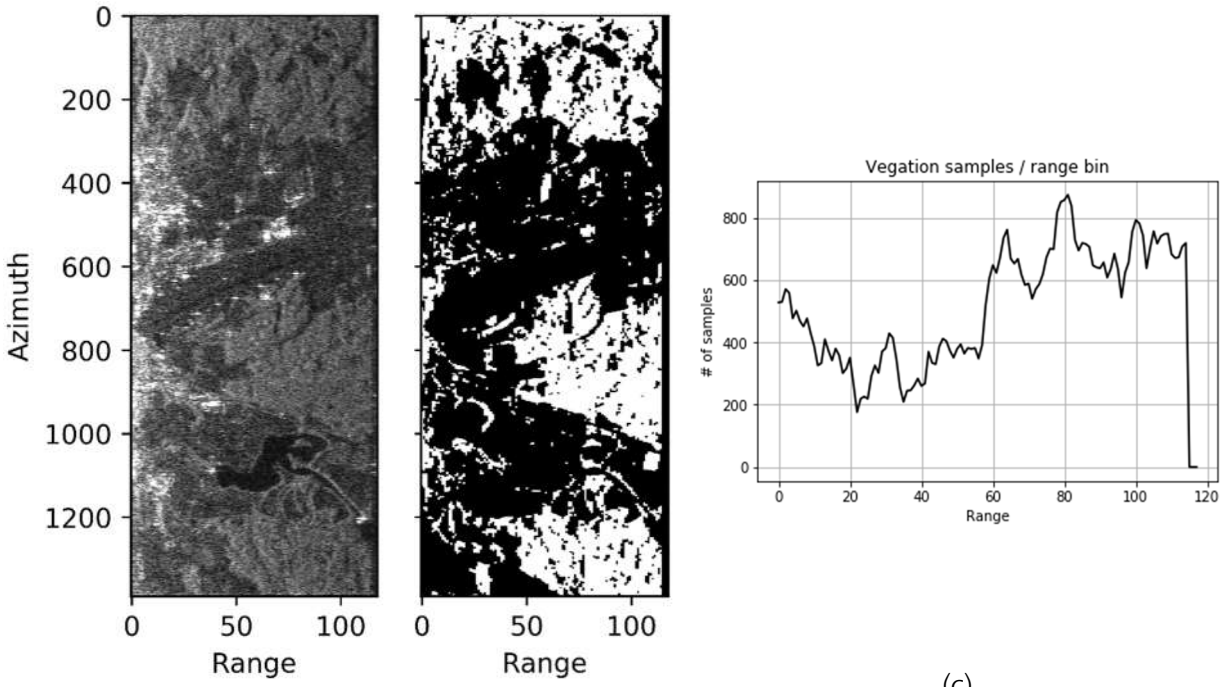

Figure 9.8: Original undistorted Hydroterra image (a), the applied distortion/vegetation mask (b) and its accumulated range profile (c).

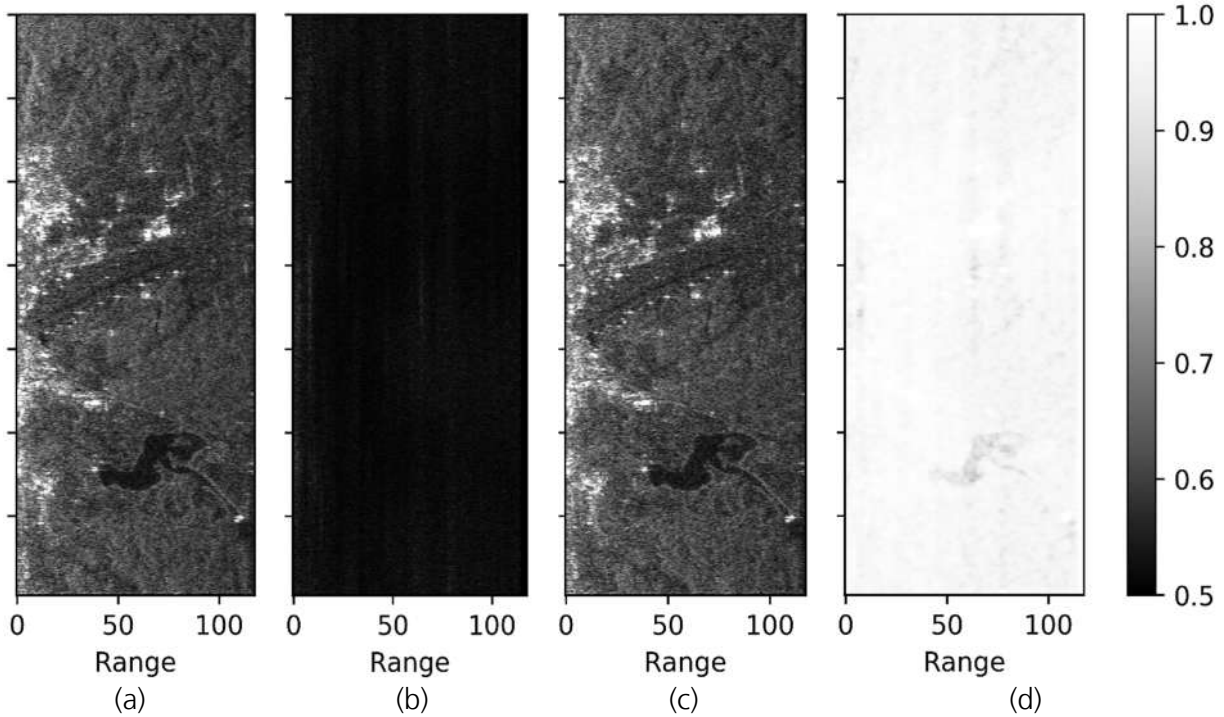

Figure 9.9: Distorted Hydroterra images for a wind speed of 3 m/s: Stable image component (a), defocused image component (b), the distorted image (sum of (a) and (b)) (c), coherence with respect to undistorted image in Figure 9.8 (a).

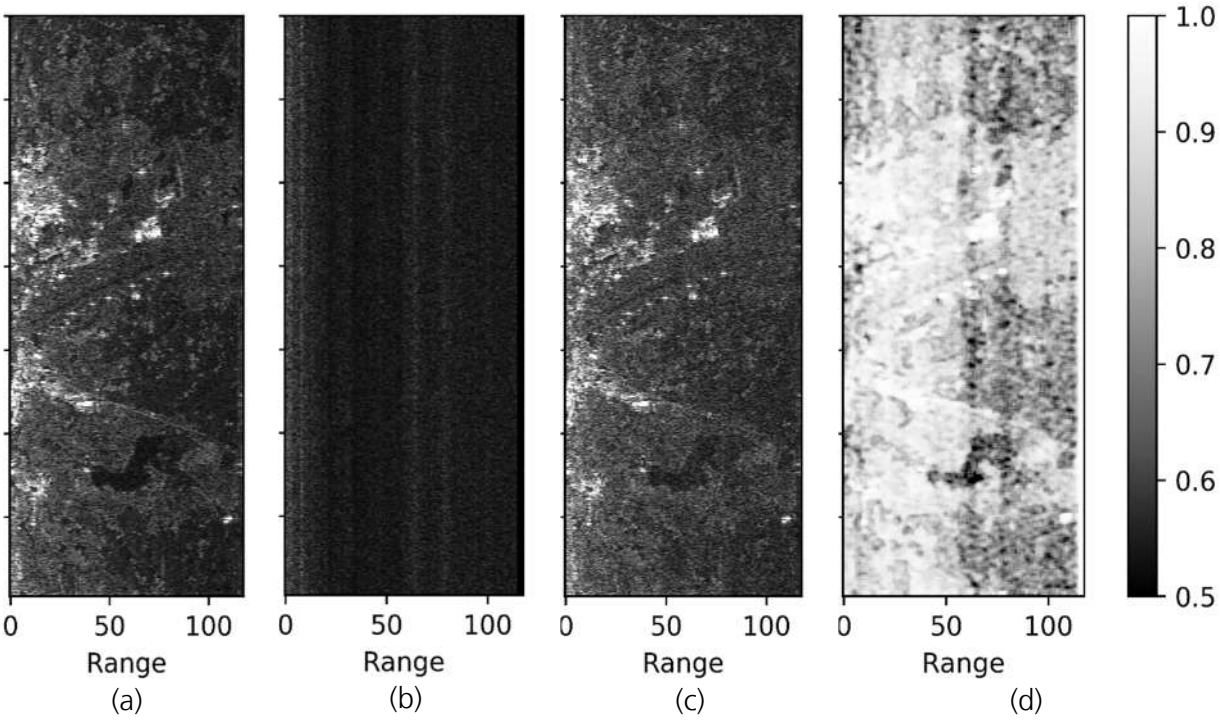

Figure 9.10: Distorted Hydroterra images for a wind speed of 6 m/s: Stable image component (a), defocused image component (b), the distorted image (sum of (a) and (b)) (c), coherence with respect to undistorted image in Figure 9.8 (a).

Some observations:

1. In areas of vegetation (forest), a decay of the backscatter can be observed with increasing wind speed. This can be seen in sub-figures (a) and (c) of Figure 9.9 and Figure 9.10.
2. This energy spreads over the complete image leading to an apparent increase of energy (wind-clutter or additional noise) in low vegetation / bare soil areas, as well as over water.
   This can be seen in sub-figures (b) and (c) of Figure 9.9 and Figure 9.10.
3. There is a considerable decrease of coherence with increasing wind speed, especially in forest areas, but also over bare soil. See sub-figures (d) of Figure 9.9 and Figure 9.10.

The quantitative impact of the wind clutter is analysed in the next section for different areas of the image.

9.1.1.4 Quantitative evaluations

9.1.1.4.1 General impact on coherence

The overall impact on the coherence of a scene is summarized in the 3 tables below. In addition to the overall impact, it is distinguished between vegetated and non-vegetated areas as indicated by the forest mask in Figure 9.1. Tables 9.2 to 9.4 summarize the coherence values between the wind distorted images and the original input image to the wind clutter simulation of Figure 9.7 for different polarisations and wind speeds.

Wind Speed	2.0 [m/s]	3.0 [m/s]	4.0 [m/s]	5.0 [m/s]	6.0 [m/s]	7.0 [m/s]	8.0 [m/s]	9.0 [m/s]	10.0 [m/s]
HH	0.994	0.975	0.940	0.895	0.848	0.803	0.764	0.731	0.705
VV	0.994	0.974	0.936	0.891	0.841	0.794	0.754	0.720	0.720
HV	0.991	0.961	0.916	0.862	0.811	0.766	0.730	0.701	0.679

Table 9.2: Wind induced coherence with respect to the original undistorted image for the complete scene.

Wind Speed	2.0 [m/s]	3.0 [m/s]	4.0 [m/s]	5.0 [m/s]	6.0 [m/s]	7.0 [m/s]	8.0 [m/s]	9.0 [m/s]	10.0 [m/s]
HH	0.992	0.962	0.900	0.852	0.772	0.691	0.619	0.558	0.509
VV	0.992	0.966	0.920	0.855	0.772	0.691	0.618	0.556	0.506
HV	0.985	0.947	0.886	0.798	0.707	0.625	0.557	0.504	0.463

Table 9.3: Wind induced coherence with respect to the original undistorted image for the highly vegetated (forest) parts of the scene.

Wind Speed	2.0 [m/s]	3.0 [m/s]	4.0 [m/s]	5.0 [m/s]	6.0 [m/s]	7.0 [m/s]	8.0 [m/s]	9.0 [m/s]	10.0 [m/s]
HH	0.996	0.983	0.962	0.921	0.892	0.867	0.847	0.831	0.818
VV	0.994	0.978	0.946	0.912	0.881	0.854	0.832	0.815	0.801
HV	0.994	0.970	0.933	0.900	0.871	0.847	0.829	0.815	0.804

Table 9.4: Wind induced coherence with respect to the original undistorted image for the sparsely vegetated (non-forest) parts of the scene.

These numbers can be used as input for quantifying the additional decorrelating coherence component due to wind in case of interferometric HT acquisitions. If e.g. only one image is affected by wind, the numbers can be taken directly from the table, whereas if both images are affected by wind, the wind decorrelation coherence component becomes the product of two table entries. E.g. for VV polarisation and wind speeds of 2 m/s and 5 m/s in the 2 acquisitions, the additional coherence factor will be 0.992*0.855 = 0.848 for the forest areas and 0.994*0.912 = 0.906 for non-forest areas.

9.1.1.4.2 Assessment for different land cover types

In this section we describe exemplarily the impact for different land cover types for which ground truth has been collected. The impact on scene backscatter and the decorrelation contribution are quantified. The displayed coherence plots are with respect to the input image.

Figure 9.11: Ground truth locations A30, B06, Urban-1 and Forest-2 used for quantitative analysis.

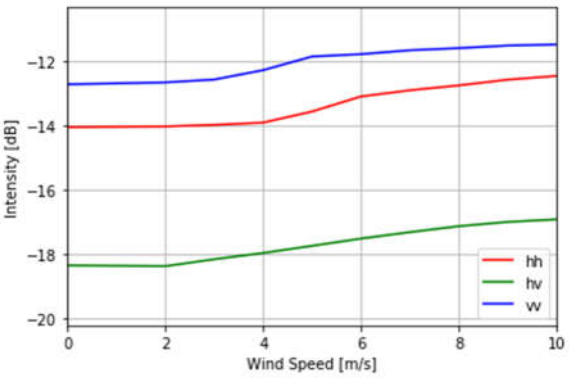

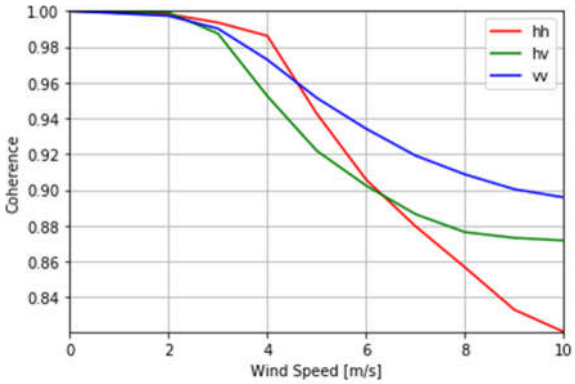

Figure 9.12: **A30 (short grass, 3 cm, watered):** The VV-polarisation dominates the backscatter. With increasing wind speed, the wind-blown energy from the forest areas (clutter noise) increases the apparent backscatter level. The coherence decays faster for lower backscatter.

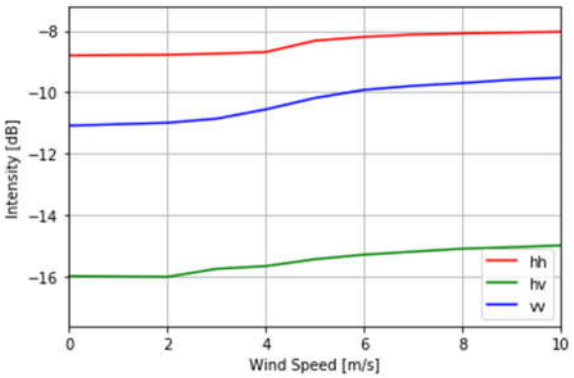

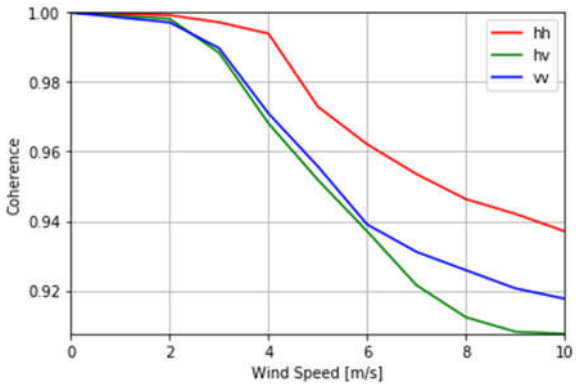

Figure 9.13: **B06 (wheat field):** The HH-polarisation dominates the backscatter (higher double bounce component). With increasing wind speed, the wind-blown energy from the forest areas (clutter noise) increases the apparent backscatter level. The coherence decays faster for lower backscatter.

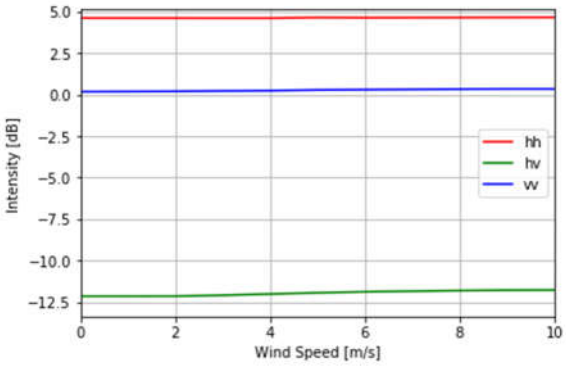

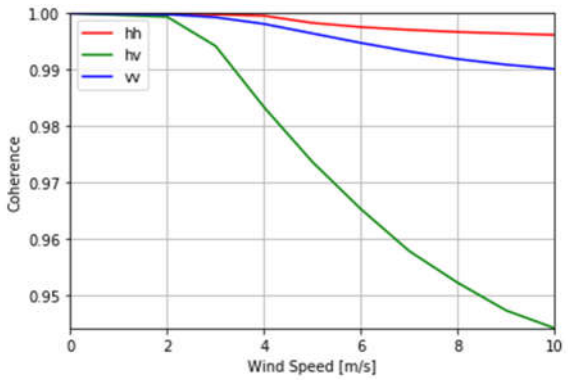

Figure 9.14: **Urban 1:** The VV-polarisation dominates the backscatter. With increasing wind speed, the wind-blown energy from the forest areas (clutter noise) increases the apparent backscatter level for HV polarisation. The coherence decays faster for lower backscatter.

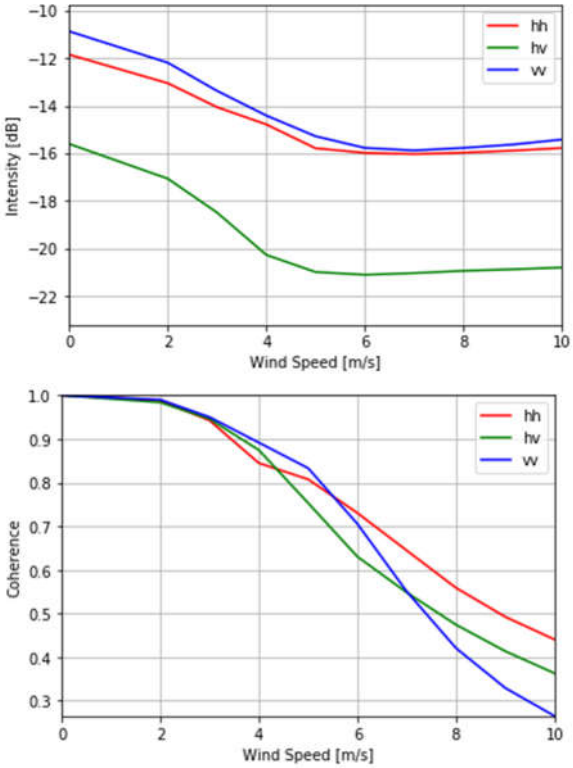

Figure 9.15: **Forest 2:** All polarisations suffer from a decay of measured backscatter, as wind-blown energy spreads over the complete scene. Due to defocusing, the coherence decays quickly for all polarisations.

9.1.1.4.3 Impact on interferometry between flights

The impact on interferometry between successive data acquisitions is presented in Figure 9.16 and Figure 9.17 exemplarily for 3 different wind conditions. In comparison with sub-figures (a), which present the undistorted case, the coherence is further decorrelating on the non-vegetated image parts. However, the dominant decorrelation source is temporal decorrelation, such that the wind effect is of secondary relevance, especially for wind speeds below 5 m/s. The effect on the interferometric phase is some additional phase noise and is even less visible, at least at the presented $\pm\pi$ scale.

The impact is further quantified for the 4 different land cover types shown in the previous section.
The non-vegetated test sites are characterized by a certain amount of interferometric coherence which is not much affected by wind clutter up to 3-4 m/s. For these low wind speeds also the interferometric phase of the co-polar interferograms is hardly affected. With further increasing wind speed the interferometric coherence starts to become affected and also the mean phase can be biased (except the urban scenario). On the contrary, the forested area is already strongly decorrelated and the additional effect of wind has no consequence on the interferometric observables.

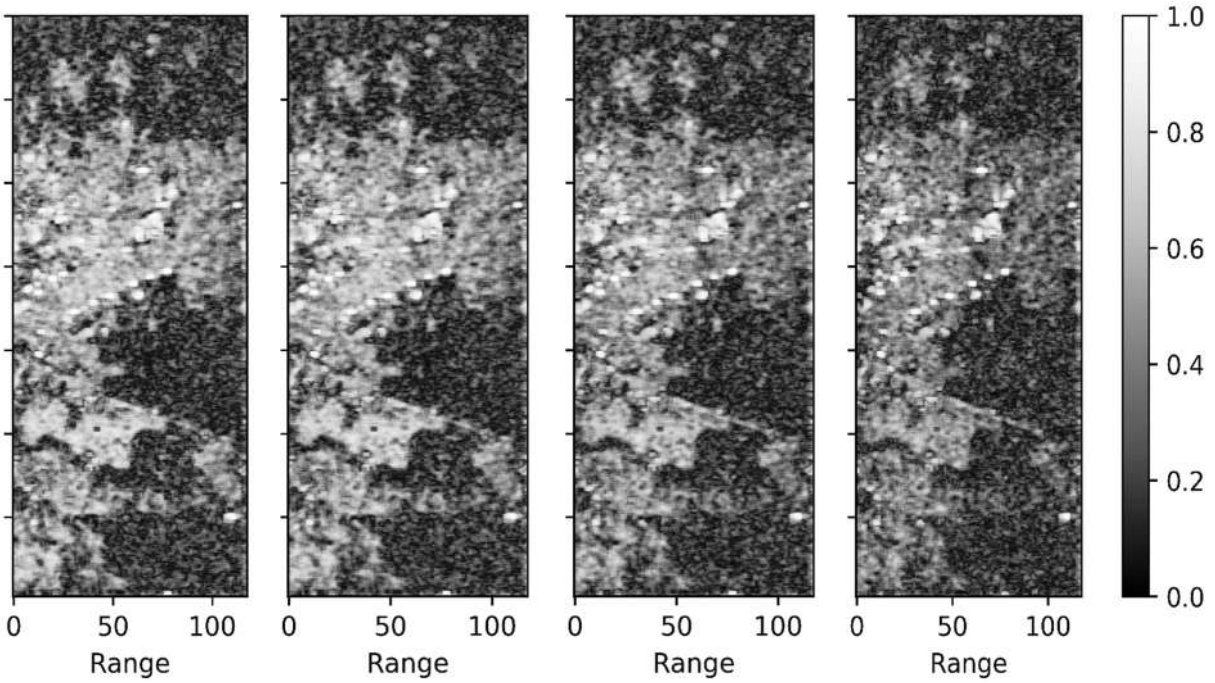

Figure 9.16: Interferometric coherence of distorted Hydroterra images for different wind speeds: input data with 0.0 m/s (a), wind speed of 3 m/s (b), wind speed of 5 m/s (c), wind speed of 10 m/s (d).

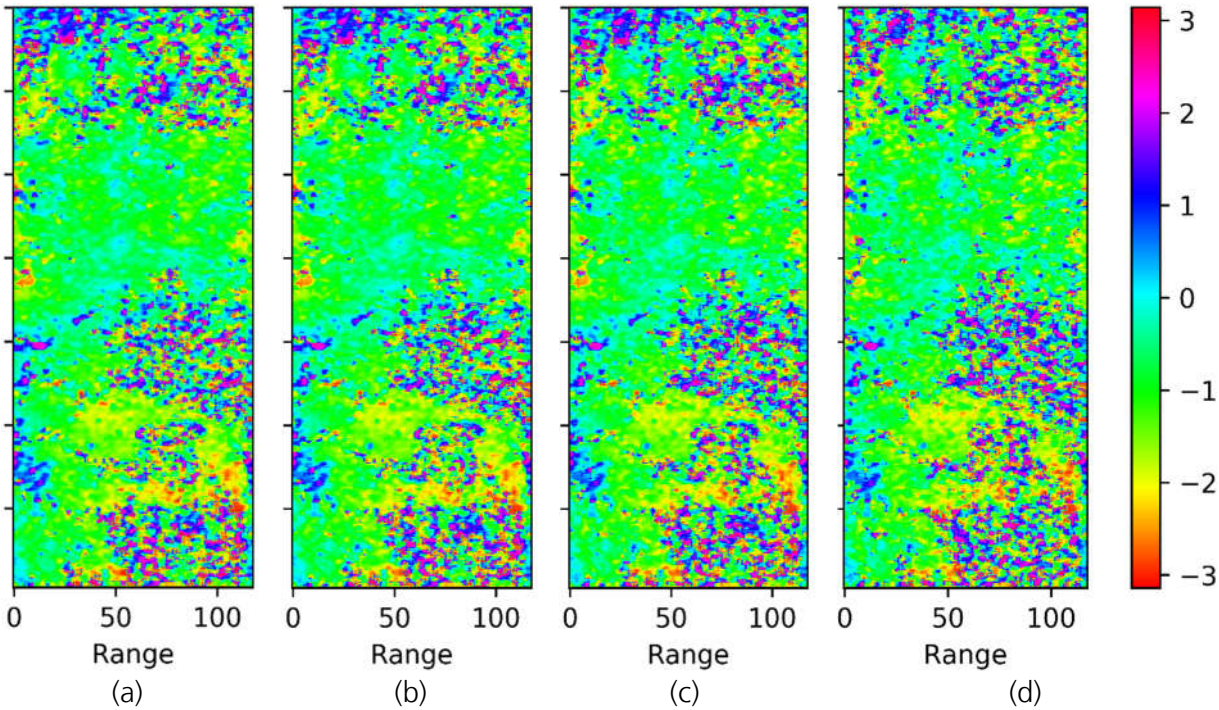

Figure 9.17: Interferometric phase of distorted Hydroterra images for different wind speeds: input data with 0.0 m/s (a), wind speed of 3 m/s (b), wind speed of 5 m/s (c), wind speed of 10 m/s (d).

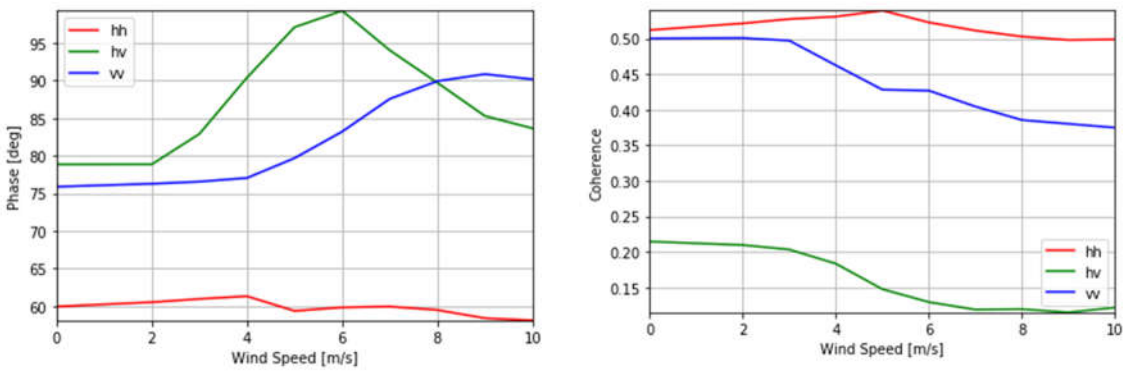

(a)

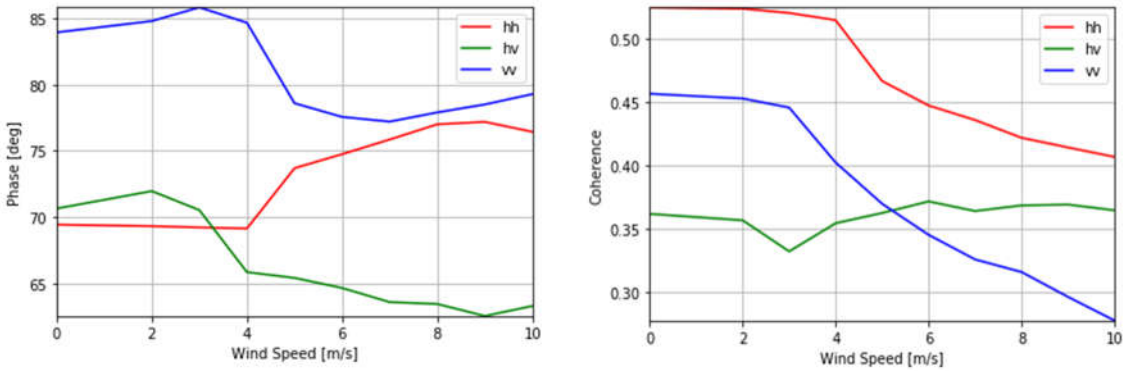

(b)

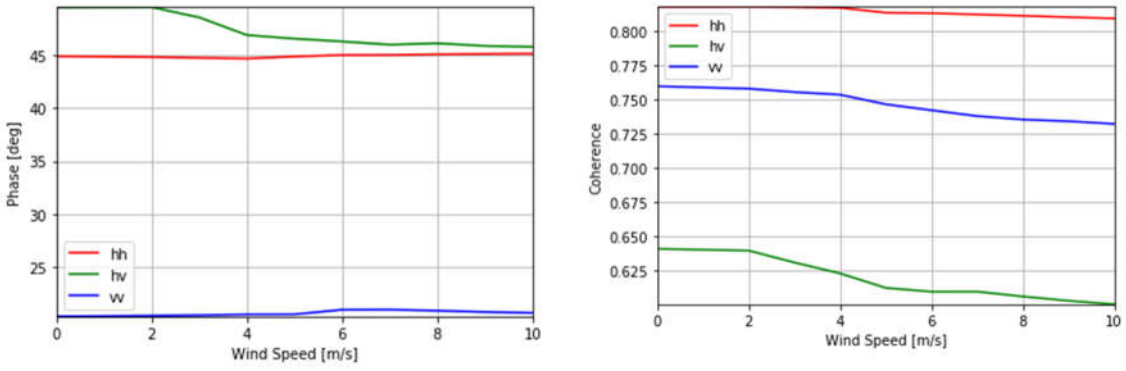

(c)

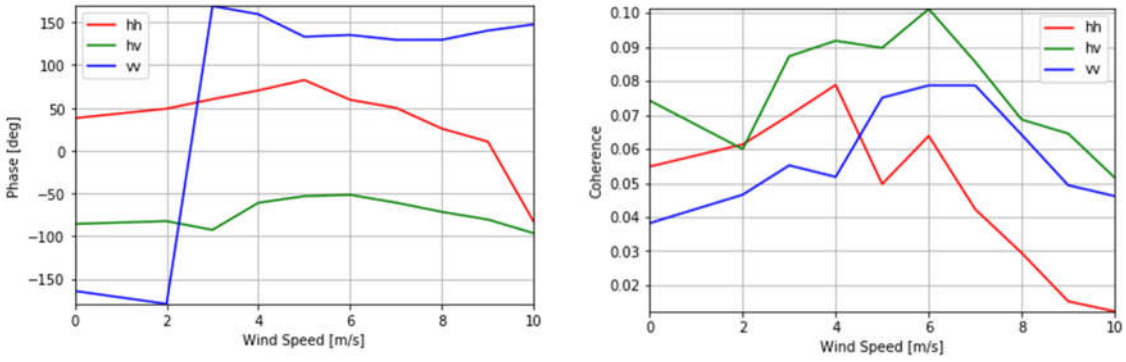

(d)

Figure 9.18: Impact on interferometric phase and coherence between flight 1 and flight 2 for the land cover types shown in Figure 9.12 to Figure 9.15. From top to bottom: A30 - wet grass (a), B06 - wheat field (b), Urban1 - urban area (c), and Forest2 - forest (d).

9.2 Product Description

As part of 'WP500 – Hydroterra Images with different Wind Conditions', DLR has simulated single-look complex (SLC) data starting from the two HT quality data sets, delivered already. The wind simulated data will be delivered to ESA in the following format:

- slc_ht_flZZ_YY_X.X.rat

Here "ZZ" corresponds to the flight number, "YY" to the polarization and "X.X" to the simulated wind speed. In addition, the coherence and intensity ratio with respect to the undistorted images is included in the following files.

- coh_flZZ_YY_X.X.rat
- ratio_dB_flZZ_YY_X.X.xml

The data files are grouped into different directories for the different flight numbers and further into sub-folders for the different wind speeds, e.g. fl01/3.0 for flight 1 data with simulated wind parameter of 3.0 m/s. The simulation is performed for wind speeds ranging in integer steps from 2.0 to 10.0 m/s.

The rat format is described in more detail in [3]. Parameter files are not part of this product description as they are left unchanged with respect to the input data.

10 Summary

This is the final report of the SARSimHT study. The first objective of this study is to simulate Hydroterra amplitude and interferometric products from airborne radar data. The second objective is to investigate variations of image parameters as a function of geophysical conditions acquired from ground-truth data. The third objective is to investigate the potential to detect diurnal changes of land surface parameters with simulated Hydroterra time series with soil moisture for agriculture product (SSM Agro) parameters. The fourth objective is to simulate Hydroterra data with different wind effects to identify and quantify to which extend defocussing of high vegetation areas affects the surrounding areas of bare soil / sparse vegetation.

In Chapter 3 simulated Hydroterra amplitude and interferometric products are presented. These products are simulated from airborne data, which were collected with the F-SAR radar system. Two flights were performed, one in the morning and one in the afternoon. Single-look complex products of both flights and for all polarisations and also multi-look detected products of both flights and for all polarisations were simulated for the Hydroterra system. These products were processed for the fully available integration time of 1 hour and 41 minutes for the first flight and 1 hour and 44 minutes for the second flight, but also for shorter integration times of 43 and 17 minutes. The two simulated Hydroterra single-look complex products are used to compute the interferometric phase and the coherence for all polarisations. These products are also presented in Chapter 3. All data will be delivered to ESA.

Additionally, in Chapter 3 the contrast of the two simulated Hydroterra single-look complex products was evaluated and compared to the contrast of a single-look complex image of one acquisition. This analysis showed that in forest areas the contrast is lower for the Hydroterra products due to the change of backscatterer during the long integration time, resulting in practice in an increased clutter level for the neighbouring pixels. Note that this analysis was not evaluating the impact of wind in the formation of the synthetic aperture, but just the change in backscattering. Chapter 9 (see below) is the one performing the evaluation of wind-blown clutter.

In Chapter 4 the intensity, coherence and interferometric phase of field areas around six survey points were analysed for both flights. At the survey points the vegetation type and height was collected by the ground measurements teams during the airborne campaign. This analysis showed that if only grass is present, a small drop in the intensity can be observed between the first and second flights.
Additionally, the coherence between different acquisitions during the first flight is much lower than the one during the second flight for grass areas. This is considered to be due to moisture. It rained heavily the night before the airborne campaign and the ground measurement teams reported that more moisture on the grass was present during the morning than during the afternoon. Therefore, the moisture change was more pronounced during the morning flights, while during the afternoon flights the grass had dried almost completely and therefore the change in moisture was less significant. For field areas with crops a change in intensity or coherence between the first and second flight was not observed, because here other scatterings effects are more dominant than the moisture effect.

The intensity, coherence and interferometric phase were analysed in Chapter 4 for the F-SAR radar parameters. In Chapter 5 a time series was simulated with Hydroterra radar parameters, which were described in Chapter 3. The purpose of Chapter 5 is to evaluate if the same variations can be observed as in Chapter 4. One conclusion is that for grass areas also a drop in the intensity between the second and first flight is visible, but this drop is less pronounced, because the intensity varies stronger for Hydroterra data due to the limited mitigation of speckle. This is

because less samples of each field are available for averaging. Different coherences between the first and the second flight are also visible, although this is not the case for the volume scattering component, which is closer to the noise power. The volume scattering component has the lowest signal and therefore thermal decorrelation has the highest influence.

Additionally, coherences at different survey points of the simulated Hydroterra products were compared to the ones of Hydroterra time series. It was found that the coherence of simulated Hydroterra products matches well with the mean coherence between all acquisitions of the first flight and all acquisitions of the second flight.

In Chapter 6 coherences of 3 forest and 3 urban areas were analysed for time series with F-SAR and Hydroterra radar parameters. As one would expect, the coherences were much lower for the forest areas than for the field areas which were analysed in Chapters 4 and 5. As expected, for urban areas volume decorrelation has a high impact, which can be observed in the correlation between the coherence and the height of ambiguity.

In Chapter 5 the intensity, coherence and interferometric phase were evaluated of simulated Hydroterra time series with radar parameters of the scenario 4 of the interferometric type (Glacier flow/ Landslides). In Chapter 7 these parameters were calculated and presented for simulated Hydroterra time series with soil moisture for agriculture product (SSM Agro) parameters. The intensity, coherence and interferometric phase were compared to the ones of F-SAR data for different polarisations. One difference between the data in Chapter 5 and Chapter 7 is that for Hydroterra time series with SSM Agro parameters the drop in the intensity is more pronounced for some survey points, due to different resolutions in range and azimuth. This chapter also shows that the main observations of the F-SAR data for some survey points, which are the drop in the intensity and a lower coherence during the second flight, can also be observed for the Hydroterra time series with SSM Agro parameters.

The phase triplets analysis were performed in Chapter 8 to make a first evaluation of diurnal moisture changes. This analysis with the high-resolution F-SAR data showed a clear signal in the closure phase, probably indicating a change in moisture. The closure phase of F-SAR data was compared to the one of simulated Hydroterra time series. This comparison showed that several fields show a non-zero closure phase for F-SAR as well as for simulated Hydroterra data. However, due to the significant amount of spatial averaging which has to be performed to mitigate the phase noise in the phase triplets and due to the small field sizes, not all fields of the test site can be analysed with phase triplets by using simulated Hydroterra time series. For future experiments it would be therefore interesting to choose test sites with larger field areas and also to have ground truth measurements of soil moisture in order to make a proper quantitative analysis.

In Chapter 9 a power-law model derived from BOREALSCAT measurements has been used to modify the set of simulated Hydroterra products generated from DLR's airborne campaign data and to analyse the effects of wind-blown clutter on both, the vegetated areas (especially forest) and the bare soil/low-vegetation areas in between. First, a vegetation/non-vegetation mask has been derived from the full resolution airborne SAR data using a polarimetric entropy-alpha classification and repeat-pass coherence information. Morphological closing and opening operators were employed to ensure a more homogeneous, planar vegetation cover. Areas labelled as vegetation were then partially defocused using realisations of wind speed induced Doppler distortions, according to BOREALSCAT model parameterisation from 2 to 10 m/s. With increasing wind speed the amount of backscatter being defocused is increased, leading to a drastic reduction of backscatter and coherence in the vegetation areas with respect to the undistorted SAR image. In the non-vegetated areas, the effects on wind-blown clutter are an increase of energy (noise) and a decay of the coherence with respect to the undistorted image. The explanation is,

that the defocused energy, which spreads from vegetation to non-vegetated areas does not increase the noise floor in a dramatic way, at least for the test scene under consideration. The deterioration is considered tolerable up to a wind speed of 4 m/s, both with respect to the impact on retrieved backscatter (< 0.5 dB) as well as on coherence (> 0.95) and impact on interferometric phase (< 5deg). For the same wind speed limit, urban areas are hardly affected because of their increased reflectivity.